Title

An Explosive Party: Supernovae, Tidal Disruption Events, and Quasi-Periodic Eruptions

Author

Patra, Kishore Chandra

Publication Date

2024

Peer reviewed|Thesis/dissertation

An Explosive Party: Supernovae, Tidal Disruption Events, and Quasi-Periodic Eruptions

By

Kishore Chandra Patra

A dissertation submitted in partial satisfaction of the

requirements for the degree of

Doctor of Philosophy

in

Astrophysics

in the

Graduate Division

of the

University of California, Berkeley

Committee in charge:

Distinguished Professor Alexei Vladimir Filippenko, Chair
Assistant Professor Wenbin Lu
Professor Daniel Kasen

Spring 2024

An Explosive Party: Supernovae, Tidal Disruption Events, and Quasi-Periodic Eruptions

Abstract

An Explosive Party: Supernovae, Tidal Disruption Events, and Quasi-Periodic Eruptions

by

Kishore Chandra Patra

Doctor of Philosophy in Astrophysics

University of California, Berkeley

Distinguished Professor Alexei Vladimir Filippenko, Chair

Astrophysical transient events, particularly Type Ia supernovae (SNe Ia) and tidal disruption events (TDEs), provide critical insights into stellar systems and black hole activity. This thesis studies polarimetry of SNe Ia and TDEs in an attempt to better understand the geometry and physical processes behind these explosive events.

For SN 2019ein, spectropolarimetric data from approximately 11 days before to 10 days after peak brightness revealed a continuum polarization of 0.0–0.3%. The constant polarization angle indicates axial symmetry in the explosion, consistent across inner and outer ejecta regions. Notably, polarization at the Si II and Ca II lines reached about 1%, suggesting a largely spherical explosion with localized clumping of intermediate-mass elements. These observations largely disfavor merger-induced models for SN 2019ein. A larger sample of SNe Ia spectropolarimetry observed at Lick Observatory is presented and described.

In the study of the TDE AT 2019qiz, spectropolarimetry showed negligible continuum polarization at peak brightness, suggesting a nearly spherical, optically thick electron scattering photosphere around the black hole. By day 29, polarization increased to around 1%, indicating a more aspherical interior as the fallback rate decreased and the photosphere receded. This marks the first detailed spectropolarimetric evolution observed in a TDE, and supports the reprocessing model for the source of optical emission in TDEs. The study of AT 2019qiz is followed by imaging polarimetry of several TDEs from Keck Observatory in an attempt to build a more comprehensive picture of gas geometry in TDEs.

Additionally, the thesis explores the newly discovered X-ray quasi-periodic eruptions (QPEs), analyzing archival *Hubble Space Telescope* images of the QPE source GSN 069. The data revealed a compact [O III] emission region within a 35 pc radius of the nucleus, along with extended emission up to 2 kpc away. Simulations with the photoionization

code CLOUDY suggest this emission comes from dense gas, likely ionized by X-rays from a young accretion disk, offering a unique glimpse into the dynamic processes at play in the host galaxies of QPEs.

To Amma and Papa

Contents

List of Figures v

List of Tables viii

Acknowledgments ix

1 Introduction 1
- 1.1 Type Ia Supernovae . . . 2
- 1.2 Tidal Disruption Events . . . 3
- 1.3 Quasi-Periodic Eruptions . . . 3
- 1.4 Polarimetry: A Powerful Tool . . . 4
- 1.5 Thesis Chapters . . . 5
- 1.6 Other Work . . . 5

2 Spectropolarimetry of the Type Ia SN 2019ein Rules Out Significant Global Asphericity of the Ejecta 7
- 2.1 Chapter Abstract . . . 7
- 2.2 Introduction . . . 8
- 2.3 Observations and data reduction . . . 10
  - 2.3.1 Kast Spectropolarimetry . . . 10
  - 2.3.2 RINGO3 Imaging Polarimetry . . . 13
- 2.4 Analysis and results . . . 13
  - 2.4.1 Calculating the Stokes q and u . . . 13
  - 2.4.2 Polarimetric Calibration . . . 14
  - 2.4.3 Interstellar Polarization . . . 14
  - 2.4.4 Continuum Polarization . . . 17
  - 2.4.5 Line Polarization . . . 17
  - 2.4.6 The q–u Plane and the Dominant Axis . . . 23
  - 2.4.7 Polarization Time Series . . . 25
- 2.5 Discussion . . . 28

2.5.1 Implications for Explosion Scenarios . . . 30
2.5.2 Comparison with a Detonating Failed Deflagration (DFD) Model . 32
2.5.3 The Si .9513.6λ6355 Polarization Compared with a Larger Sample 33
2.6 Concluding Summary . . . 34

3 Lick Spectropolarimetry Database of Type Ia Supernovae 37
3.1 Introduction . . . 37
3.2 The LSD-Ia . . . 38
3.3 Using the Lick spectropolarimetry database: The example of SN 2011fe . . . 45
3.4 Future Work . . . 51
3.5 Acknowledgments . . . 51

4 Spectropolarimetry of the Tidal Disruption Event AT 2019qiz: A Quasispherical Reprocessing Layer 54
4.1 Chapter Abstract . . . 54
4.2 Introduction . . . 55
4.3 Observations . . . 57
4.4 The measured polarization . . . 58
4.5 Interpretation . . . 61
4.5.1 The size of the reprocessing layer . . . 61
4.5.2 Substructures in the electron-scattering photosphere . . . 64
4.5.3 Hα line polarization . . . 67
4.5.4 Comparison with other polarimetric studies of TDEs . . . 69
4.6 Conclusion . . . 70

5 Imaging Polarimetry of Tidal Disruption Events 72
5.1 Introduction . . . 72
5.2 Observations and Data Reduction . . . 73
5.3 Calibrating LRISp . . . 74
5.4 Preliminary Results . . . 76
5.5 Future Work . . . 84

6 Constraints on the Narrow-Line Region of the X-ray Quasi-periodic Eruption Source GSN 069 85
6.1 Chapter Abstract . . . 85
6.2 Introduction . . . 86
6.3 HST Images . . . 87
6.4 Photometry . . . 92
6.5 CLOUDY Simulations . . . 97
6.6 Discussion and Prediction for Future Observations . . . 104

6.6.1 Extended [O III] emission region 105
6.6.2 Testable predictions for future observations 106
6.7 Conclusion 107

Bibliography **111**

List of Figures

2.1 Spectropolarimetry of SN 2019ein at day −10.9 relative to the *B*-band peak brightness at MJD 58618.2 (Kawabata et al. 2020). The cyan vertical bands represent the regions of telluric correction. The panels below the total-flux spectrum represent the polarimetry before (red) and after (black) the ISP correction. The grey-shaded area indicates the associated 1σ uncertainty. The *PA* panel shows only the polarization position angle after ISP correction. With the exception of the flux spectrum, we use 50 Å binning for the purpose of presentation. 18
2.2 Similar to Figure 2.1 but for day −9.9. We use 40 Å binning for the purpose of presentation. 19
2.3 Similar to Fig. 2.1 but for day −3.9. We use 25 Å binning for the purpose of presentation. 20
2.4 Similar to Fig. 2.1 but for day −2.9. We use 25 Å binning for the purpose of presentation. The wavelength region 4800–5600 Å was used to estimate the ISP as described in Section 2.4.3. 21
2.5 Similar to Fig. 2.1 but for day +10.1. We use 30 Å binning for the purpose of presentation. 22
2.6 Polarization in the Stokes *q*–*u* plane. The Si .9513.6λ6355 and Ca .9513.6NIR3 lines were omitted from the left-side panels labeled "continuum". The dashed lines in the "Si .9513.6λ6355" and the "Ca .9513.6NIR3" panels represent the dominant axes for the labeled absorption features. 26
2.7 Polarization vs. time. The polarization and *PA* have been corrected for the ISP. The black squares represent the continuum polarization and *PA* from the Kast spectropolarimeter. The red, blue, and green circles show the polarization measured by Kast in different wavelength regions: blue (4580–6400 Å), green (6500–7600 Å), and red (7700–9000 Å). The blue inverted triangles show polarization and *PA* measured by RINGO3 in the blue channel with wavelength range 3500–6400 Å. The light curves in the top panel were obtained by KAIT at Lick Observatory. 27

3.1 Spectropolarimetry of SN 2011fe on day −9. 47
3.2 Polarization of SN 2011fe on day −9 presented in the Stokes $q - u$ plane. . . . 48
3.3 Spectropolarimetry of SN 2011fe on day +13. 49
3.4 Polarization of SN 2011fe on day +13 presented in the Stokes $q - u$ plane. . . 50
3.5 The polarization time series of SN 2011fe. 52
3.6 Polarization of SN 2011fe on day +76. Note the significant polarization in the Ca II line near-infrared triplet lines. 53

4.1 Spectropolarimetry of AT 2019qiz on days +0 and +29 relative to the peak brightness on MJD 58764 (Nicholl et al. 2020). Cyan vertical bands mark the spectral regions corrected for major telluric lines. The error bars indicate 1σ uncertainty. With the exception of the flux spectrum, we use 60 Å binning on day +0 and 80 Å binning on day +29 for clarity of presentation. *PA* is undefined when p is 0; we do not show those points in the *PA* panel. 59
4.2 Polarization of AT 2019qiz in the $q - u$ plane on day +0. The left-side panel shows the polarization in the wavelength range 5400–8600 Å, coloured by wavelength. Additionally, the size of the data points also reflects their relative wavelengths in a decreasing order (i.e., larger points are bluer). The right-side panel only shows the polarization of the Hα line in the wavelength range 6000–6900 Å. The black dashed lines are the best-fitting dominant axes. Constant-polarization contours in 0.5 per cent increments are shown as dashed circles. The black star in each panel represents the error-weighted mean Stokes q and u. The coefficient of determination (R^2) and the χ^2/DoF are also provided. . . . 65
4.3 Same as Figure 4.2 but for day +29. The Hα wavelength range is 6300–6900 Å. The abscissa and the ordinate are on the same scale as Figure 4.2 for ease of comparison. 66
4.4 Schematic diagram illustrating the geometrical configuration of a sky-projected electron-scattering photosphere that is compatible with the observed polarimetry. The white arrows represent the relative size and direction of the local polarization. The outer circle shows the scattering photosphere on day +0, and the inner ellipse displays the photosphere a month later on day +29. The inner ellipse has an aspect ratio of $e \approx 0.8$, which produces $\sim$ 1 per cent continuum polarization in a scattering-dominated photosphere. 68

5.1 An image of AT 2019qiz in the *B* filter with LRISp showing both the ordinary (top) and extraordinary (bottom) images. 75
5.2 Comparison between LRISp and Kast for the null-standard star Gaia2504724807045303808. Kast data are shown in black whereas LRISp data are with colors denoting the different filters. 77

5.3 Similar to Figure 5.2 but showing comparison between LRISp and Kast for the null-standard star Gaia2504739959689944704. 78
5.4 Similar to Figure 5.2 but showing comparison between LRISp and Kast for the high-polarization standard star Gaia524279927616349440. 79
5.5 Similar to Figure 5.2 but showing comparison between LRISp and Kast for the high-polarization standard star Gaia524280099415036672. 80
5.6 Polarization and position angle of TDEs. The colors denote the different filters whereas the shapes represent different TDEs. 81

6.1 The throughput functions of the *HST* filters in which the images of GSN 069 were obtained. 88
6.2 The left panel displays the *HST* image in the narrow-band filter FR505N which captures [O III] emission at 4958.9 Å and 5006.9 Å, along with the continuum emission. The middle panel shows the continuum image in filter FR647M, whereas the right panel presents the continuum-subtracted image of GSN 069. All three panels are plotted on the same flux-density scale to enable direct comparison. 90
6.3 The left panel shows the far-UV image created by subtracting F165LP from F140LP. The middle panel displays the broad-band F606W optical image. The continuum-free [O III] emission image is reproduced for comparison in the right panel. All three panels are plotted on the same flux-density scale for comparison. 91
6.4 Fitting of photometry models to the observed data. Left panel shows the fitting of a power-law-only model, whereas the right panel shows the fitting of a power-law + point-source model. The bottom panels display observed data-to-best-fit model ratios as residuals. 95
6.5 Posterior distributions of the parameters that describe the two models fit to the photometry of the continuum-subtracted [O III] image. 96
6.6 Constraints on the hydrogen number density ($n_{\rm H}$) and the distance from SMBH of the [O III]-emitting gas in the nucleus of GSN 069. See the continued caption after this figure. 102
6.8 The optical spectrum of GSN 069 was obtained on Sep. 19, 2019 UTC, using the FORS2 instrument on the 8.2 m Very Large Telescope. The slit width and the extraction window were 1″ and 1.25″, respectively, which corresponds to $\sim 0.4 \times 0.5$ kpc in physical size. 110

List of Tables

2.1 Journal of spectropolarimetric observations. 12
2.2 Summary of polarimetry results. 16
2.3 Fitted parameters for the dominant axes. 24

3.1 Inventory of spectropolarimetry of SNe Ia observed at Lick Observatory. 39
3.2 A portion of the Lick Spectropolarimetry Database for SNe Ia. 44

5.1 Imaging polarimetry of standard stars observed with Keck LRISp on UT Dec 13, 2023. Statistical uncertainty in the last few significant figures is provided in parentheses next to each measurement. For e.g., 0.07 ± 0.11 is written as 0.07(11) and 32 ± 24 is written as 32(24). 82
5.2 Imaging polarimetry of TDEs observed with Keck LRISp. Statistical uncertainty in the last few significant figures is provided in parentheses next to each measurement. For example, 0.07 ± 0.11 is written as 0.07(11) and 32 ± 24 is written as 32(24). Note that the *R*-band image of AT 2019qiz was severely affected by cosmic rays, and consequently was omitted from the analysis. . . . 83

6.1 Summary of *HST* observations of GSN 069. 88
6.2 Flux measurement of all *HST* images. The radii in arcseconds of the circular apertures are shown in the header. The uncertainty presented here is the statistical Poisson noise. 94

Acknowledgments

It is often said that 'it takes a village to raise a child', and this adage holds particularly true for my journey toward a PhD. I extend my deepest gratitude to everyone who contributed to this exciting endeavor.

First and foremost, I owe immense gratitude to my thesis advisor, Alex Filippenko. Over the past six years, Alex has provided me with a unique sandbox of intellectual freedom, allowing me to explore a diverse array of projects in astrophysics. His expertise in supernovae, observations, and spectroscopy, along with his leadership in managing a well-oiled research group, have profoundly shaped my skills as a scientist. I am also thankful for the opportunities to serve as a teaching assistant in his Astro C10 course, which was an incredibly inspiring experience that taught me the principles of good scientific communication.

I am equally grateful to Wenbin Lu, with whom I had the pleasure of working closely over the last two years. His boundless knowledge and insightful guidance have instilled in me the confidence to tackle complex theoretical problems in astrophysics. Similarly, I must acknowledge Dan Kasen, who has been a supporter throughout my PhD journey, serving on all my committees and providing crucial academic guidance.

My experience was enriched by my colleagues in Alex's dynamic research group. Special thanks go to Tom Brink and WeiKang Zheng for their mentorship in spectroscopic observations and data reduction, and to Yi Yang for his expertise in spectropolarimetry. Working alongside Sergiy Vasylyev on spectropolarimetry data challenges was exceptionally rewarding. I also cherish the relationships developed with numerous undergraduates in our group, especially Efrain Alvarado III, Eli Gendrau-Distler, and Kate Bostow, whose enthusiasm and leadership in the exoplanet research project were inspirational. I am also grateful for numerous stimulating discussions with Raf Margutti, Ryan Chornock and the other members of the Explosive Astro seminar.

I am fortunate to have had the support of my close friend, colleague, and mentor, Andrea Antoni. Her presence made the challenges of graduate school far more bearable and enjoyable.

Maintaining a healthy work-life balance during graduate school was largely made possible by my involvement with the Spartan Cricket Club and the many wonderful people

associated with it, particularly Hasu Patel and Harsh Shah. Additionally, I am thankful for my role as the captain and a 'senior' advisor to the Cal Cricket Club, which was founded by a group of enterprising undergraduates the year I joined UC Berkeley. These experiences provided me with much-needed leisure and camaraderie.

My heartfelt appreciation extends to my network of friends— Ishwar Kohale, Priti Kharel, Iveel Tsogsuren, and Surya Tripathi—who have enriched my life with their unwavering love and support.

I am profoundly grateful to the numerous organizations and individuals who have financially supported my education since 5th grade, from the taxpayers of India to the Pestalozzi International Foundation, and from the MIT UROP program to the taxpayers of California. Special thanks also go to the I-House at UC Berkeley and the many individual donors who have supported my education and research. The appropriate individual donors are credited at the end of each chapter.

None of this would have been possible without the sacrifices made by my parents, including allowing their 11-year-old boy to leave home in pursuit of education. I cannot thank amma and papa enough for their unending love, support, and hope for me. I owe everything to them. My brother and sister, who grew up with an often absent brother, have shown nothing but patience and affection.

Finally, my deepest gratitude is for my wife Nina. Since the start of my graduate studies, she has witnessed my personal and professional growth and has been a cornerstone of my journey. Her love and support have been my greatest sources of strength. I am also thankful to Nina's parents and her brother for being like a second family to me.

To all of you, I am eternally grateful for guiding, supporting, and believing in me throughout this incredible journey. Thank you.

Chapter 1

Introduction

The Universe displays an array of spectacular, though transient, performances in the form of high-energy explosions and flares. These events, ranging from supernovae (SNe) to tidal disruption events (TDEs), offer a window into the fundamental processes that shape the Universe. The study of these explosions intersects with a diverse set of physics subfields, including thermodynamics, nuclear physics, relativity, (magneto)hydrodynamics, electromagnetism, and the burgeoning field of gravitational wave astronomy, demonstrating the richness and complexity involved in studying them.

Astrophysical explosions, by their very nature, are transient. They *burst* into prominence, deliver a wealth of information, and then fade away. Once an event concludes, the opportunity for direct observation is lost, although its remnants may continue to offer valuable insights for decades thereafter. The advent of advanced optical transient surveys, such as the Zwicky Transient Facility (ZTF; Bellm et al. 2019) and the All-Sky Automated Survey for Supernovae (ASAS-SN[1]), has revolutionized our ability to detect and study explosions of all kinds. These surveys have discovered a universe teeming with transient phenomena, each with its own unique story and theoretical framework, thereby giving birth to the field of transient time-domain astronomy. This rapidly developing field focuses on capturing the evolution of these transients over time, providing an ever-changing perspective on the physical processes driving these powerful events.

The significance of time-domain science has been underscored by its designation as a top priority in the Astro 2020 Decadal Survey[2], reflecting the community's recognition of its potential to unravel some of the Universe's deepest mysteries. The upcoming start of the Vera C. Rubin Observatory's Legacy Survey of Space and Time (LSST) represents a giant leap forward in our observational capabilities, promising to uncover an even broader array

[1] https://www.astronomy.ohio-state.edu/asassn/

[2] https://www.nationalacademies.org/our-work/decadal-survey-on-astronomy-and-astrophysics-2020-astro2020

of transients in unprecedented numbers.

This thesis ventures into the diverse landscape of transient events, focusing on three particular phenomena: Type Ia SNe, TDEs, and quasi-periodic eruptions (QPEs). Each of these events, in their own right, constitutes a rich field of study. Supernovae, the cataclysmic end-of-life explosions of stars, forge heavy elements and influence galactic evolution. TDEs, where a star is shredded by a supermassive black hole's gravitational forces, provide a rare glimpse into the realm of strong gravity and black hole feeding mechanisms. Lastly, the mysterious QPEs, with their enigmatic and (quasi)periodic flares, offer a new puzzle in the world of high-energy astrophysics, challenging our understanding of accretion processes and compact object physics. This thesis explores the aforementioned phenomena, sometimes blending observations with theory, to enhance our understanding of explosive astrophysics.

1.1 Type Ia Supernovae

Type Ia supernovae (SNe Ia) have been pivotal in astrophysics for over fifty years, profoundly influencing our understanding of the Universe. They have provided insights into phenomena ranging from nucleosynthesis and chemical enrichment to the heating of the interstellar medium. Notably, they played a crucial role in the discovery of the Universe's accelerating expansion (Riess et al. 1998; Perlmutter et al. 1999), and the more recent excitement around the "Hubble tension" (Riess 2020).

Despite their wide-ranging significance, the origins and explosion mechanisms of SNe Ia remain areas of active research. It is widely accepted that these objects arise from thermonuclear explosions in white dwarfs (WDs), but the nature of their progenitors and explosion mechanisms are still poorly understood.

Two progenitor scenarios are popularly put forth to explain the origin of SNe Ia. (i) Double-degenerate channel: the SN results from mass transfer between two WDs in a binary system (Iben & Tutukov 1984; Webbink 1984). (ii) Single-degenerate channel: a WD accretes material from a companion star until it nears the critical Chandrasekhar mass limit and undergoes a thermonuclear explosion (Nomoto et al. 1976).

The explosion itself can initiate through several mechanisms: (i) Delayed detonation: A transition from subsonic burning (deflagration) to a supersonic, explosive burning (detonation) (Khokhlov 1991). (ii) Double detonation: An initial detonation in a helium layer on the WD's surface ignites a secondary explosion within the core (Fink et al. 2010). (iii) Compressional heating: The merger or collision of two WDs generates enough heat to trigger an explosion (Pakmor et al. 2010).

As it stands, no single model for the progenitor or the explosion mechanism can completely explain the diverse and sometimes confounding observations associated with SNe Ia. However, the community is making steady progress toward a better understanding of

these highly energetic events (see Liu et al. 2023 for a recent review).

1.2 Tidal Disruption Events

Occasionally, a star ventures too close to a supermassive black hole (SMBH), and the tidal forces exerted by the black hole overpower the star's gravitational force, ripping the star apart. Known as tidal disruption events (TDEs), these phenomena occur when a star crosses within the tidal radius of the SMBH (Hills 1975). Owing to the large range of specific orbital energies gained by the stellar debris post-disruption, about half remains bound in highly eccentric orbits around the SMBH, while the remainder escapes (Rees 1988). The bound debris is expected to fall toward the SMBH and form an accretion disk, with the gravitational potential energy of the infalling material converting into electromagnetic radiation, producing a bright flare that can last for several months.

Initially, all TDEs were thought to primarily emit extreme-ultraviolet (UV) and X-ray light, similar to active galactic nuclei (AGNs). Yet, many exhibit strong near-UV/optical emission with luminosities that are significantly higher than, or at least on par with, their X-ray emission (see, e.g., Gezari et al. 2008; Holoien et al. 2016a; Auchettl et al. 2018; vanVanvan Velzen et al. 2021), sparking debates about the source of this bright optical emission and the absence of X-rays in some of these events. Two main hypotheses have been suggested: (i) the accretion disk does generate substantial X-ray emission, but this is reprocessed by a thick gas layer located well beyond the tidal radius (e.g., Strubbe & Quataert 2009; Metzger & Stone 2016; Dai et al. 2018; Lu & Bonnerot 2020), and (ii) optical emission from TDEs is energized by shocks resulting from collisions within streams in the outer regions of a highly eccentric disk (e.g., Piran et al. 2015; Shiokawa et al. 2015).

Indirect evidence increasingly supports the first hypothesis, suggesting that accretion disks form promptly in TDEs, as evidenced by double-peaked Balmer lines (Hung et al. 2020; Short et al. 2020) and Bowen fluorescence triggered by excitation from high-energy photons (Leloudas et al. 2019; Blagorodnova et al. 2019). The mechanisms leading to the formation of a reprocessing gas layer, however, remain a mystery. Theories propose that it may originate from winds or outflows from the TDE (Lodato & Rossi 2011; Miller 2015; Jiang et al. 2016; Dai et al. 2018; Bonnerot et al. 2021) or from a radiation-pressure-supported envelope formed from the bound debris (Loeb & Ulmer 1997; Coughlin & Begelman 2014).

1.3 Quasi-Periodic Eruptions

Quasi-periodic eruptions (QPEs) are a new class of X-ray sources best identified by X-ray surveys. These enigmatic objects exhibit distinctive characteristics, featuring bursts

of bright X-ray emission lasting for roughly an hour, superimposed on top of quiescent emission consistent with steady-state accretion around a black hole. The quasi-periodic recurrence times range from a few hours to days. In the X-ray band, the spectra of QPEs are thermal-like, with higher temperatures ($k_{\rm B}T \approx 100\,{\rm eV}$) during the eruption phase and lower temperatures ($k_{\rm B}T \approx 50\,{\rm eV}$) in quiescence. The flare amplitude can reach 100 times that of the quiescent phase at energies $< 2\,{\rm keV}$. QPEs are predominantly detected in the nuclei of low-mass galaxies ($M_* \approx 10^9\,M_\odot$), implying that these sources are associated with relatively low-mass SMBHs. To date, only 7 QPEs have been securely confirmed: GSN 069 (Miniutti et al. 2019), RX J1301.9+2747 (Giustini et al. 2020), eRO-QPEs 1 through 4 (Arcodia et al. 2021, 2024), and *Swift* J0230+28 (Guolo et al. 2024). Given the small number of known QPEs and sparse temporal and wavelength coverage of them, there is limited knowledge regarding their origin(s), emission processes, lifetime, and periodicity, making them a novel and exciting probe of low-mass SMBHs.

Several theoretical frameworks have been proposed to explain the origin of QPEs, spanning concepts such as disk instabilities (e.g., Raj & Nixon 2021; Kaur et al. 2023), mass transfer from various configurations of orbiting bodies (e.g., Chen et al. 2022; King 2020, 2022; Linial & Sari 2023), and interactions between a secondary orbiting object and the accretion disk around the primary SMBH (e.g., Suková et al. 2021; Franchini et al. 2023). A connection between QPEs and TDEs has also been proposed (e.g., Xian et al. 2021; Linial & Metzger 2023). Additionally, some of the currently known QPE sources/candidates might be associated with X-ray-selected TDEs (e.g., GSN 069, J02491, eRO-QPE3). A common theme among all the aforementioned models is an accretion disk, whose X-ray emission has been detected during the quiescent phase in at least some of the QPE sources (e.g., GSN 069, RXJ 1301, eRO-QPE4). QPEs can provide a unique opportunity to study the properties and environments of SMBH accretion disks as they form and evolve. There is some indication that these accretion disks may be compact in size, as inferred from the lack of broad optical emission lines and near-IR dust emission typically associated with AGNs. However, the disk properties (e.g., accretion rate, mass feeding, and radial structure) are poorly constrained owing to lack of multiwavelength observations with sufficient spatial resolution to significantly reduce the contamination from the host galaxy.

1.4 Polarimetry: A Powerful Tool

The vast majority of transient events are not resolvable, even with the most powerful interferometers. Polarimetry remains the sole method for studying the geometry of these unresolved explosions. Light from many astrophysical sources becomes polarized through electron scattering, which conveys the shape of the last-scattering surface. Spectropolarimetry and imaging polarimetry are powerful yet underutilized techniques that provide insights into the geometry and configuration of unresolved astrophysical objects. These

methods are particularly crucial for understanding high-energy transient events, as they enable analyses of gas distribution and the structure of ejecta or debris. Such information, which is inaccessible through spectroscopy alone, offers essential clues about the underlying progenitor mechanisms, dynamic processes, and physical conditions within these events.

SNe Ia have been previously studied using polarimetry (Wang et al. 2008). Generally, SNe Ia exhibit low polarization in the continuum and comparatively higher polarization in the Si and Ca lines. This suggests that while the overall explosion of SNe Ia is spherical, the intermediate-mass elements are synthesized in clumps. On the other hand, the study of polarimetry in TDEs represents a new frontier. To date, only 2–3 TDEs have documented polarization data. Analyzing the polarization of TDEs could enhance our understanding of the shape and orientation of gas post-disruption, which in turn could provide crucial insights into the sources of optical emission and the timescale of disk formation.

1.5 Thesis Chapters

This thesis is organized as follows. Chapter 2 delves into SNe Ia and spectropolarimetry, using SN 2019ein as a case study to deepen the understanding of the progenitor channels and explosion mechanisms of SNe Ia. Details of spectropolarimetry observations, data reduction, and calculation of polarization are also described. Chapter 3 introduces a comprehensive sample of spectropolarimetric data of SNe Ia, describes the database, and highlights its value through preliminary analyses of the polarimetry of SN 2011fe.

Chapter 4 employs polarimetry techniques on one of the closest TDEs to date, AT 2019qiz, marking one of the first spectropolarimetric studies of TDEs. The next chapter (5) expands on this by presenting imaging polarimetry of several TDEs, aiming to enlarge the sample of TDEs with polarimetric data.

Chapter 6 shifts focus to the related phenomenon of X-ray QPEs, analyzing *Hubble Space Telescope (HST)* images of GSN 069, the host galaxy of the first discovered QPE. This analysis reveals a compact, unresolved source of [O III] emission in the galaxy's nucleus, which is utilized to constrain the characteristics of the gas surrounding the SMBH in GSN 069.

1.6 Other Work

During my tenure as a graduate student, I have engaged in a diverse array of research topics in astrophysics, including exoplanets and transient events. While not all of my projects are thematically aligned with this thesis, here I provide a brief overview of other significant contributions.

- **Tidal Orbital Decay of Hot Jupiters:** In Patra et al. (2020), we conducted an extensive investigation of the orbits of several “hot Jupiter" exoplanets to confirm the longstanding hypothesis that their orbits are gradually shrinking. This work provided definitive evidence of orbital decay in WASP-12 b and established lower limits on the stellar quality factor for numerous other hot Jupiter systems.

- **TDE Dust Echoes:** This ongoing project is focused on modeling the IR light curves following a TDE. The models developed from this work will help ascertain the bolometric luminosity of TDEs, as well as the density and orientation of dust around the SMBH. As progressively more IR TDEs are discovered, the ability to model IR light curves will be extremely helpful.

- **FRB Polarization:** Fast radio bursts (FRBs) are explosive events that last only milliseconds and are primarily observed at radio wavelengths. They exhibit rich and complex polarization patterns. This ongoing work aims to demonstrate that much of this polarization diversity arises from interactions between the radio emission and the plasma along the line of sight, which will improve constraints on the intrinsic polarization properties of FRBs.

- **Undergraduate Mentoring:** I have mentored several undergraduate students, designing and supervising their research projects. I would like to specifically acknowledge the contributions of Efrain Alvarado III, Eli Gendrau-Distler, and Kate Bostow, who have continued the research on hot Jupiter orbital decay. Under my supervision, they wrote a paper that has been submitted to the *Monthly Notices of the Royal Astronomical Society* and has received a favorable review.

Chapter 2

Spectropolarimetry of the Type Ia SN 2019ein Rules Out Significant Global Asphericity of the Ejecta

An earlier version of this article was previously published as Patra, Kishore C.; Yang, Yi; Brink, Thomas G.; Höflich, Peter; Wang, Lifan; Filippenko, Alexei V.; Kasen, Daniel; Baade, Dietrich; Foley, Ryan J.; Maund, Justyn R.; Zheng, WeiKang; Hung, Tiara; Cikota, Aleksandar; Wheeler, J. Craig; Bulla, Mattia, MNRAS, 509, 4058.

2.1 Chapter Abstract

Detailed spectropolarimetric studies may hold the key to probing the explosion mechanisms and the progenitor scenarios of Type Ia supernovae (SNe Ia). We present multi-epoch spectropolarimetry and imaging polarimetry of SN 2019ein, an SN Ia showing high expansion velocities at early phases. The spectropolarimetry sequence spans from ~ -11 to +10 days relative to peak brightness in the *B*-band. We find that the level of the continuum polarization of SN 2019ein, after subtracting estimated interstellar polarization, is in the range 0.0–0.3%, typical for SNe Ia. The polarization position angle remains roughly constant before and after the SN light-curve peak, implying that the inner regions share the same axisymmetry as the outer layers. We observe high polarization ($\sim$ 1%) across both the Si II λ6355 and Ca II near-infrared triplet features. These two lines also display complex polarization modulations. The spectropolarimetric properties of SN 2019ein rule out a significant departure from spherical symmetry of the ejecta for up to a month after the explosion. These observations disfavour merger-induced and double-detonation models for SN 2019ein. The imaging polarimetry shows weak evidence for a modest increase in polarization after $\sim$ 20 days since the *B*-band maximum. If this rise is real and is observed

in other SNe Ia at similar phases, we may have seen, for the first time, an aspherical interior similar to what has been previously observed for SNe IIP. Future polarization observations of SNe Ia extending to post-peak epochs will help to examine the inner structure of the explosion.

2.2 Introduction

During the last half century, Type Ia supernovae (SNe Ia; see Filippenko 1997 and Gal-Yam 2017 for reviews of SNe) have answered (and posed) a myriad of interesting questions in astrophysics. These range from nucleosynthesis, chemical enrichment (Renzini 1999), and heating of the interstellar medium (Ciotti et al. 1991) to the discovery of the accelerating expansion of the universe (Riess et al. 1998; Perlmutter et al. 1999), and more recently the so-called “Hubble tension" (as summarised by Riess 2020). Yet, the nature of the progenitor systems of SNe Ia is still unclear. It has been generally established that the rise of SNe Ia is powered by the thermonuclear runaway of white dwarfs (WDs; see Hoyle & Fowler 1960; Howell 2011; Hillebrandt et al. 2013; Maoz et al. 2014; Höflich 2017; Soker 2019 for recent reviews). However, the exact mechanism by which a WD’s explosion is triggered and propagates through the progenitor still remains poorly understood (Arnett 1969; Nomoto et al. 1976; Khokhlov 1991; Niemeyer et al. 1996; Reinecke et al. 2002; Plewa et al. 2004; Röpke 2007; Pakmor et al. 2011; Seitenzahl et al. 2013).

Multiple channels of progenitors have been theorised, including the double-degenerate scenario in which two WDs merge (Iben & Tutukov 1984; Webbink 1984), the single-degenerate scenario in which a WD accretes matter from a nondegenerate companion until the Chandrasekhar mass ($M_{\rm Ch} \approx 1.4\ M_{\odot}$) is approached (Whelan & Iben 1973), and tidal disruption of a WD by a compact companion and subsequent detonation of the WD (Rosswog et al. 2009; Luminet & Pichon 1989).

Among these progenitor scenarios, a range of explosion mechanisms might be possible: delayed detonation, in which an initial deflagration front transitions to a detonation in a WD (Khokhlov 1991); double detonation, where a thin He layer on the WD detonates first, starting a detonation front in the WD (see, for example, Fink et al. 2010; Taam 1980; Shen et al. 2010); and compressional heating of WDs triggered by the dynamic merger of two C-O WDs (Pakmor et al. 2010; Hayden et al. 2010) or head-on collisions of WDs (Kushnir et al. 2013).

The shape of the ejecta and their circumstellar configuration is spatially unresolvable for extragalactic SN explosions, even with the best of ground-based interferometers[1]. Conventional photometry and spectroscopy provide a way to probe the kinematics and chemical

[1]The minimum resolution required to study a nearby SN, for instance 3 Mpc away with a photosphere 100 au wide, would be $\sim 10\ \mu$as. For comparison, the Event Horizon Telescope can achieve a resolution of $\sim 60\ \mu$as.

structures of SN ejecta and their interaction with any pre-explosion circumstellar matter (CSM; see, for example, Nugent et al. 2011; Gal-Yam et al. 2014). However, these observations only offer crude clues on the structures of the ejecta and the interaction between the ejecta and any existing CSM. Such information is projected and smeared into the single dimension of radial velocity. Fortunately, spectropolarimetry, which measures polarization as a function of wavelength, provides a unique approach to the study of the SN explosion geometry. Any asphericity of the SN ejecta and the distribution of various elements formed in the ejecta are traced by the level of the continuum and the profiles of associated spectral lines in the polarization spectra, respectively. Additionally, the footprint of the interaction between the SN ejecta with any companion and CSM is encoded in the polarization spectra since such processes may create non-spherically- symmetric emission and/or scattering photon sources.

In SN atmospheres, photons are scattered by free electrons (Thomson scattering). The polarization state of the emitted photons is determined when they escape the last-scattering surface, known as the photosphere. A photon that undergoes Thomson scattering will be polarized perpendicularly to the plane of scattering, which is defined as the plane containing the incident and scattered rays. For a spatially-unresolved source, the observed polarization is an integration of the photons' electric vectors (E-vectors) projected in the plane of the sky. If the projected photosphere is circularly symmetric, a complete cancellation of the E-vectors results in zero net polarization. However, if the projected photosphere deviates from circular symmetry, incomplete cancellation of the E-vectors would lead to nonzero polarization across the spectrum. Additionally, any clumps of high-opacity absorbing material present above the photosphere along the observer's line of sight may block parts of the underlying photosphere. Therefore, an incomplete cancellation of the E-vectors will occur across the corresponding spectral lines, further producing nonzero polarization at the extinguished wavelengths.

SN 2019ein [α(J2000) = 13:53:29.11, δ(J2000) = +40:16:31.33] was discovered on 2019 May 1.47 (UT dates are used throughout this paper; Tonry et al. 2019) in the outskirts of the nearby galaxy NGC 5353. The host of SN 2019ein is a lenticular galaxy (Hubble type S0). A redshift of $z = 0.00775$ taken from the NASA/IPAC Extragalactic Database[2] was adopted in this study. The spectrum obtained by the Las Cumbres Observatory (LCO) Global SN project on 2021 May 2.3 (about two weeks before the B-band light-curve peak) shows a very high expansion velocity of $\sim 24,000\,\mathrm{km\,s^{-1}}$ as inferred from the absorption minimum of the Si II λ6355 line. The Ca II near-infrared triplet (hereafter Ca II NIR3) and the O I lines are blended, creating a broad absorption profile. Curiously, the entire spectrum was slightly blueshifted with respect to the host-galaxy redshift, with the emission peaks of Si II, Ca II, and S II exhibiting velocities $\sim 10,000\,\mathrm{km\,s^{-1}}$ toward the observer. Pellegrino et al. (2020) suggested that the apparent blueshift may be caused by an asymmetric explo-

[2] https://ned.ipac.caltech.edu

sion resulting in enhanced abundance of material at high velocities or due to optical-depth effects in the photosphere, in which most of the flux comes from material moving along the SN-Earth line of sight. The rise time of SN 2019ein was short (15.37 ± 0.55 days), after which the SN faded rapidly with a 15 day post-peak B-band magnitude decline (Phillips 1993) $\Delta m_{15}(B) = 1.36 \pm 0.02$ mag (Kawabata et al. 2020).

These features put SN 2019ein in the rare company of high-velocity SNe Ia like SNe 2004dt and 2006X, for which spectropolarimetric data have been obtained (Wang et al. 2006; Patat et al. 2009). In this work, we present five epochs of spectropolarimetry of SN 2019ein. We describe our observations in Section 4.3 and present our results along with the analysis in Section 2.4. We discuss the interpretations of the data in Section 6.6 and provide a concluding summary in Section 2.6.

2.3 Observations and data reduction

2.3.1 Kast Spectropolarimetry

Spectropolarimetry of SN 2019ein was obtained using the polarimetry mode of the Kast double spectrograph on the Shane 3 m telescope at Lick Observatory (Miller et al. 1988). In the polarimetry mode, the light beam incident on the spectrograph is passed through a rotatable, half-wave plate and then through a Wollaston Prism. The prism splits the incident light into two perpendicularly polarized components, named the ordinary and the extraordinary beams, which appear on the detector as two parallel traces. Only the red channel of Kast was used for spectropolarimetry. A GG455 order-sorting filter was in place, blocking all first-order light below ~4600 Å and all second-order light below ~9800 Å. The usable wavelength range of the setup was 4600–9000 Å. Observations were made with the 300 lines mm^{-1} grating and the 3″-wide slit, resulting in a resolution of $\Delta\lambda \approx 18$ Å ($\sim 800\,\mathrm{km\,s}^{-1}$) at the central wavelength ~ 6800 Å.

Flatfield and arc-lamp exposures were obtained at the beginning of the observation night. The flatfield spectra were produced by the reflection of the light from an incandescent lamp off of the inner surface of the dome.

SN 2019ein and polarization standard stars were observed each night. Four exposures were carried out at retarder-plate angles of 0°, 45°, 22.5°, and 67.5°. Multiple sets of polarimetry exposures were obtained for SN 2019ein to achieve higher signal-to-noise ratios (S/N). Since all observations were carried out at small airmasses ($\lesssim 1.25$; see Table 2.1), we aligned the slit to the position angle of 180° (north-south direction). Because Kast does not have an atmospheric dispersion compensator (ADC) to atone for the differential loss of blue light (Filippenko 1982), the following sanity check was carried out. For each night, we compared the Stokes parameters measured for different sets of spectropolarimetry with the values derived for the set obtained at the smallest airmass, typically 1.05. The Stokes

parameters for each set were consistent within the associated uncertainties, suggesting a negligible effect on the polarization measurement from the loss of blue light.

Our nightly observations of the unpolarized standard star HD 110897 confirmed the low instrumental polarization of the Kast spectrograph (Sec. 2.4.2). The polarizance test to determine the instrumental response to 100% linearly polarized light was done by observing the same unpolarized standard star through a polarizing filter. Each night we also conducted spectropolarimetry of two polarization standard stars chosen among HD 154445, HD 161056, and HD 155528 to determine the accuracy of polarimetric measurements (see Sec. 2.4.2 for more details). A polarization "probe star" was also observed to estimate the Galactic interstellar polarization (see Sec. 2.4.3).

Extraction of the ordinary and the extraordinary beams was carried out following standard techniques for CCD processing and spectrum extraction within IRAF[3]. The images were bias subtracted using an overscan region. Cosmic ray hits on the detector were removed with *L.A.Cosmic* (van Dokkum 2001). For each night, flatfield images were combined and normalised by a low-order spline function to fit the continuum before applying to the science images. Then we used the prescription of Horne (1986) to optimally extract each spectrum independently from the science images with apertures typically set to width at $\sim$ 1–2% of the maximum of the spectrum profile. The background apertures were usually 5–10 pixels wide and placed 2–3 times the value of the full width at half-maximum intensity (FWHM) away from the profile centre.

Wavelength calibration was conducted separately for the ordinary and extraordinary beams in each individual exposure (all four retarder-plate angles) using lamp exposures. Small wavelength adjustments determined from the night-sky lines in the object frames were also applied to fine tune the wavelength calibration. A typical root-mean-square (RMS) accuracy of $\sim$ 0.2 Å was achieved. Flux calibration of the ordinary and extraordinary beams of the SN was applied using the corresponding beam of a flux standard star observed at a similar airmass. We fit splines to the continuum of the flux-standard spectrum to generate a "sensitivity function" that maps CCD counts to the flux at each wavelength. This mapping function was then applied to the SN spectra. Correction for telluric absorption was carried out by interpolating over the atmospheric absorption regions of the flux-standard spectrum.

[3]IRAF is distributed by the National Optical Astronomy Observatories, which are operated by the Association of Universities for Research in Astronomy, Inc., under cooperative agreement with the National Science Foundation (NSF).

Table 2.1: Journal of spectropolarimetric observations.

UT Date (MM-DD-YYYY)	MJD	Phase[a] (days)	Airmass Range	Avg. Seeing (arcsec)	Wavelength Range (Å)	Exposure Time[b] (s)
05-05-2019	58607.3	−10.9	1.04 –> 1.03	1.30	4570–9000	4×1080
05-06-2019	58608.3	−9.9	1.04 –> 1.13	1.21	4570–9000	4×1080
05-12-2019	58614.3	−3.9	1.01 –> 1.14	1.63	4570–9000	4×1080
05-13-2019	58615.4	−2.9	1.03 –> 1.13	1.29	4570–9000	4×1080
05-26-2019	58628.4	+10.1	1.09 –> 1.25	1.86	4570–9000	4×1080

[a]Relative to *B*-band peak brightness at MJD 58618.2 (Kawabata et al. 2020).
[b]Number of waveplate positions × exposure time at each position.

2.3.2 RINGO3 Imaging Polarimetry

In this work, we adopted the imaging polarimetry of SN 2019ein from Maund et al. (2021). Details of the RINGO3 observations and data reduction are provided by Maund et al. (2021). In brief, they obtained the data using the Liverpool Telescope (LT) located on the Canary Island of La Palma, with the RINGO3 polarimeter (Arnold et al. 2012). Observations were carried out in three cameras optimised to integrate over the following wavelength ranges: b, 3500–6400 Å; g, 6500–7600 Å; and r, 7700–10000 Å. Interstellar polarization was subtracted from the Stokes parameters measured by Maund et al. (2021) (see Sec. 2.4.7 for details). The Stokes parameters, polarization, and its position angle are shown in Table 2.2.

2.4 Analysis and results

2.4.1 Calculating the Stokes q and u

We express the normalised Stokes parameters as $q = Q/I$ and $u = U/I$, where Q and U are the differences in flux with E-vector oscillating in two perpendicular directions and I is the total flux. U measures polarization along angles that are rotated by 45° with respect to those measured by Q.

We calculate q and u from two sets of spectra obtained with the waveplate at [0°, 45°], and [22°.5, 67°.5], respectively. From the ordinary (o) and the extraordinary (e) flux beams (f), q_o and q_e can be defined as

$$q_o = \frac{f_{o,0} - f_{o,45}}{f_{o,0} + f_{o,45}} \text{ and } q_e = \frac{f_{e,0} - f_{e,45}}{f_{e,0} + f_{e,45}}, \tag{2.1}$$

respectively, which are then averaged to calculate Stokes q. Similarly, we calculate Stokes u using the exposures at the other set of waveplate positions. The observed polarization is then given by

$$p_{\rm obs} = \sqrt{q^2 + u^2} \tag{2.2}$$

and the polarization position angle (PA) is

$$PA_{\rm obs} = \frac{1}{2} \arctan\left(\frac{u}{q}\right). \tag{2.3}$$

The polarization defined this way is positive-definite and biased toward higher polarization, especially in the low S/N regime. The final derived polarization was achieved after a debiasing procedure following Wang et al. (1997):

$$p = \left(p_{\rm obs} - \frac{\sigma_p^2}{p_{\rm obs}}\right) \times h(p_{\rm obs} - \sigma_p) \text{ and } PA = PA_{\rm obs}, \tag{2.4}$$

where σ_p denotes the 1σ uncertainty in p and h is the Heaviside step function. The flux spectrum is calculated by averaging all the spectra of o-rays and e-rays used in deriving q and u. Figures 2.1–2.5 show the measured Stokes q, u, p, PA, and total flux at each epoch.

2.4.2 Polarimetric Calibration

The nightly-measured Stokes q and u of the unpolarized standard star HD 110897 are consistent with a level of $< 0.05\%$, indicating a low instrumental polarization and a high stability of the Kast spectropolarimeter over time. In the polarizance test with the same standard star, we determined that the polarimetric response of the instrument is larger than 99.5% across the entire wavelength range (4600–9000 Å) and therefore does not necessitate further correction. The polarization position angle of SN 2019ein was corrected as follows:

$$q_{\rm corr} = p_{\rm obs}\ q_{\rm obs}\ \cos 2(PA_{\rm obs} - PA_i), u_{\rm corr} = p_{\rm obs}\ u_{\rm obs}\ \cos 2(PA_{\rm obs} - PA_i),$$

where PA_i is the position angle of the instrumental polarization determined from the polarizance test.

The polarization and position angle measurements of the two high-polarization standards observed on each night were respectively found to be within 0.1% and 3° of the references (Schmidt et al. 1992; Wolff et al. 1996).

2.4.3 Interstellar Polarization

Light passing through interstellar dust clouds is polarized through dichroic extinction by nonspherical paramagnetic dust grains present along the line of sight. The contribution to polarization by dust, namely the interstellar polarization (ISP), must be removed to determine the intrinsic polarization of the source. Although several approaches have been commonly used to estimate the ISP along the SN-Earth line of sight (see, for example, Stevance et al. 2019; Yang et al. 2020), the exact level of the ISP contribution to the observed polarization of SN 2019ein is generally uncertain.

Serkowski et al. (1975) showed that the Galactic ISP can be constrained to $p_{\rm ISP} < 9 \times E(B-V)$ %. The Milky Way colour excess $E(B-V)_{\rm MW}$ along the line of sight of SN 2019ein is 0.011 mag (Schlafly & Finkbeiner 2011), constraining $\rm ISP_{MW}$ to $< 0.1\%$. This upper limit is commensurate with the measured polarization of an ISP "probe star"[4] – an intrinsically unpolarized star within 1of SN 2019ein that probes at least 150 pc scale height of the Galactic interstellar medium (ISM). The Stokes q and u measured for the probe star were found to be $< 0.05\%$ in the continuum wavelength range of SN 2019ein, indicating low contribution from Galactic reddening.

[4]We observed the star *Gaia DR2 1497177392672672128*.

An upper limit of the ISP from the host galaxy of SN 2019ein (NGC 5353) can be estimated based on the host reddening $E(B-V)_{\rm host} = 0.09 \pm 0.02$ mag (Kawabata et al. 2020). Accounting for both the Galactic and SN 2019ein-host dust, we place an upper limit of $p_{\rm ISP} < 0.9\%$ along the SN-Earth line of sight. Such a value of ISP is higher than the continuum polarization level seen in SN 2019ein; thus, interstellar dust could potentially account for all of the continuum polarization of SN 2019ein. The caveat, however, is that Serkowski's law may not be applicable to all galaxies because different dust properties could lead to different efficiencies for ISP (Leonard et al. 2002). Therefore, we employ a more direct approach by following the method used by Yang et al. (2020) to estimate the ISP Stokes parameters $q_{\rm ISP}$ and $u_{\rm ISP}$.

We consider the wavelength region 4800–5600 Å in the spectrum when the SN is near its peak brightness. This region is expected to be intrinsically depolarized owing to multiple overlapping Fe absorption features, which create a "line blanketing" effect whose opacity dominates over electron scattering (Howell et al. 2001; Maund et al. 2013). We set the level of Stokes q and u to 0 within this wavelength range on day −2.9 (see Fig. 2.4), giving us an estimate of $q_{\rm ISP} \approx -0.24\%$ and $u_{\rm ISP} \approx 0.19\%$. We note that these estimates are consistent with the upper limit derived above using Serkowski's rule. These ISP values were subtracted from the observed q and u on each night and the polarization and the position angle were subsequently recalculated (see Table 2.2). We note that owing to the relatively low level of expected ISP, only a wavelength-independent ISP estimation is presented. We will discuss the ISP-corrected continuum and line polarization of SN 2019ein in Sections 2.4.4 and 2.4.5, respectively.

Table 2.2: Summary of polarimetry results.

MJD	Phase[a] (d)	Instrument	q(%)	u(%)	p(%)	PA(deg)	q(%)	u(%)	p(%)	PA(deg)
			(observed)				(ISP corrected)			
58607.3	−10.9	Kast	−0.23(07)	0.05(07)	0.21(07)	83(9)	0.01(07)	−0.14(07)	0.10(07)	138(15)
58608.3	−9.9	Kast	−0.18(05)	0.09(05)	0.19(05)	77(7)	0.06(05)	−0.10(05)	0.10(05)	151(12)
58612.9	−5.3	RINGO3: *b*	−0.50(16)	0.43(15)	0.64(15)	70(7)	−0.13(25)	−0.04(24)	< 0.01	99(> 360)
58614.3	−3.9	Kast	−0.22(02)	0.22(02)	0.31(02)	68(2)	0.02(02)	0.03(02)	0.02(02)	210(18)
58615.4	−2.9	Kast	−0.23(04)	0.23(04)	0.32(04)	68(3)	0.01(04)	0.03(04)	0.00(04)	215(30)
58620.0	1.8	RINGO3: *b*	−0.33(15)	0.64(16)	0.70(15)	59(6)	0.04(24)	0.17(25)	< 0.01	219(> 360)
58622.9	4.7	RINGO3: *b*	−0.28(15)	0.34(13)	0.42(12)	65(9)	0.09(24)	−0.13(22)	< 0.01	152(> 360)
58628.4	10.1	Kast	−0.07(06)	−0.05(07)	0.03(07)	108(24)	0.17(06)	−0.24(07)	0.28(07)	153(7)
58630.9	12.7	RINGO3: *b*	−0.15(24)	1.14(26)	1.12(25)	49(6)	0.22(33)	0.67(35)	0.54(34)	215(17)
58639.0	20.8	RINGO3: *b*	−0.47(23)	−0.91(23)	0.99(22)	122(7)	−0.10(32)	−1.38(32)	1.31(32)	133(6)

[a]Relative to *B*-band peak brightness at MJD 58618.2 (Kawabata et al. 2020).

2.4.4 Continuum Polarization

Aspherical distribution of electrons, for instance an ellipsoidal photosphere, will cause imperfect cancellation of polarization E-vectors, leading to a nonzero continuum polarization (Höflich 1991, 1995; Bulla et al. 2015; Stevance et al. 2019). SNe Ia typically show low continuum polarization ($\lesssim 0.3\%$; see, for example, Wang & Wheeler 2008; Yang et al. 2020), indicating that SNe Ia tend to be remarkably close to being spherical.

The continuum polarization of SN 2019ein and the associated uncertainty were estimated by binning the Stokes parameters over a wavelength range of 6400–7150 Å following a procedure similar to that described by Yang et al. (2020). The selected spectral region is known to be free from strong absorption features (Patat et al. 2009). The uncertainty was correspondingly binned.

The continuum polarization on days −10.9 and −9.9 is low with values of $p_{\mathrm{cont},-10.9\mathrm{d}} = 0.10 \pm 0.07\%$ and $p_{\mathrm{cont},-9.9\mathrm{d}} = 0.10 \pm 0.05\%$, respectively (Figs. 2.1 and 2.2). The polarization is consistent with 0 as the SN approaches maximum brightness around day −3.9 and day −2.9 (Figs. 2.3 and 2.4). After peak brightness, polarization increases slightly, reaching $p_{\mathrm{cont},+10.1\mathrm{d}} = 0.28 \pm 0.07\%$ (Fig. 2.5). We note that these values are consistent with infrared spectropolarimetry of SN 2019ein, which found a 3σ upper limit on polarization of 1.2% around the SN peak brightness (Tinyanont et al. 2021).

The measured continuum polarization position angle (PA), which represents the position of global axisymmetry of the ejecta, remains fairly consistent before and after peak brightness, hovering around 150°. Even though the PA on days −3.9 and −2.9 is apparently larger ($\sim 210°$), we note that the polarization is so close to zero that the PA is essentially undetermined on those days.

2.4.5 Line Polarization

Polarization signal at specific spectral lines arises due to the presence of clumps of material above the photosphere. The absorbing material partially obscures the underlying Thomson-scattering photosphere, resulting in an excess of polarization superimposed on the continuum polarization over the range of the absorption wavelengths. Below, we present the polarization of three absorption features as follows.

1. Si II λ6355: We observe weak line polarization ($0.5 \pm 0.4\%$) on day −10.9, whereas no significant line polarization was detected on day −9.9. On days −3.9 and −2.9, we see strong line polarization, which reaches its peak value of $\sim 1\%$ at an expansion velocity of $\sim 17,000\,\mathrm{km\,s^{-1}}$. The strong line polarization persists into day 10.1, at an expansion velocity of $\sim 13,600\,\mathrm{km\,s^{-1}}$.

2. O I λ7774: No significant line polarization was seen at any phase.

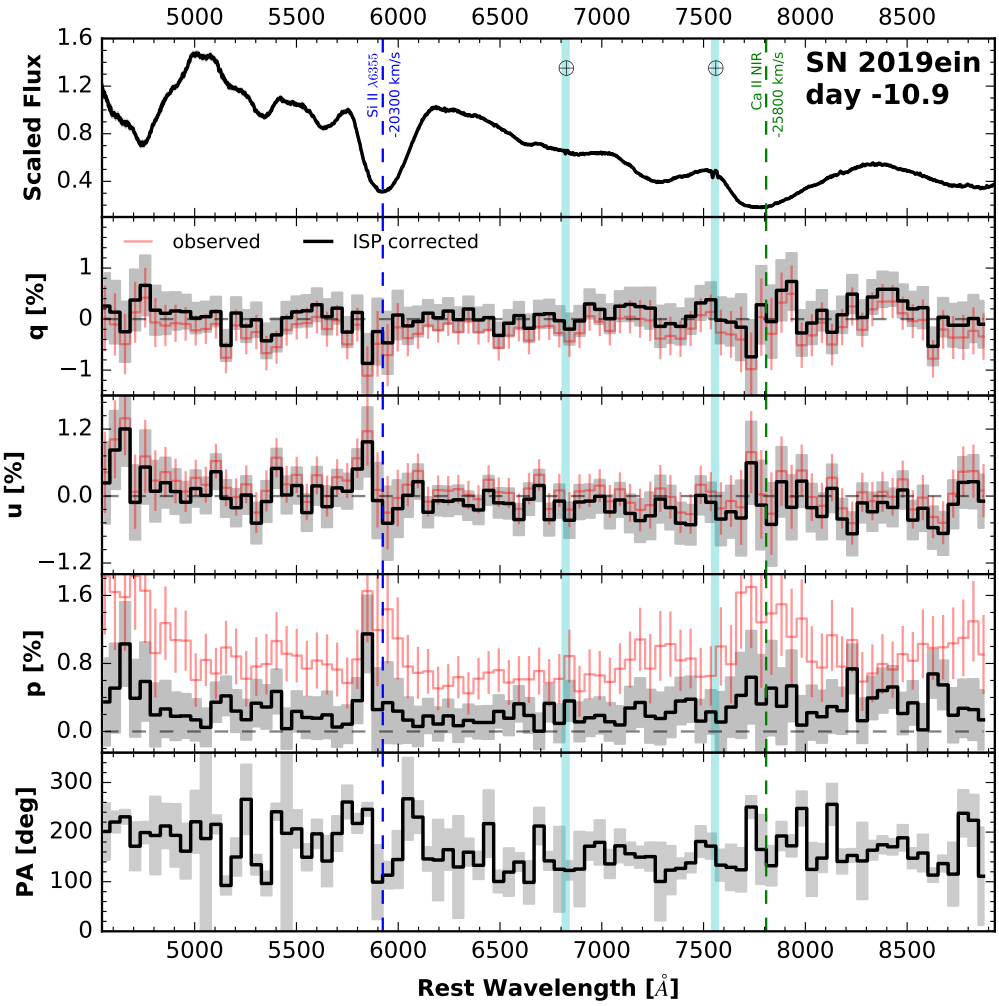

Figure 2.1: Spectropolarimetry of SN 2019ein at day −10.9 relative to the *B*-band peak brightness at MJD 58618.2 (Kawabata et al. 2020). The cyan vertical bands represent the regions of telluric correction. The panels below the total-flux spectrum represent the polarimetry before (red) and after (black) the ISP correction. The grey-shaded area indicates the associated 1σ uncertainty. The *PA* panel shows only the polarization position angle after ISP correction. With the exception of the flux spectrum, we use 50 Å binning for the purpose of presentation.

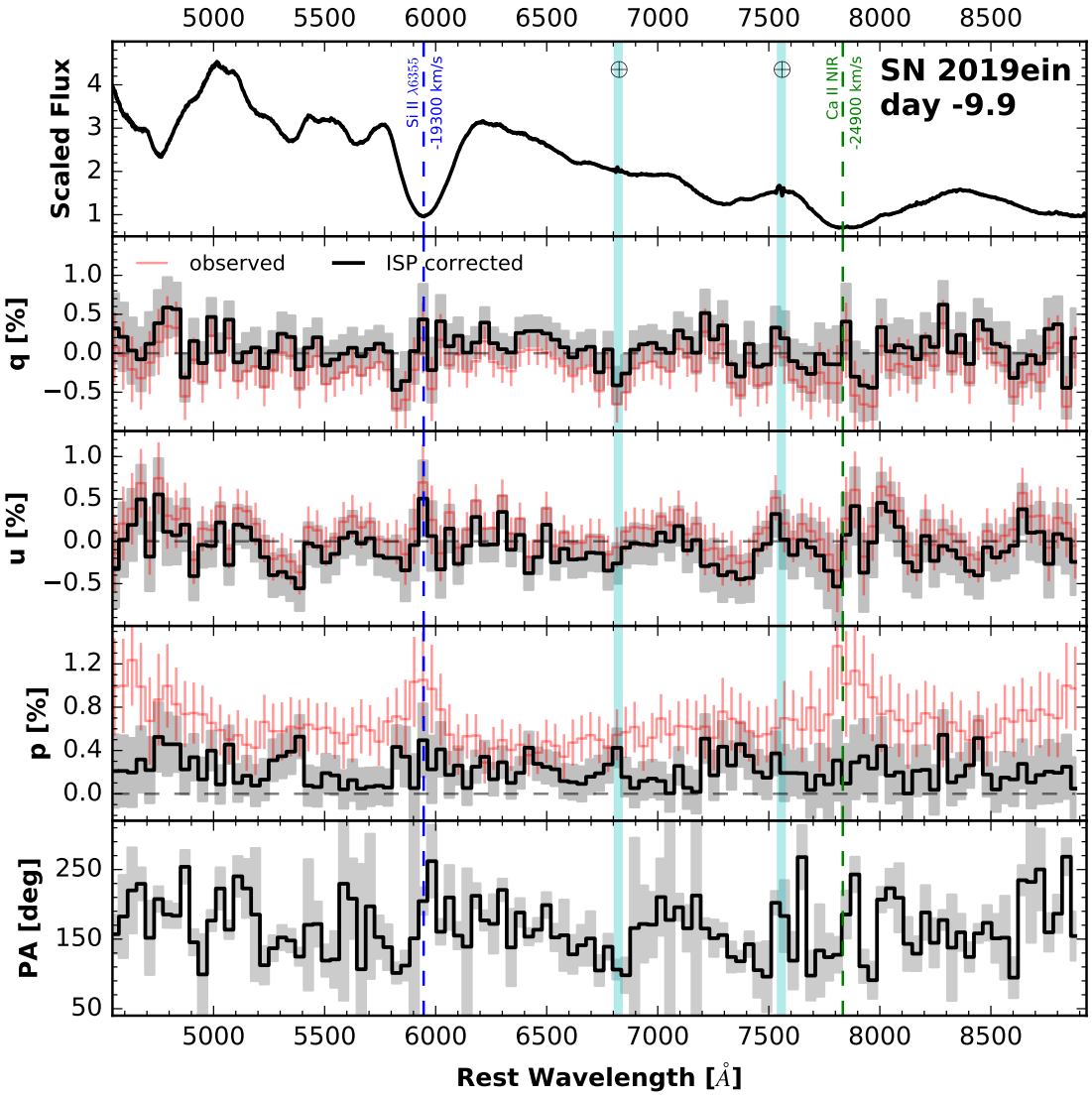

Figure 2.2: Similar to Figure 2.1 but for day −9.9. We use 40 Å binning for the purpose of presentation.

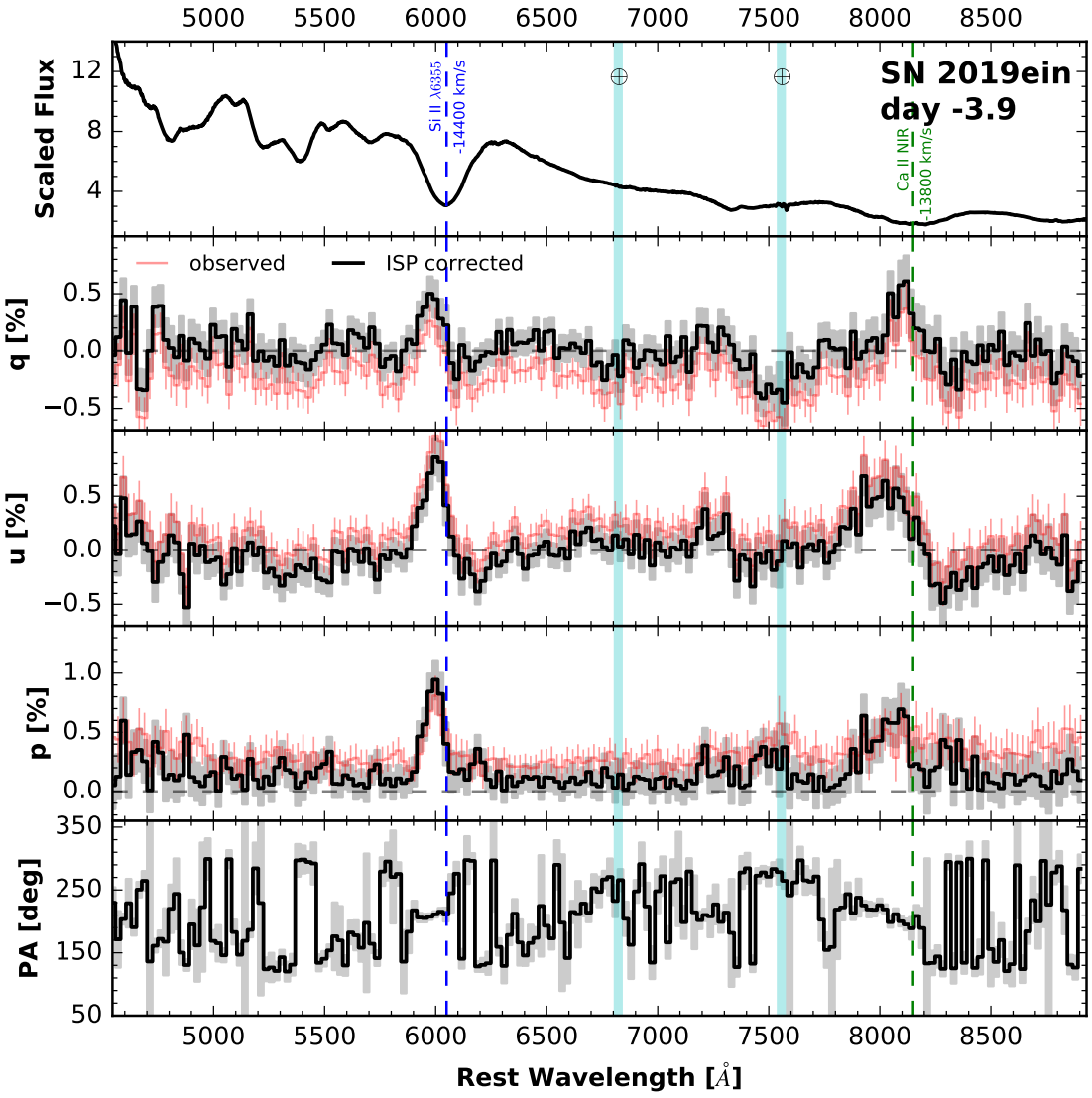

Figure 2.3: Similar to Fig. 2.1 but for day −3.9. We use 25 Å binning for the purpose of presentation.

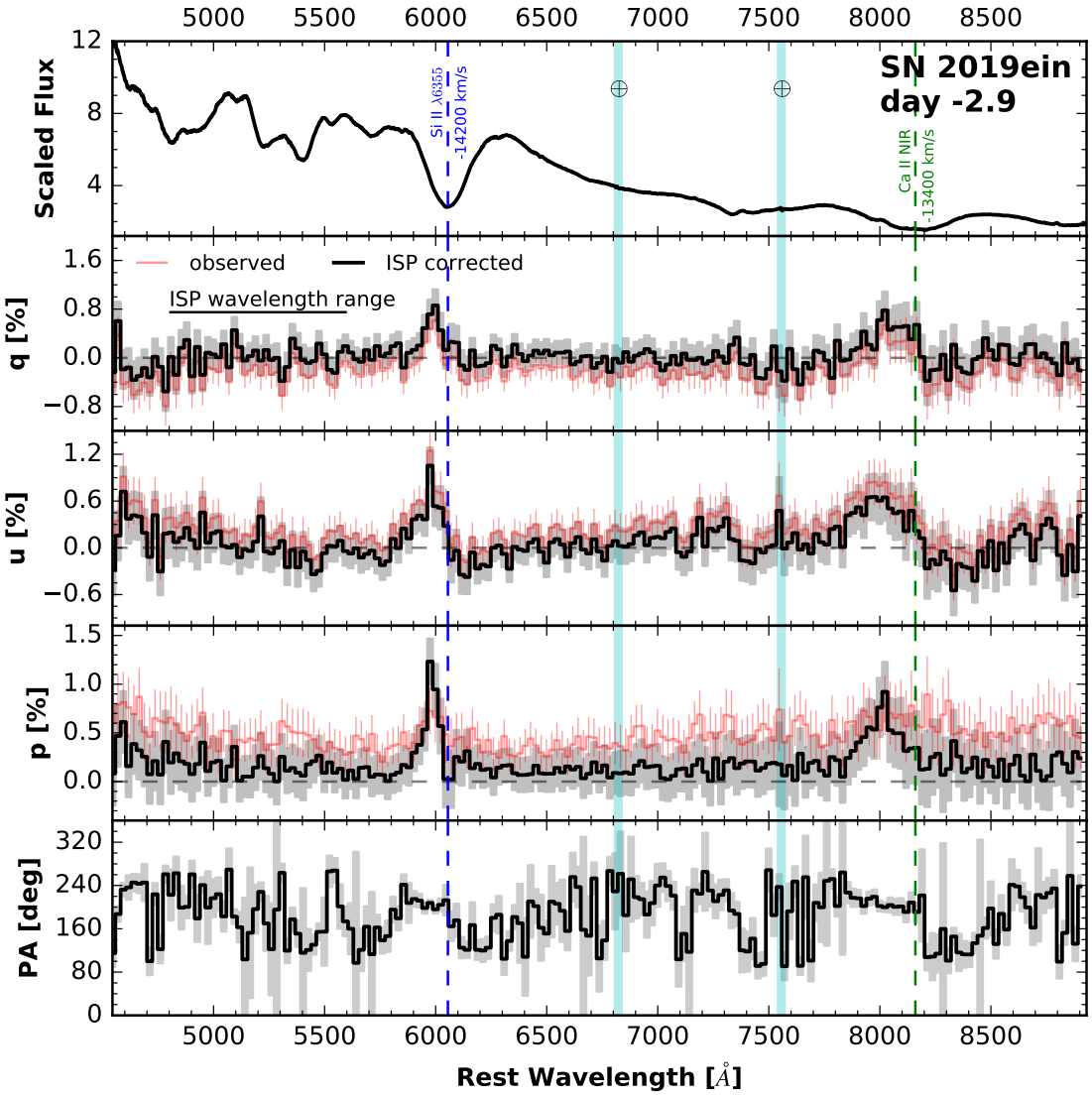

Figure 2.4: Similar to Fig. 2.1 but for day −2.9. We use 25 Å binning for the purpose of presentation. The wavelength region 4800–5600 Å was used to estimate the ISP as described in Section 2.4.3.

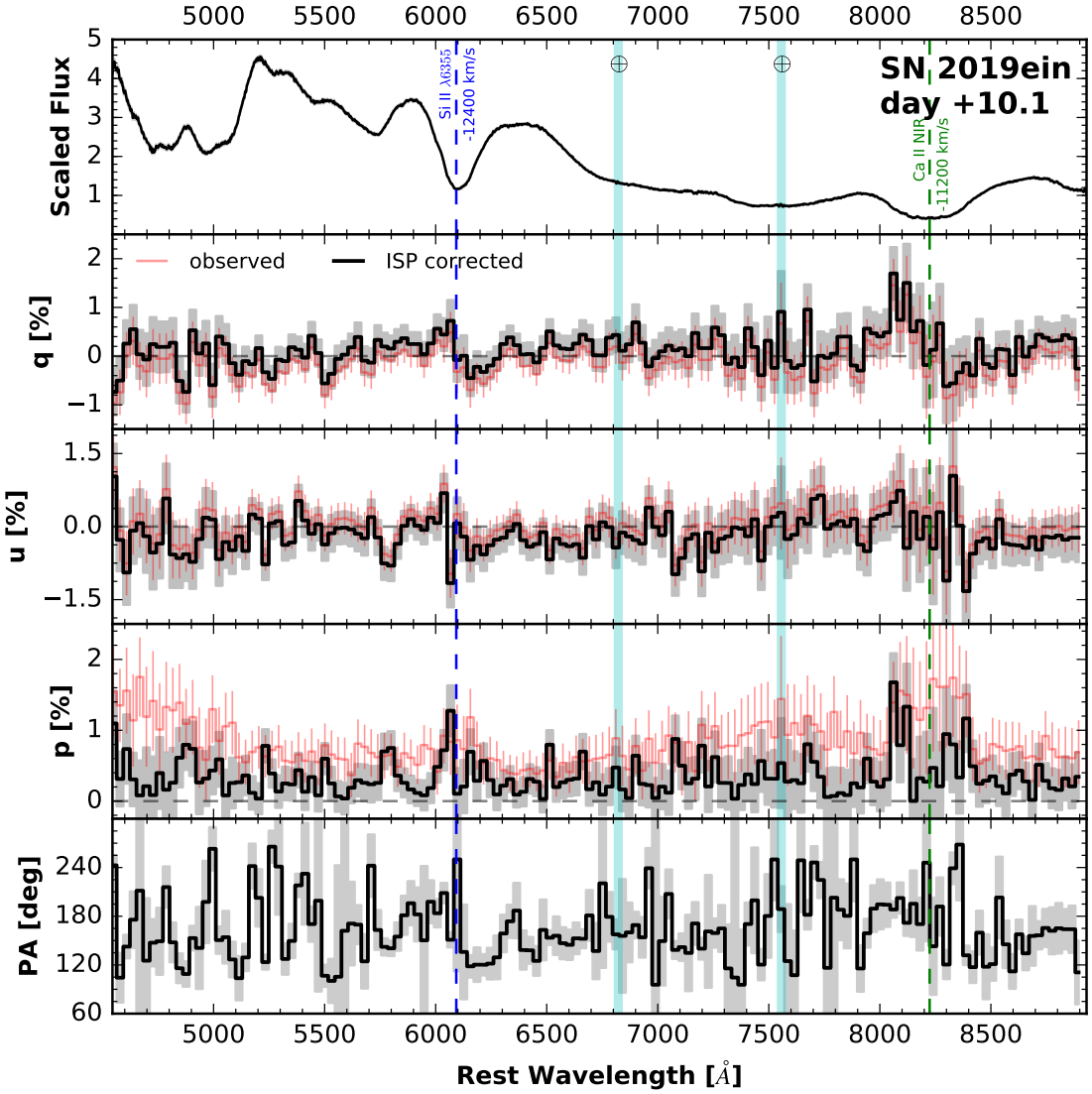

Figure 2.5: Similar to Fig. 2.1 but for day +10.1. We use 30 Å binning for the purpose of presentation.

3. Ca II NIR3: Similarly to Si II, no significant line polarization was observed on days −10.9 and −9.9. In contrast, on days −3.9 and −2.9, we see strong line polarization, reaching its peak value of $\sim$ 0.8% at an expansion velocity of $\sim$ $18,000\,\mathrm{km\,s^{-1}}$. The strong line polarization continues into day 10.1, reaching up to $\sim$ 1.5% at $17{,}000\,\mathrm{km\,s^{-1}}$.

Starting on day −3.9 and thereafter, both Si II and Ca II show a complex structure in the polarization spectra, likely associated with high-velocity (HV) and normal-velocity (NV) components. For example, at day +10.1, the polarization across Ca II NIR3 reached two local maxima at $-17{,}000\,\mathrm{km\,s^{-1}}$ and $-5900\,\mathrm{km\,s^{-1}}$. The emergence of the line polarization of both the HV and NV components over time may result from an increase of Si II and Ca II opacity from larger to smaller radii.

2.4.6 The q–u Plane and the Dominant Axis

Table 2.3: Fitted parameters for the dominant axes.

Phase (days)	$\alpha_{\rm cont}$	$\beta_{\rm cont}$	$\alpha_{\rm Si\ II}$	$\beta_{\rm Si\ II}$	Velocity Range (-10^3 km s^{-1})	$\alpha_{\rm Ca\ II\ NIR3}$	$\beta_{\rm Ca\ II\ NIR3}$	Velocity Range (-10^3 km s^{-1})
−10.9	0.81(21)	−0.15(04)	−2.23(1.35)	−0.12(23)	28.6 – 9.7	−0.74(24)	−0.11(07)	34.8 – 6.7
−9.9	4.68(2.62)	−0.47(24)	0.99(49)	−0.10(09)	28.5 – 7.3	0.87(28)	−0.08(06)	34.8 – 6.7
−3.9	0.33(09)	−0.04(01)	1.95(27)	−0.06(05)	23.9 – 5.0	2.24(52)	0.00(08)	26.1 – 3.2
−2.9	−0.94(14)	0.03(02)	1.37(24)	−0.09(06)	23.8 – 3.9	1.33(23)	−0.01(07)	26.1 – 3.2
+10.1	0.02(13)	−0.20(04)	0.90(31)	−0.23(08)	21.5 – 2.6	0.62(11)	−0.28(06)	22.5 – 0.3

Plotting the Stokes parameters in the q–u plane allows us to examine the axisymmetry of the continuum and various spectral features. If the SN ejecta are smooth and axisymmetric, the data points should fall along a straight line called the "dominant axis" (Wang et al. 2001, 2003). Deviations from the dominant axis in the perpendicular direction represent departures from axisymmetry and clumpiness of the ejecta. The dominant axis is determined by

$$u = \alpha q + \beta, \tag{2.5}$$

where α and β are the fitted parameters from an error-weighted orthogonal distance regression. In Figure 2.6, we present the polarization in the q–u plane in the continuum as well as for Si II λ6355 and Ca II NIR3. We omitted the Si II and Ca II lines when plotting the continuum q and u in the wavelength range 4700–8750 Å. The fitted parameters α and β that characterise the dominant axes are given in Table 2.3.

As suggested by the values of χ^2/DoF in Figure 2.6, the departure from the dominant axis fitted across the line profile indicates a significant clumpiness in the Si II-rich ejecta on days −10.9 and −9.9. Considering the relatively large values of χ^2/DoF, it is ambiguous whether a dominant axis is present at early times. The absence of a clear dominant axis together with the measured low polarization suggests that any Si II-rich clumps are fairly uniformly distributed in the ejecta at early times, when the photosphere only intersects with the outermost part of the ejecta. Axial symmetry is evident on days −3.9 and −2.9 for Si II when the SN is near its peak brightness. However, the axial symmetry becomes weak and clumpiness increases again around day +10. Ca II shows an overall higher degree of clumpiness compared to Si II. Ca II also exhibits weak axial symmetry at early times. However, as time progresses, Ca II settles onto a more prominent symmetry axis. Unlike Si II, Ca II continues to exhibit high axial symmetry at day +10. The symmetry axes of both Si II and Ca II are roughly aligned with each other and remain fairly constant starting on day −10 and thereafter.

As seen in the left panels of Figure 2.6, no clear dominant axis can be identified in the continuum at any epoch. The data points form a cloud centred near the origin. This strengthens the case that even though the overall ejecta geometry is spherical, the polarization in Si II and Ca II is due to clumps of explosively synthesised material.

2.4.7 Polarization Time Series

We build a temporal series of polarization measurements of SN 2019ein by combining the Kast spectropolarimetry and the RINGO3 imaging polarimetry. In order to compare the polarization measured by the two instruments, we binned the Kast spectropolarimetry over the RINGO3 b, g, and r filter passbands. This process estimates the equivalent imaging polarimetry data points in RINGO3 filters. In this way, we built the polarimetric dataset with a time baseline from −11 to 21 days relative to the B-band light-curve peak of SN 2019ein.

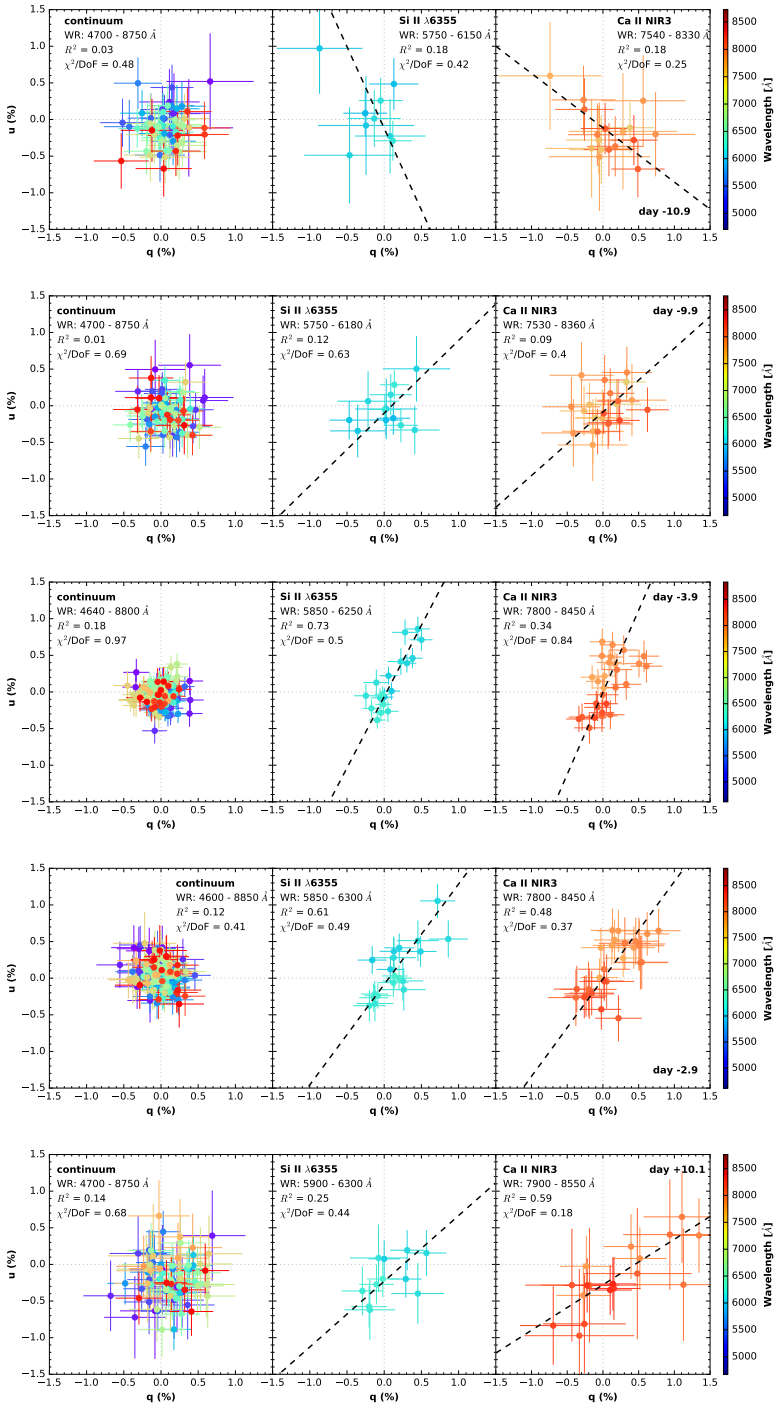

Figure 2.6: Polarization in the Stokes q–u plane. The Si II λ6355 and Ca II NIR3 lines were omited from the left-side panels labeled "continuum". The dashed lines in the "Si II λ6355" and the "Ca II NIR3" panels represent the dominant axes for the labeled absorption features.

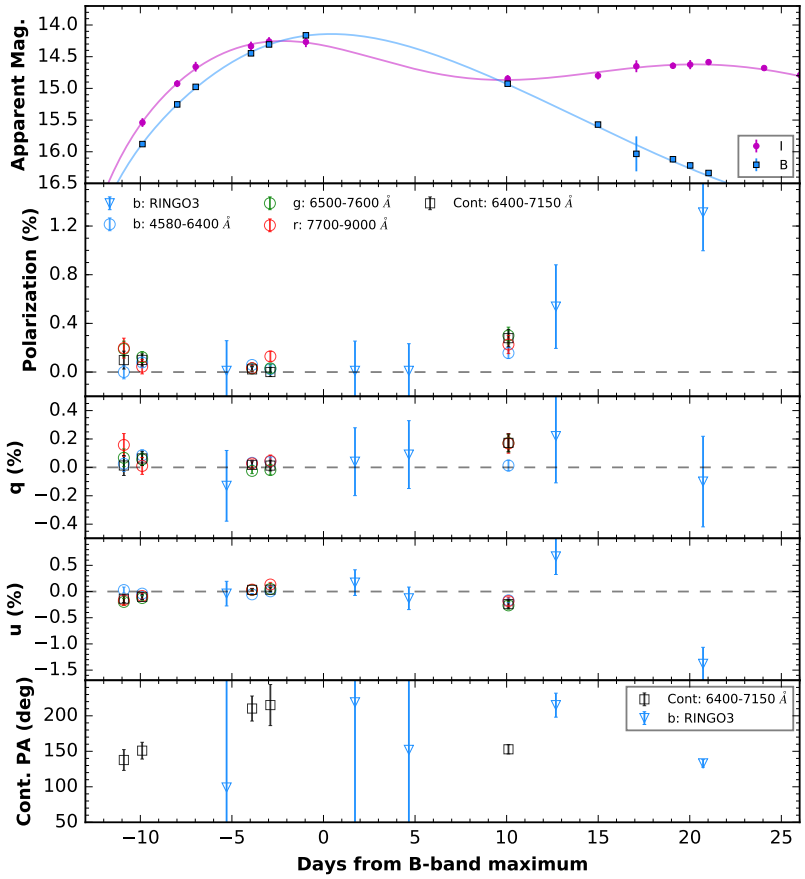

Figure 2.7: Polarization vs. time. The polarization and *PA* have been corrected for the ISP. The black squares represent the continuum polarization and *PA* from the Kast spectropolarimeter. The red, blue, and green circles show the polarization measured by Kast in different wavelength regions: blue (4580–6400 Å), green (6500–7600 Å), and red (7700–9000 Å). The blue inverted triangles show polarization and *PA* measured by RINGO3 in the blue channel with wavelength range 3500–6400 Å. The light curves in the top panel were obtained by KAIT at Lick Observatory.

The broad-band polarization from Kast was derived by integrating over the wavelength of the filter-transmission-weighted polarized flux.

The combined polarization time series is presented in Figure 2.7. The top panel displays two light curves obtained in the Landolt I and B bands with the Katzman Automatic Imaging Telescope (KAIT; Filippenko et al. 2001) at Lick Observatory. The middle panel shows polarization over time. The red, blue, and green circles represent the synthesised Kast polarization in wavelength ranges that roughly match the three channels of RINGO3. The black squares present the Kast continuum polarization in the wavelength range 6400–7150 Å. We note that the b and r bins include the polarization of the Si II λ6355 and Ca II NIR3 features, respectively. The blue inverted triangles show the polarization measured by the blue channel of RINGO3. The bottom panel provides the measured PA in the continuum region (6400–7150 Å) by Kast and by the blue channel of RINGO3. The polarimetry presented here has been ISP corrected. Since we do not know the exact magnitude of any systematic bias (for example, instrumental polarization) in RINGO3 measurements, we employed a different strategy to account for ISP and any systematic bias: we calculated the mean q and u from the three epochs within ~ 5 days of the B-band peak brightness (days −5.3, +1.8, and +4.7; see Table 2.2), which gives $q_{\rm ISP+sys} \approx -0.37\%$ and $u_{\rm ISP+sys} \approx 0.47\%$. We then subtracted the averaged q and u from the observed Stokes parameters of all RINGO3 data under the assumption that SNe Ia exhibit effectively zero continuum polarization near peak brightness. This assumption is validated independently by the Kast spectropolarimetry of SN 2019ein on days −2.9 and −3.9. We also propagated the uncertainty of ISP subtraction into the final calculations of p and PA.

2.5 Discussion

A nonzero continuum polarization may result from either an overall inhomogeneous electron density distribution or a nonspherical heating source. The latter case was seen in models of Bulla et al. (2016a,b) for SNe Ia, and has also been used to explain the observed increase in polarization during the plateau phase of SNe IIP, in which an aspherical ionisation front of ^{56}Ni is typically present (Höflich et al. 1996).

Overall, the polarization properties of SN 2019ein before its peak luminosity are consistent with the typical behaviour of SNe Ia. For example, the continuum polarization is $< 0.2\%$. Distinct line polarization, which is typically on the order of 1%, can also be identified across some prominent spectral lines including Si II, Fe II, and Ca II (Wang & Wheeler 2008). The asymmetric distribution of the intermediate-mass elements (IMEs, $9 \leqslant Z \leqslant 20$, including Si, Ca, S, and Mg) inferred from the line polarization is indicative of sufficient outward mixing. IMEs generated in the nuclear burning can also be produced at higher velocities compared to the SN ejecta. In thermonuclear SNe, below the production zone of the IMEs, the inner burning region is surrounded by C and O from the progen-

itor WD. The energy input is given by the radioactive decay chain of ^{56}Ni→^{56}Co→^{56}Fe, which is initiated by the nucleosynthesis of ^{56}Ni as the main product of the silicon-burning process. An asymmetric ^{56}Ni distribution hence results in an asymmetric energy source.

The low line and continuum polarization at early times (day ~ -11) do not support the idea put forward by Pellegrino et al. (2020) that the bluesfhited emission peaks in early-time spectra are due to an aspherical explosion enhancing abundance of material at high velocities. Furthermore, the lack of a clear dominant axis in the q–u plane at early times indicates that even if clumps of high-velocity material are present, they must be fairly uniformly distributed in the outer ejecta. We cannot, however, rule out the possibility that the apparent blueshift is due to optical-depth effects arising from a steep density profile in the ejecta (Pellegrino et al. 2020).

As seen in the bottom panel of Figure 2.7, we do not identify significant variation in PA at different epochs. We note that near peak brightness, q and u intrinsic to SN 2019ein are very close to zero after correcting for the ISP as discussed in Section 2.4.7. Such small values of Stokes parameters lead to effectively random values of the PA around the SN light-curve peak. Furthermore, we remark that the PA calculated before ISP removal also tends to be consistent from day −11 to +21 (see Table 2.2). A relatively low level of continuum polarization together with a roughly constant direction of the dominant axis suggests a common axial symmetry from the outer electron-scattering zone to the inner region near the energy source.

We remark that RINGO3 uses two dichroics to separate the three wavelength channels and a depolarizing Lyot prism, resulting in an induced systematic uncertainty in polarization of up to $\sim$ 0.5% (Jermak 2017). As shown in the third and the fourth panels of Figure 2.7, after day +5, the continuum level of polarization estimated from RINGO3 observations is mostly from u, while q is consistent with zero. A moderate degree of asphericity is suggested by Kast spectropolarimetry at day +10. Unfortunately, we were not able to conduct Kast spectropolarimetry of SN 2019ein after day +10 owing to technical issues. Therefore, the “rise" in polarization after maximum brightness is anchored by just one RINGO3 measurement from day +21. For this reason, out of an abundance of caution, we refrain from claiming that a definitive rise in polarization was observed in SN 2019ein post maximum brightness. However, if the post-peak rise of polarization is real and intrinsic to SN 2019ein, we cautiously provide our interpretations below, hoping to invite more sophisticated theoretical investigations.

We suggest that the secondary maximum in the NIR band could be the key for understanding the post-peak rise of the continuum polarization. The formation of the secondary maximum in the NIR can be understood as an opacity effect. In normal SNe Ia, although the photospheric radius increases with time because the opacity remains high for $\sim$ 2–3 weeks after the SN explosion, it recedes gradually in mass coordinate (see, e.g., Fig. 3 of Höflich 2017) until the SN light curve approaches its secondary maximum in the NIR. This

may explain the relatively little evolution of polarization seen in SN 2019ein until peak brightness.

After peak brightness, the recession of the SN photosphere is governed by the geometrical dilution of the homologously expanding envelope. However, the photospheric radius decreases rapidly owing to the significant drop in opacity when Fe-group elements begin recombining from ionisation states III to II (Höflich et al. 1993, 1998; Kasen et al. 2006). Therefore, when the SN reaches its secondary NIR maximum $\sim$ 40–50 days after the explosion, most of the energy input emerges above the photosphere. In the presence of an asymmetric energy source, the flux at the photosphere will be direction-dependent, leading to rise in polarization of the SN after maximum brightness. The interpretation of any rise in late-time polarization may be complicated by optical-depth effects that still remain poorly understood (Höflich 1991) in SNe photospheres. As such, detailed theoretical investigations into how polarization behaves over time for various explosion mechanisms are pressingly warranted.

On the other hand, if the rise in late-time polarization is shown to be not true and the inner energy source is found to be spherical, we also arrive at an interesting implication. In that case, models with burning starting on the surface might be better at explaining the observed polarimetry. We speculate that if the burning starts on the surface, the detonation will propagate through the central zone supersonically and preserve the spherical nature of the WD.

Spectropolarimetric observations of SNe Ia beyond 20 days after maximum light are very rare. The handful of SNe Ia for which such measurements exist display low continuum polarization. For example, SN 2012fr was polarized to $\sim$ 0.2% on day +24 (Maund et al. 2013), and SN 2001el and SN 2006X showed $<$ 0.1% polarization on days +38 and +39, respectively (Patat et al. 2009; Wang et al. 2003). These observations challenge the apparent late-time increase in polarization of SN 2019ein. However, owing to a small sample and the fact that these SNe display a diverse set of properties (expansion velocities, decline rates, etc.), the question remains whether any SNe Ia display late-time increases in polarization. More polarimetric observations of SNe Ia at similar phases are required to answer that question.

2.5.1 Implications for Explosion Scenarios

The time-invariant *PA* observed from early times to the phase just prior to the secondary maximum in the NIR light curves of SN 2019ein brings us to the implications for explosion scenarios and the characteristics of p. Based on current understanding, SNe Ia might be triggered through the following mechanisms.

1. Deflagration: compressional heating in a slow accretion near the WD centre triggers subsonic burning when the WD approaches the Chandrasekhar mass $M_{\rm Ch}$ (Nomoto

et al. 1984; Gamezo et al. 2004; Röpke 2007; Ma et al. 2014).

2. Delayed detonation: explosion begins at the end of a deflagration phase near or at the centre of the WD. When a critical density of $\sim 10^7$ g cm^{-3} is reached a transition to detonation occurs (Khokhlov 1991).

3. Colliding/inspiraling WDs: heat released on dynamical timescales triggers a detonation of a double-degenerate system (Iben & Tutukov 1984; Webbink 1984; Benz et al. 1990; Nugent et al. 1997; Pakmor et al. 2010; Kushnir et al. 2013; García-Berro & Lorén-Aguilar 2017).

4. Double/helium detonation: a sub-$M_{\rm Ch}$ C-O WD may explode by detonating a thin surface He layer, which triggers a detonation front in the WD (Woosley et al. 1980; Nomoto 1982b,a; Livne 1990; Woosley & Weaver 1994; Höflich & Khokhlov 1996; Kromer et al. 2010).

In the framework of off-centre delayed-detonation models, a slightly asymmetric excitation will lead to an off-centre distribution of iron-group elements. The axis of symmetry will be defined by the centroid of the density distribution and the point of off-centre delayed-detonation transition (Livne 1999; Höflich et al. 2006; Fesen et al. 2007). If the ^{56}Ni region is above the photosphere, the time-invariant *PA* observed in SN 2019ein would indicate a moderate asphericity of the central energy source. Otherwise, a change of *PA* may be seen as the SN approaches its secondary peak. The low continuum polarization observed in SN 2019ein challenges any model that predicts significant asymmetry of the photosphere.

Dynamical or head-on collisions of WDs are expected to show larger asymmetries (Benz et al. 1990; Pakmor et al. 2011; Sato et al. 2016; Katz et al. 2016; García-Berro et al. 2017; García-Berro & Lorén-Aguilar 2017). The dynamical models are not favoured since they predict high polarization levels at early phases (Pakmor et al. 2012; Bulla et al. 2016a) and larger asymmetries in the inner layers or off-centred energy sources, which are incompatible with our observations of SN 2019ein.

For sub-$M_{\rm Ch}$ explosions through a double/helium detonation, outer asymmetry is expected owing to the He-ignition process. Classical He-detonation models require a significant He-surface mass on the order of 0.01 to 0.1 $M_\odot$ (e.g., Nomoto 1982b,a; Woosley & Weaver 1994; Höflich & Khokhlov 1996; Bildsten et al. 2007; Shen & Bildsten 2009). Starting from the SN explosion, the photosphere recedes and will first cross the burning product of the outermost He layer. The O I λ7774 feature is prominent at day -10.9 in the flux spectrum. However, we see no polarization signal at the corresponding wavelength, suggesting that oxygen was present in the outer layer and maintained a spherically symmetric distribution in the expanding envelope. This is in contrast with the $\sim$ 0.4% O I λ7774 line polarization predicted by Bulla et al. (2016b) for the double/helium detonation

models. Therefore, we infer that the outermost layer is dominated by the spherical pre-explosion C and O from the WD, rather than a He shell, since the latter is likely to produce an abundance jump in O in the line-forming region (see, e.g., Yang et al. 2020). In fact, SNe 2006X and 2004dt, both of which are high-velocity SNe Ia, also show no polarization across O I, putting strong constraints on the distribution of oxygen in the explosion ejecta. We note that the polarimetric properties of more modern models of sub-$M_{\rm Ch}$ double/helium detonation (e.g., Shen et al. 2018) are currently theoretically unexamined.

2.5.2 Comparison with a Detonating Failed Deflagration (DFD) Model

Kasen & Plewa (2007) made theoretical predictions for spectropolarimetric observations of a $M_{\rm Ch}$ WD using the detonating failed deflagration (DFD) model. They studied one particular model in detail, named Y12, in which the WD's ignition starts within a small spherical region, 50 km in diameter and offset 12.5 km from the centre. Here, we compare the observed spectropolarimetric properties of SN 2019ein with the predictions of Kasen & Plewa (2007).

According to Kasen & Plewa (2007), if an SN is observed from the deflagration side – the side where ignition began – high ejecta velocities are expected. Since SN 2019ein exhibited very high expansion velocities, we may be observing the explosion from the ignition side (viewing angles $\theta \approx 0^\circ$). From this orientation, the projected surface of the intrinsically "egg-shaped" density structure in the observer's direction would be fairly circular, leading to low continuum polarization. In fact, Kasen & Plewa (2007) argue that low continuum polarization is expected from all viewing angles at peak brightness. Therefore, continuum polarization is not informative for constraining the viewing angle of the SN.

The Y12 model predicts substantial line polarization (1–2%) depending on the viewing angle (Fig. 13 of Kasen & Plewa 2007). Indeed, we observe significant line polarization across both Si II λ6355 and Ca II NIR3 features in SN 2019ein, which suggests a viewing angle of $\theta \approx 0^\circ$ or 90°. A viewing angle of $\sim 180^\circ$ (opposite to the ignition side) is disfavoured because we observe high polarization across both Si II and Ca II, whereas in the Y12 model only Si II polarization is seen for angles $\sim 180^\circ$. Together with the high expansion velocity of SN 2019ein, $\theta \approx 0^\circ$ is favoured over other orientations, strengthening the case that we may be viewing the SN from the ignition side. According to Kasen & Plewa (2007), such events are rare and expected to constitute roughly 10% of all SNe Ia. Spectropolarimetry of more SNe Ia is needed to test this prediction.

As described in Section 2.4.6, both Si II and Ca II display higher degree of clumpiness at early epochs than near and after peak brightness. This is also expected in the DFD model, which can produce a clumpy outer layer of IMEs but maintain a relatively smoother IME distribution in the inner layers.

2.5.3 The Si II λ6355 Polarization Compared with a Larger Sample

We notice that the continuum polarization of SN 2019ein on the Stokes q–u diagram can be fitted with straight lines (e.g., see the left panels of Fig. 2.6). A dominant axis is present in Kast spectropolarimetry between days ~ -11 and $+10$. Except for the first epoch, the direction of the dominant axis appears to be unchanged, suggesting that different layers of the ejecta share a roughly fixed axial symmetry. These properties indicate that SN 2019ein belongs to the spectropolarimetric type D1 (Wang & Wheeler 2008), in which a dominant axis is identifiable but with significant scatter.

We compared the polarimetric properties of SN 2019ein with those of SNe 2004dt and 2006X, both of which display high expansion velocities at early phases. As inferred from the absorption minimum of the Si II λ6355 line, SN 2004dt shows an expansion velocity of $\sim 17,000\,\mathrm{km\,s^{-1}}$ at $\sim$ 6–8 days before the optical maximum (Wang et al. 2006), and SN 2006X exhibits an expansion velocity of 20,700 $\mathrm{km\,s^{-1}}$ at day -11.3 (Wang et al. 2008). A linear correlation between the maximum polarization measured across Si II λ6355, $p_{\mathrm{SiII}}^{\mathrm{max}}$[5] and the SN expansion velocity traced by the same line at day -5, $v_{\mathrm{SiII@-5d}}$, has been found by Cikota et al. (2019) based on the analysis of a sample of 35 SNe Ia. The velocity-polarization relation connects the kinematics with the ejecta asymmetry and indicates that a higher departure from spherical symmetry for Si is produced at higher velocities.

For comparison with the Si II velocity-polarization relation presented in Figure 13 of Cikota et al. (2019), we estimated $v_{\mathrm{SiII@-5d}} = 15,100 \pm 300\,\mathrm{km\,s^{-1}}$ for SN 2019ein. The peak polarization of SN 2019ein across the Si II λ6355 line, i.e., $p_{\mathrm{SiII}}^{\mathrm{max}}$ derived based on 100 Å and 50 Å binnings on day -4, is $0.76 \pm 0.10\%$ and $0.82 \pm 0.16\%$, respectively. These values place SN 2019ein slightly above the predicted Si II λ6355 polarization. We remark that SN 2019ein is still broadly consistent with the Si II velocity-polarization relation, corroborating the trend that higher-velocity SNe Ia tend to exhibit higher polarization. SN 2019ein shows significantly lower Si II λ6355 polarization compared to SN 2004dt ($14,870 \pm 140\,\mathrm{km\,s^{-1}}$, $1.34 \pm 0.14\%$), which exhibits an exceptionally high peak polarization across the Si II line and was considered an outlier by Cikota et al. (2019). On the other hand, SN 2006X ($17,040 \pm 90\,\mathrm{km\,s^{-1}}$, $0.63 \pm 0.05\%$) is in good agreement with the Si II velocity-polarization relation.

Wang et al. (2007) also derived a correlation between the maximum line polarization of Si II λ6355 and $\Delta m_{15}(B)$. For the former parameter, the observations are often converted to the level at five days before the B-band maximum, i.e., $p_{\mathrm{SiII}}^{\mathrm{corr-5}}$. Owing to the sparsely sampled spectropolarimetry, we adopt the peak Si II λ6355 polarization measured at day -4 for SN 2019ein. The B-band light-curve decline rate of SN 2019ein has been determined as $\Delta m_{15}(B) = 1.36 \pm 0.02$ mag (Kawabata et al. 2020) and $\Delta m_{15}(B) = 1.40 \pm 0.004$ mag

[5]The peak of the Si IIλ6355 polarization is measured between roughly days -11 and $+1$ (Cikota et al. 2019)

(Pellegrino et al. 2020). We infer that SN 2019ein is consistent with the $\Delta m_{15}(B)$–$p_{\rm SiII}^{\rm corr-5}$ relation as presented by Wang et al. (2007) and Cikota et al. (2019). This relation can be interpreted such that at a given epoch, higher line polarization is expected for less-luminous SNe, which indicates a higher chemical nonuniformity. This can be understood as an indication that less material is burned in fainter events, and such incomplete burning may not be sufficient to wipe out lumpy chemical configurations.

Therefore, we conclude that SN 2019ein is consistent with both the Si II velocity–polarization relationship and the light-curve decline rate–Si II polarization relation. Such behaviour may be explained with the off-centre delayed-detonation model (e.g., Höflich et al. 2006; Cikota et al. 2019).

2.6 Concluding Summary

We have presented spectropolarimetry of SN 2019ein, a high-velocity SN Ia in NGC 5353. Our observations range from day −10.9 to +10.1 from the B-band light-curve peak. We found that the continuum polarization in SN 2019ein is low, staying $< 0.25\%$ until about a month after the explosion. This indicates that the photosphere is quite close to being spherical.

The blueshifted emission peaks observed in early-time spectra of SN 2019ein cannot be due to a highly asymmetric explosion, as evidenced by low continuum polarization at early times. However, our observations do not preclude the possibility that optical-depth effects in a steep-density ejecta lead to the apparent blueshift of the emission peaks.

The RINGO3 imaging polarimetry shows an apparent increase in polarization ($\sim 1\%$) around day +21. However, owing to significant systematic uncertainties found in previous RINGO3 measurements, we are cautious of the observed rise in polarization. If the post-peak increase in polarization is real and intrinsic to SN 2019ein, we note that it coincides with the beginning of the transition from Fe III to Fe II ionisation states. The recombination decreases the opacity, providing us a deeper view into the SN ejecta. We speculate that the possible post-peak rise of the polarization, therefore, could indicate the presence of an aspherical central energy source.

The polarization position angle does not change drastically over the observed epochs. We also observe high line polarization ($\sim 1\%$) across the Si II λ6355 and the Ca II NIR3 features around peak brightness of SN 2019ein. The polarization signatures of SN 2019ein are consistent with models predicting SNe Ia explosions that produce a modest amount of asphericity. To summarise,

1. A low amount of asphericity in the high-velocity layers is detected, as in previous observations of other SNe Ia.

2. Significant departures from global spherical symmetry can be ruled out throughout the ejecta. A common symmetry axis persists from the outer to the inner layers.

3. After day +21, the possibility of a small amount of polarization caused by an asymmetric distribution of ^{56}Ni, which may arise from many different models of SN explosions (Höflich 1991; Leonard et al. 2005; Kasen et al. 2009; Pakmor et al. 2010; Seitenzahl et al. 2013; Moll et al. 2014; Raskin et al. 2014; Bulla et al. 2015, 2016a,b; Höflich et al. 2017), cannot be eliminated. Spectropolarimetry of more SNe Ia at post-peak epochs is needed to confirm whether polarization rises beyond day +20.

The spectropolarimetric observations of SN 2019ein strengthen existing evidence that the explosions of SNe Ia are largely spherical, especially when considering that SN 2019ein is an event with one of the highest expansion velocities ever observed.

Finally, we compared the results with the detonating failed deflagration model of Kasen & Plewa (2007) and found that the low continuum polarization but high line polarization are consistent with the model. A viewing angle of $\theta \approx 0^\circ$ is favoured, which means we may be viewing SN 2019ein from the ignition side.

We recommend high-quality spectropolarimetric observations of bright, nearby future SNe Ia to be carried out covering both their rising and falling phases. Such polarimetric tomography is essential for building a robust picture of how polarization signatures vary over time and the consequences of various explosion mechanisms and progenitor scenarios.

Acknowledgements

K.C.P. is thankful to Sergiy Vasylyev and Matthew Chu for helpful discussions. A.V.F.'s group at U.C. Berkeley acknowledges generous support from the Miller Institute for Basic Research in Science, Sunil Nagaraj, Landon Noll, Gary and Cynthia Bengier, Clark and Sharon Winslow, Sanford Robertson, and many additional donors. The UCSC team is supported in part by NASA grants NNG17PX03C, 80NSSC19K1386, and 80NSSC20K0953; NSF grant AST-1815935; the Gordon & Betty Moore Foundation; the Heising-Simons Foundation; and by a fellowship from the David and Lucile Packard Foundation to R.J.F. The research of Y.Y. is supported through the Bengier-Winslow-Robertson Fellowship and the Benoziyo Prize Postdoctoral Fellowship. P.H. acknowledges the support by the NSF project "Signatures of Type Ia Supernovae, New Physics and Cosmology," grant AST-1715133. The supernova research by L.W. is supported by NSF award AST-1817099. J.C.W. is supported by NSF grant AST-1813825. The research of J.M. is supported through a Royal Society University Research Fellowship. M.B. acknowledges support from the Swedish Research Council (Reg. No. 2020-03330).

A major upgrade of the Kast spectrograph on the Shane 3 m telescope at Lick Observatory, led by Brad Holden, was made possible through generous gifts from the Heising-

Simons Foundation, William and Marina Kast, and the University of California Observatories. KAIT and its ongoing operation were made possible by donations from Sun Microsystems, Inc., the Hewlett-Packard Company, AutoScope Corporation, Lick Observatory, the U.S. NSF, the University of California, the Sylvia & Jim Katzman Foundation, and the TABASGO Foundation. Research at Lick Observatory is partially supported by a generous gift from Google. We appreciate the excellent assistance of the staff at Lick Observatory.

PyRAF, PyFITS, STSCI_PYTHON are products of the Space Telescope Science Institute (STScI), which is operated by AURA for NASA. STScI is operated by the Association of Universities for Research in Astronomy, Inc., under NASA contract NAS5-26555. This research has made use of NASA's Astrophysics Data System Bibliographic Services; the SIMBAD database, operated at CDS, Strasbourg, France; and the NASA/IPAC Extragalactic Database (NED) which is operated by the Jet Propulsion Laboratory, California Institute of Technology, under contract with NASA.

Chapter 3

Lick Spectropolarimetry Database of Type Ia Supernovae

3.1 Introduction

In the previous chapter, we presented polarimetric analysis of the Type Ia supernova SN 2019ein. This analysis showed low continuum polarization, suggesting a highly spherical explosion. However, significant polarization in the Si II and Ca II lines indicated a pronounced asphericity in the distribution of intermediate-mass elements. The pattern appears to be consistent across the limited number of SNe Ia that have been studied in detail (see Wang et al. 2008; Yang et al. 2019; Patra et al. 2022b, for examples). Despite their utility as standardizable candles, SNe Ia display considerable diversity. It is crucial, therefore, to investigate how the polarization characteristics of SNe Ia correlate with other properties of these objects. Furthermore, acquiring time-series polarimetry of more SNe Ia is essential for a comprehensive understanding of how their geometrical structures evolve over time.

This chapter presents the largest sample of SN Ia spectropolarimetry to date – the Lick Spectropolarimetry Database of SNe Ia (LSD-Ia). All of these data were obtained with the Kast spectropolarimeter on the Shane 3 m telescope at Lick Observatory. The primary goal of this chapter is to introduce and release this substantial collection of SN Ia polarimetry data. We will outline the features of LSD-Ia, describe its significant aspects, and demonstrate its value through a preliminary analysis of the polarimetry of SN 2011fe. This example highlights the potential of LSD-Ia to enhance our understanding of the structural complexities in SNe Ia, thereby contributing to the broader astrophysical knowledge on SN Ia progenitors and explosion mechanisms.

3.2 The LSD-Ia

The inventory of spectropolarimetric observations is detailed in Table 3.1, which includes the following columns: the name of the supernova, the UTC date of observation, the Modified Julian Date (MJD) of observation, the phase of the SN relative to the date of *B*-band maximum (if known), the internally used night code by the Filippenko group, and references to any papers where the data are published. This comprehensive dataset covers 19 different SNe Ia across 88 total observation epochs. One of the strengths of LSD-Ia is its extensive coverage across various SN phases, ranging from 13 days before to 306 days after peak brightness in the *B* band, capturing the transition into the nebular phase. Additionally, LSD-Ia specifically targets the evolution of polarization through different phases, hence multiple epochs of observations are available for many (but unfortunately not all) SNe.

Table 3.1: Inventory of spectropolarimetry of SNe Ia observed at Lick Observatory.

SN	Obs. Date UTC (MM-DD-YYYY)	Obs. Date (MJD)	Phase[a] (days)	Obs. code (Internal)	References[b]
SN 2011fe	09-02-2011	55806	−7	SB	
SN 2011fe	09-24-2011	55821	8	SC	
SN 2011fe	09-29-2011	55833	20	SD	
SN 2011fe	11-26-2011	55891	78	SF	
SN 2011fe	12-18-2011	55913	100	SG	
SN 2011fe	12-24-2011	55919	106	SI	
SN 2011fe	12-27-2011	55922	109	SJ	
SN 2011fe	01-18-2012	55944	131	SL	
SN 2011fe	02-01-2012	55958	146	SM	
SN 2011fe	02-23-2012	55980	168	SO	
SN 2011fe	04-02-2012	56019	207	SP	
SN 2011fe	04-23-2012	56040	228	SQ	
SN 2011fe	04-28-2012	56045	233	SR	
SN 2011fe	05-21-2012	56068	256	SS	
SN 2011fe	05-29-2012	56076	264	ST	
SN 2011fe	06-18-2012	56096	283	SV	
SN 2011fe	07-11-2012	56119	306	SX	
SN 2014J	01-22-2014	56679	−11	VD	
SN 2014J	03-07-2014	56723	33	VF	
SN 2014J	03-24-2014	56740	50	VG	
SN 2014J	05-27-2014	56804	114	VP	
SN 2014J	06-05-2014	56813	123	VQ	
SN 2014J	06-06-2014	56814	124	VR	
ASASSN-14lp	12-22-2014	57013	−2	WL	
ASASSN-14lp	12-23-2014	57014	−1	WM	
ASASSN-14lp	01-28-2015	57050	35	WN	

Continued on next page

Table 3.1 – continued from previous page

SN	Obs. Date UTC (MM-DD-YYYY)	Obs. Date (MJD)	Phase[a] (days)	Obs. code (Internal)	References[b]
ASASSN-14lp	02-14-2015	57067	52	WO	
ASASSN-14lp	02-25-2015	57078	63	WR	
ASASSN-14lp	03-17-2015	57098	83	WS	
ASASSN-14lp	03-26-2015	57107	92	WU	
ASASSN-14lp	04-16-2015	57128	113	WV	
ASASSN-14lp	04-18-2015	57130	115	WW	
ASASSN-14lp	04-27-2015	57139	124	WX	
SN 2016coj	05-30-2016	57538	−9	YP	Zheng et al. (2017)
SN 2016coj	06-08-2016	57547	0	YQ	Zheng et al. (2017)
SN 2017erp	06-21-2017	57925	−10	AAA	
SN 2017erp	06-27-2017	57931	−4	AAB	
SN 2017erp	07-01-2017	57935	0	AAC	
SN 2017erp	07-18-2017	57952	17	AAE	
SN 2017erp	07-30-2017	57964	29	AAG	
SN 2017fgc	08-01-2017	57966	7	AAH	
SN 2019ein	05-04-2019	58607	−11	ADD	Patra et al. (2022b)
SN 2019ein	05-05-2019	58608	−10	ADD-M	Patra et al. (2022b)
SN 2019ein	05-11-2019	58614	−4	ADF	Patra et al. (2022b)
SN 2019ein	05-12-2019	58615	−3	ADG	Patra et al. (2022b)
SN 2019ein	05-25-2019	58628	10	ADH	Patra et al. (2022b)
SN 2019fck	06-06-2019	58640	–	ADJ	
SN 2019np	01-27-2019	58510	0	ACQ	
SN 2019np	03-17-2019	58559	49	ACY	
SN 2019np	03-31-2019	58573	63	ACZ	
SN 2020ue	02-15-2019	58894	–	AEJ	
SN 2020nlb	07-09-2020	59039	−3	AFG	

Continued on next page

Table 3.1 – continued from previous page

SN	Obs. Date UTC (MM-DD-YYYY)	Obs. Date (MJD)	Phase[a] (days)	Obs. code (Internal)	References[b]
SN 2020nlb	07-18-2020	59048	6	AFH	
SN 2020aatc	12-04-2020	59187	–	AFZ	
SN 2020aatc	12-08-2020	59191	–	AGA	
SN 2020aatc	12-12-2020	59195	–	AGB	
SN 2020aatc	12-19-2020	59202	–	AGC	
SN 2021J	01-17-2021	59231	−2	AGF	
SN 2021J	01-20-2021	59234	1	AGG	
SN 2021J	02-07-2021	59252	19	AGH	
SN 2021J	02-17-2021	59262	29	AGJ	
SN 2021J	03-06-2021	59279	46	AGK	
SN 2021hiz	04-04-2021	59308	−12	AGN	
SN 2021hiz	04-13-2021	59317	−3	AGO	
SN 2021hiz	04-17-2021	59321	1	AGP	
SN 2021hiz	05-03-2021	59337	17	AGQ	
SN 2021hiz	05-08-2021	59342	22	AGR	
SN 2021hiz	05-17-2021	59351	31	AGT	
SN 2021hiz	06-04-2021	59369	49	AGU	
SN 2021qvv	07-02-2021	59397	2	AGY	
SN 2021rhu	07-02-2021	59397	−13	AGY	
SN 2021rhu	07-09-2021	59404	−6	AGZ	
SN 2021rhu	10-07-2021	59494	84	AHJ	
SN 2021rhu	10-15-2021	59502	92	AHK	
SN 2022fw	01-27-2022	59606	–	AHU	
SN 2022fw	02-08-2022	59618	–	AHX	
SN 2022fw	03-08-2022	59646	–	AIA	
SN 2022fw	04-01-2022	59670	–	AID	

Continued on next page

Table 3.1 – continued from previous page

SN	Obs. Date UTC (MM-DD-YYYY)	Obs. Date (MJD)	Phase[a] (days)	Obs. code (Internal)	References[b]
SN 2022hrs	04-25-2022	59694	–	AIG	
SN 2022hrs	04-28-2022	59697	–	AIH	
SN 2022hrs	05-01-2022	59700	–	AII	
SN 2022hrs	05-06-2022	59705	–	AIJ	
SN 2022hrs	05-23-2022	59722	–	AIL	
SN 2022hrs	06-03-2022	59733	–	AIP	
SN 2022hrs	06-25-2022	59755	–	AIR	
SN 2022hrs	06-30-2022	59760	–	AIS	
SN 2022hrs	07-21-2022	59781	–	AIU	
SN 2022ihz	05-01-2022	59700	–	AII	

[a]Relative to peak brightness in *B*-band
[b]Published spectropolarimetry

An excerpt from LSD-Ia is provided in Table 3.2. Owing to the large size of the database, with well over 10^5 entries, it is impractical to display it in its entirety within this thesis. However, the complete, machine-readable database is accessible online at https://kcpatra45.github.io/data/. LSD-Ia includes every Stokes q and u spectrum observed with the Kast spectropolarimeter, presented with wavelengths in Å and Stokes q and u values along with their uncertainties as fractions. To convert these to percentage units, a user needs only to multiply by a factor of 100. It is important to note that only Stokes q and u values are provided; polarization p and position angle PA are not included because they must be recalculated by the user to suit their specific wavelength binning. This is necessary because p and PA do not follow Gaussian statistics and thus cannot be straightforwardly binned; one must first calculate the mean Stokes q and u for a given bin and then compute p and PA. The observation date is recorded in MJD, and the SN phase is noted in days relative to the maximum B-band brightness. The flux density, resulting from the sum of all ordinary and extraordinary spectra involved in calculating Stokes q and u, is presented in units of 10^{-15} erg s^{-1} cm^{-2} Å^{-1}.

Table 3.2: A portion of the Lick Spectropolarimetry Database for SNe Ia.

SN	Wavelength	Flux Density 10^{-15}	q	$q_{\rm err}$	u	$u_{\rm err}$	Date Obs.	Phase[a]
	(Å)	(erg s^{-1} cm^{-2} Å^{-1})	(fraction)	(fraction)	(fraction)	(fraction)	(MJD)	(days)
SN 2011fe	4600.0	439.115845	0.000607	0.001696	0.001666	0.001723	55806	-7
SN 2011fe	4602.0	438.421448	0.001584	0.001694	0.001181	0.001718	55806	-7
SN 2011fe	4604.0	437.372082	0.000787	0.001708	0.001519	0.001735	55806	-7
SN 2011fe	4606.0	435.601185	-0.000443	0.001715	0.001814	0.001747	55806	-7
SN 2011fe	4608.0	433.066856	0.000854	0.001702	0.000693	0.001751	55806	-7
SN 2011fe	4610.0	430.084709	0.001900	0.001676	0.000118	0.001750	55806	-7
SN 2011fe	4612.0	427.144302	0.000291	0.001667	0.000609	0.001746	55806	-7

[a]Relative to *B*-band peak brightness

3.3 Using the Lick spectropolarimetry database: The example of SN 2011fe

SN 2011fe, also known as PTF11kly, is arguably the most extensively studied SN Ia to date. It was discovered on August 24, 2011, by the Palomar Transient Factory (PTF) in the nearby galaxy M101, located approximately 7 Mpc away (Nugent et al. 2011). The LSD-Ia provides extensive spectropolarimetry of SN 2011fe, with over 15 different epochs of observation ranging from a week before peak brightness to several hundred days into the nebular phase. This section presents a preliminary analysis of the polarimetry of SN 2011fe, demonstrating the utility of LSD-Ia.

Figure 3.1 presents the polarization spectra, and Figure 3.2 shows the polarization in the Stokes $q-u$ plane for SN 2011fe, 9 days before the B-band peak. At this early stage, the SN exhibits slight polarization in the continuum at approximately 0.4%. Notably, depolarization occurs blueward of 5500 Å, primarily due to line blanketing by Fe-group elements. At this time, the Si II and Ca II lines also exhibit some minor polarization. The Stokes $q-u$ plane suggests a definite dominant axis, implying axial symmetry in the mild asphericity of the explosion. Ca II shares this axial symmetry with the overall explosion, while Si II displays more complex behavior, appearing to have two components: one that shares axial symmetry with the overall explosion and another nearly perpendicular to it.

However, 12 days after the explosion, as the SN photosphere recedes inward, the ejecta geometry changes, as illustrated in Figures 3.3 and 3.4. The polarization now resembles that of other SNe Ia, such as SN 2019ein or SN 2018gv (Patra et al. 2022b; Yang et al. 2019). The continuum polarization is low, and the Si II and Ca II line polarization seems to be diminishing. Now, the axial symmetry of Si II begins to align with the overall explosion. Thus we see that lower velocity Si follows the global geometry of the rest of the ejecta, but the higher velocity Si may be in clumps or other structures that deviates from that axis of symmetry. This may provide crucial insights into how explosive burning propagates within the exploding white dwarf.

Figure 3.5 shows the time series of continuum polarization for SN 2011fe, with continuum wavelengths chosen in the range 6700–7300 Å. The top panel shows Stokes q and u, the middle panel displays the debiased polarization, and the bottom panel illustrates the polarization position angle. This time series reveals that the outermost layer of SN 2011fe is somewhat aspherical, indicated by the moderate polarization of $\sim$ 0.4%. The middle phases exhibit very low polarization (0.1%), but then the polarization seems to increase again after about 200 days. Further investigation is required to understand this late-time increase in polarization, which may potentially be due to light echoes as the SN light is reflected off dust at light-year distances from the exploding star. The presence of nebular lines, however, may complicate the accurate determination of continuum polarization in the later phases of the SN.

An additional intriguing feature in the polarization of SN 2011fe is the existence of polarization in the Ca II near-infrared triplet around 70 days after the *B*-band maximum, as shown in Figure 3.6. Such late-time Ca II polarization has also been reported in SN 2021rhu (Yang et al. 2022). It is curious that polarization of Ca II lines persists so late in the SN phase when the electron-scattering optical depth is low. Yang et al. (2022) suggest that this polarization may be due to the alignment of calcium atoms in a weak magnetic field through optical excitation by anisotropic radiation from the SN. Now that SN 2011fe also exhibits this effect, and possibly other SNe within the LSD-Ia too, late-time polarimetry of SNe could be an interesting probe for magnetic fields within these events. Alternatively, late-time Ca II polarization could suggest the presence of a deeper layer of asymmetric nucleosynthesis of calcium. This observation would provide new and interesting constraints on the explosion models for Type Ia supernovae.

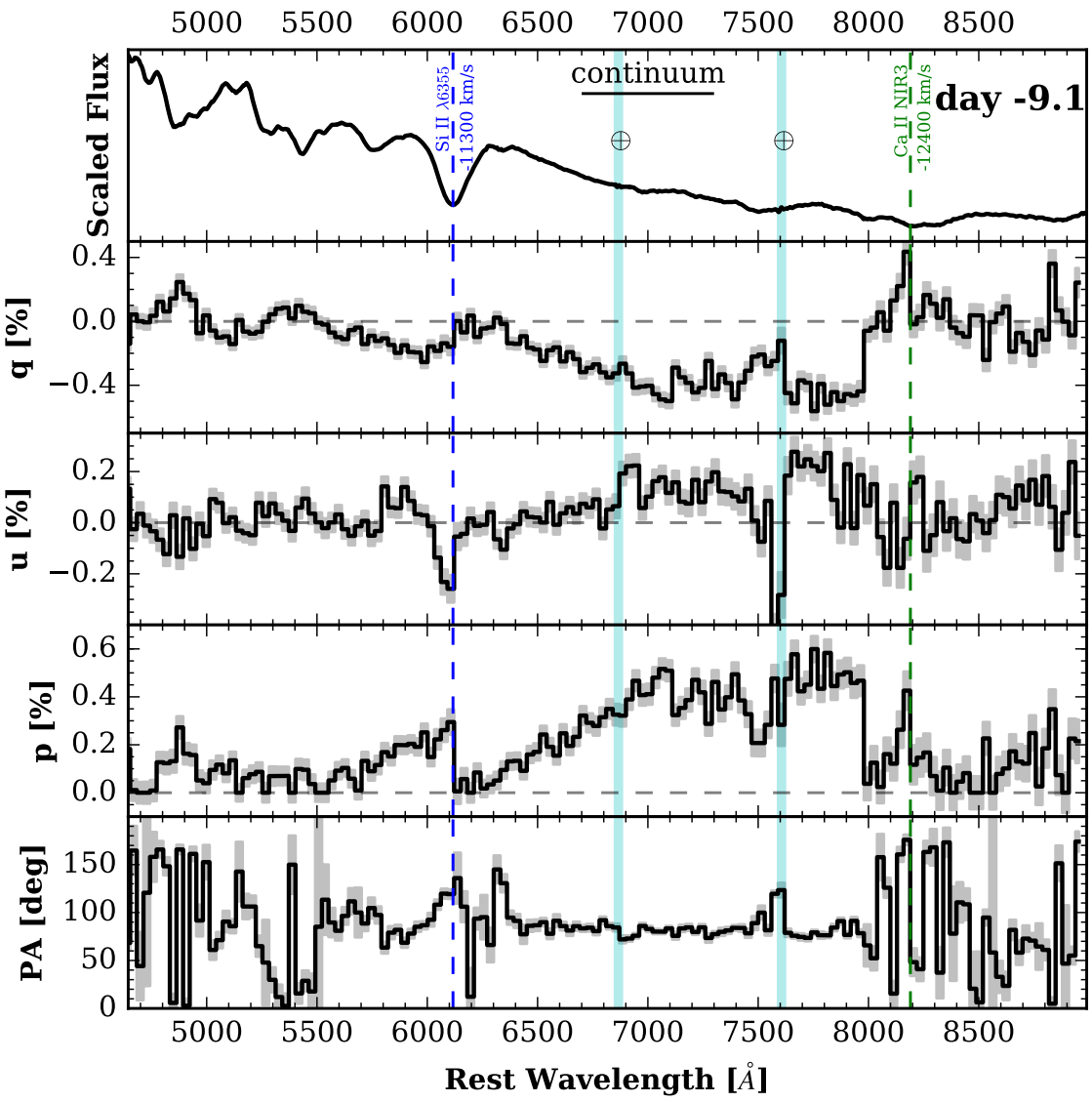

Figure 3.1: Spectropolarimetry of SN 2011fe on day −9.

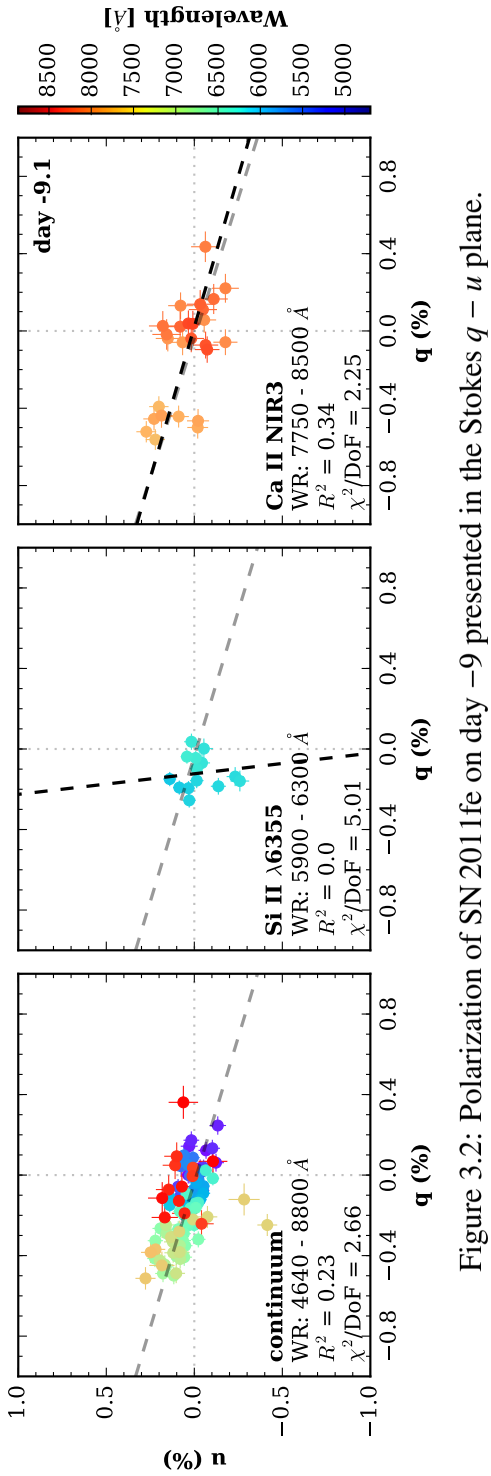

Figure 3.2: Polarization of SN 2011fe on day −9 presented in the Stokes $q - u$ plane.

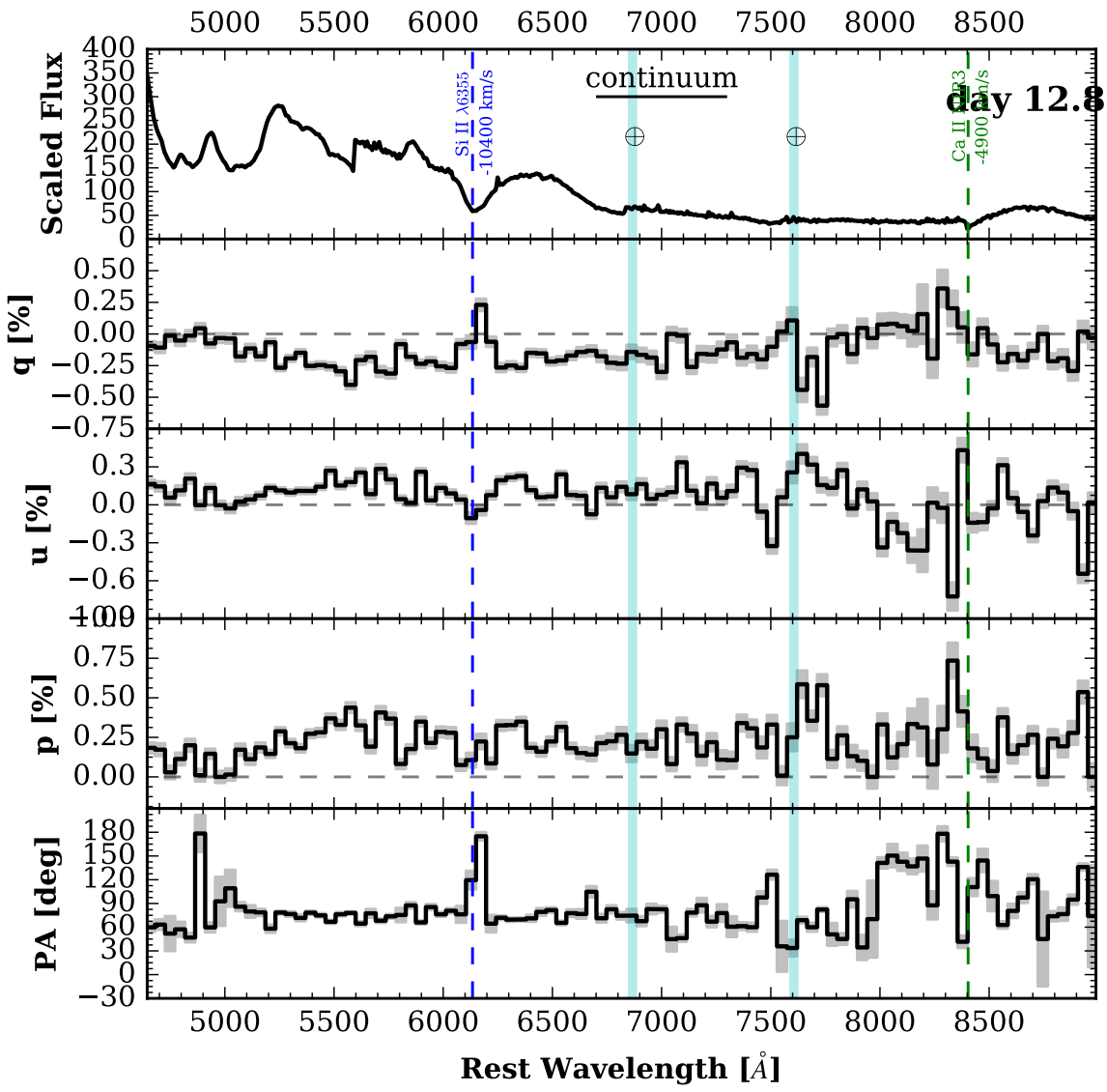

Figure 3.3: Spectropolarimetry of SN 2011fe on day +13.

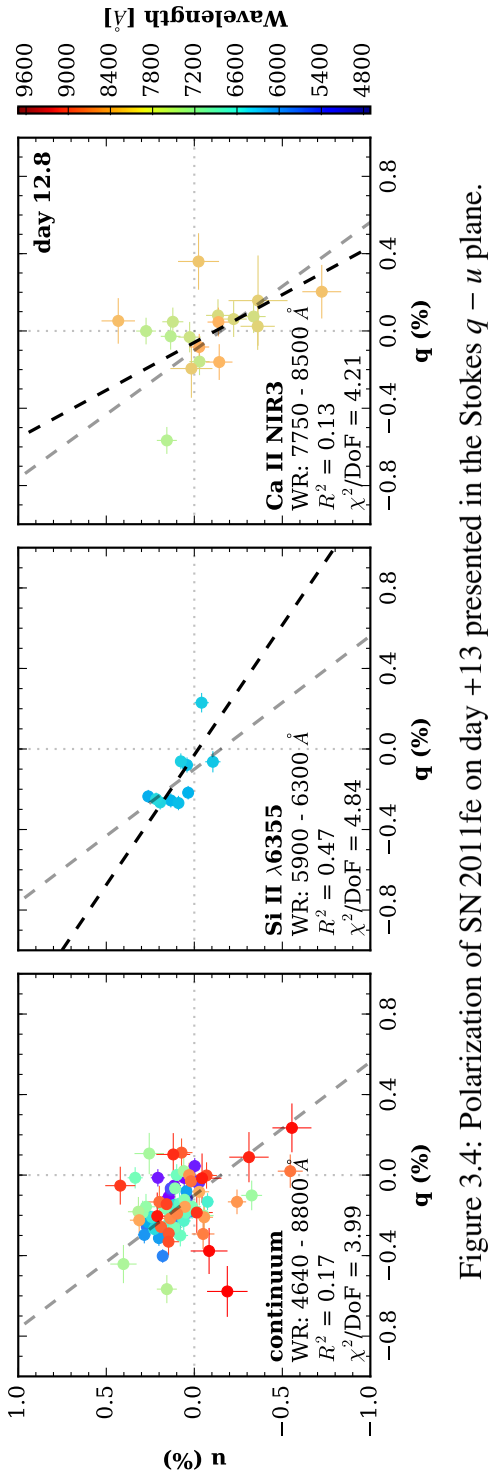

Figure 3.4: Polarization of SN 2011fe on day +13 presented in the Stokes $q - u$ plane.

3.4 Future Work

The comprehensive analysis of the LSD-Ia will require a significant investment of time and is likely to yield multiple publications. However, there are some immediate enhancements necessary for the LSD-Ia. It is essential to incorporate the Galactic extinction values for each SN. This addition will enable the estimation of interstellar polarization (ISP) along the line of sight. While these data will not determine the ISP within the host galaxy of each SN, removing the contribution of Galactic ISP can aid in extracting insights about the dust properties within the host galaxies of the SNe.

Furthermore, with a large sample of SNe, it will be useful to investigate how polarization correlates with other properties of SNe Ia. These properties include, but are not limited to, ejecta velocity, peak absolute magnitudes, Hubble residual, and decline rate (Δm_{15}; Phillips 1993). Incorporating this information into the LSD-Ia will allow for a more careful analysis, which could refine the accuracy of SN distance measurements, thereby enhancing the cosmological utility of SNe Ia.

Another key question that may be answered by further careful examination of LSD-Ia is the potential rotation of the dominant axes of Si II and Ca II lines in the Stokes $q - u$ plane. Preliminary observations of SN 2011fe and SN 2019ein suggest this phenomenon, but conclusive evidence will require data from a broader array of SNe. Fortunately, many SNe in the LSD-Ia database have sufficient early-time coverage to facilitate such work.

On the theoretical front, explanations are needed for the persistence of Ca II line polarization observed at late times. To date, theoretical work in SN polarimetry has not kept pace with observational advances. Better modeling of SN ejecta and polarization predictions, stemming from various SN Ia progenitor models and explosion mechanisms, is essential. Such efforts are crucial for placing stronger constraints on these models.

3.5 Acknowledgments

Over the years, several individuals have contributed to the observations and data reduction with the Kast spectropolarimeter. These include Kelsey Clubb, Melissa Graham, Isaac Shivvers, Heechan Yuk, Patrick Kelly, Jon Mauerhan, WeiKang Zheng, Tom Brink, Sergiy Vasylyev, and Matt Chu.

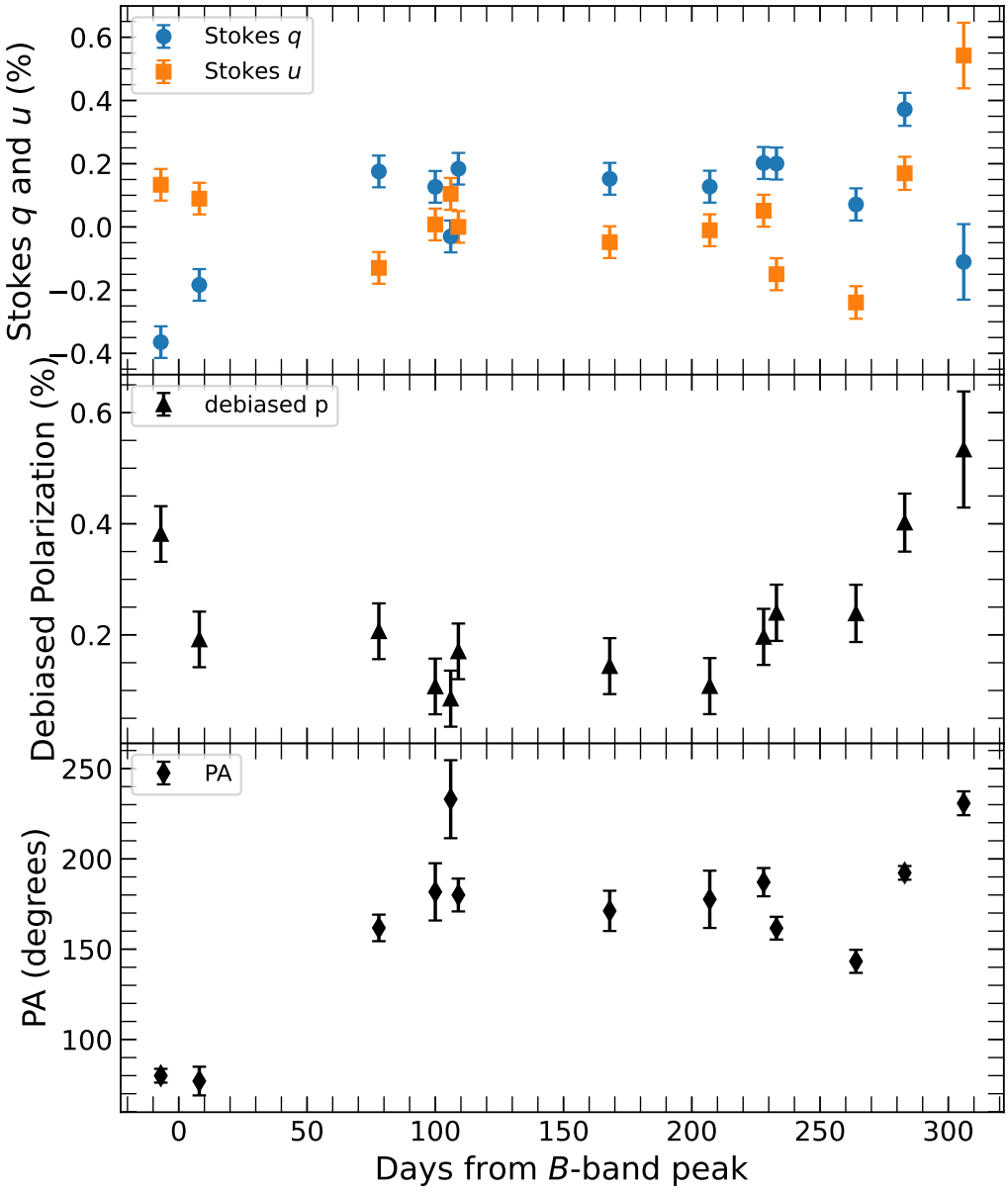

Figure 3.5: The polarization time series of SN 2011fe.

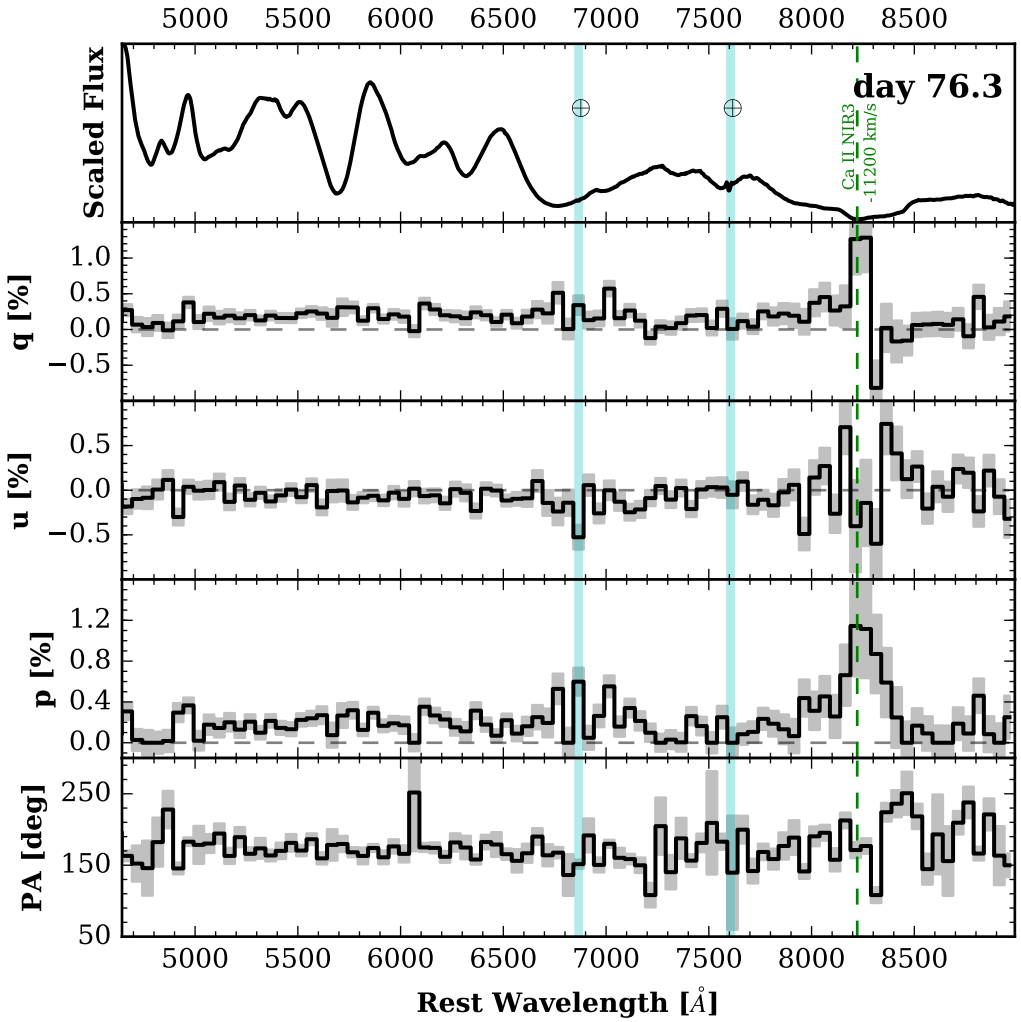

Figure 3.6: Polarization of SN 2011fe on day +76. Note the significant polarization in the Ca II line near-infrared triplet lines.

Chapter 4

Spectropolarimetry of the Tidal Disruption Event AT 2019qiz: A Quasispherical Reprocessing Layer

An earlier version of this article was previously published as Patra, Kishore C.; Lu, Wenbin; Brink, Thomas G.; Yang, Yi; Filippenko, Alexei V.; Vasylyev, Sergiy S. MNRAS, 515, 138.

4.1 Chapter Abstract

We present optical spectropolarimetry of the tidal disruption event (TDE) AT 2019qiz on days +0 and +29 relative to maximum brightness. Continuum polarization, which informs the shape of the electron-scattering surface, was found to be consistent with 0 per cent at peak brightness. On day +29, the continuum polarization rose to $\sim$ 1 per cent, making this the first reported spectropolarimetric evolution of a TDE. These findings are incompatible with a naked eccentric disc that lacks significant mass outflow. Instead, the spectropolarimetry paints a picture wherein, at maximum brightness, high-frequency emission from the accretion disc is reprocessed into the optical band by a nearly spherical, optically thick, electron-scattering photosphere located far away from the black hole. We estimate the radius of the scattering photosphere to be $\sim$ 100 au at maximum brightness — significantly larger than the tidal radius ($\sim$ 1 au) and the thermalisation radius ($\sim$ 30 au) where the optical continuum is formed. A month later, as the fallback rate drops and the scattering photosphere recedes, the continuum polarization increases, revealing a moderately aspherical interior. We also see evidence for smaller-scale density variations in the scattering photosphere, inferred from the scatter of the data in the Stokes q–u plane. On day +29, the Hα emission-line peak is depolarized to $\sim$ 0.3 per cent (compared to $\sim$ 1 per cent

continuum polarization), and displays a gradual rise toward the line's redder wavelengths. This observation indicates the Hα line formed near the electron-scattering radius.

4.2 Introduction

Occasionally a star gets too close to a supermassive black hole (SMBH), at which point tidal forces on the star exceed its self gravity, tearing apart the ill-fated interloper. Tidal disruption events (TDEs) — as these transient events are called — occur when a star wanders within the tidal radius, $r_t \approx R_\star(M_{BH}/M_\star)^{1/3}$, of the SMBH (Hills 1975). Owing to the large spread in specific orbital energy acquired by the post-disruption stellar debris, roughly half of the debris is bound in a range of highly-eccentric orbits around the SMBH, whereas the rest goes unbound (Rees 1988). The bound material is expected to fall toward the SMBH, forming an accretion disk. The gravitational potential energy lost by the infalling matter is converted into electromagnetic radiation, resulting in a luminous flare that enables the detection of TDEs.

All TDEs were originally expected to be extreme-ultraviolet (UV) and X-ray emitters, as is the case for active galactic nuclei. However, many of them were found to show bright near-UV/optical emission with a luminosity much higher than (or at least comparable to) that in the X-ray band (Gezari et al. 2008, 2012; Holoien et al. 2016a; Auchettl et al. 2018; Hinkle et al. 2021; vanVanvan Velzen et al. 2021), igniting a long-standing controversy on the origin of the bright optical emission and on the apparent absence of X-rays in these TDEs[1]. Two classes of solutions have been proposed: (i) the accretion disc does produce ample X-ray emission, but it gets reprocessed by an optically-thick gas layer located at a distance much larger than the tidal radius (e.g., Strubbe & Quataert 2009; Guillochon et al. 2014; Roth et al. 2016; Metzger & Stone 2016; Dai et al. 2018; Lu & Bonnerot 2020), and (ii) instead of accretion, TDEs are powered by shocks resulting from collision of streams in the outer regions of a highly-eccentric disc (e.g., Piran et al. 2015; Shiokawa et al. 2015).

Indirect evidence is beginning to mount in favor of solution (i) in the form that accretion discs are created promptly even in X-ray-lacking TDEs, with double-peaked Balmer lines (Hung et al. 2020; Short et al. 2020) and Bowen fluorescence from excitation by high-energy photons (Leloudas et al. 2019; Blagorodnova et al. 2019) being a few examples. Currently, the details of how such a reprocessing gas layer comes into existence remain unclear. Proposed models include wind or outflows from the TDE (Lodato & Rossi 2011; Miller 2015; Jiang et al. 2016; Dai et al. 2018; Bonnerot et al. 2021) or the presence of a

[1]In this paper, we focus on TDEs that are selected by UV/optical transient surveys, as they are more accessible to optical spectroscopy. Another class of TDEs selected by X-ray transient surveys indeed emit the majority of their luminosity in the extreme-UV and soft X-ray bands with subdominant optical emission, and their rate is likely comparable to the optically-selected ones (Komossa & Bade 1999; Esquej et al. 2008; Sazonov et al. 2021).

radiation-pressure-supported envelope originating from the bound debris (Loeb & Ulmer 1997; Coughlin & Begelman 2014).

A unique and previously unseen perspective on this debate is offered by spectropolarimetry — a technique that measures polarization [2] as a function of wavelength. Light from a TDE is polarized by electron (Thomson) scattering of photons, and the final scatter before escape determines the photon's polarization state. For a spatially unresolved source, such as a TDE, the total polarization will be the integration of the photons' electric vectors projected on the plane of the sky. If the sky-plane-projected photosphere is circularly symmetric, the electric vectors cancel out, resulting in zero polarization. Conversely, if the projected photosphere deviates from circular symmetry, the electric vectors undergo incomplete cancellation, resulting in a net nonzero polarization (see Wang & Wheeler 2008 for a review). In the absence of intrinsically polarized emission from a non-thermal source (e.g., a relativistic jet), the measurement of polarization (or the lack thereof) thus informs the geometry of the electron-scattering surface. The subject of this paper is the spectropolarimetric study of the TDE AT 2019qiz and the resulting constraints on its reprocessing layer.

AT 2019qiz [α(J2000) = $04^{\rm hr}46^{\rm m}37.88^{\rm s}$, δ(J2000) = $-10°13'34.90''$] was discovered on 2019-Sep-19 (UT dates are used throughout this paper; Forster 2019) in the centre of the galaxy 2MASXJ04463790-1013349. A spectrum obtained on 2019-Sep-25 by Siebert et al. (2019) showed broad He II and H I Balmer lines superposed on a blue continuum, classifying AT 2019qiz as a TDE. In the scheme of vanVanvan Velzen et al. (2021), AT 2019qiz falls under the TDE-Bowen class. UV/optical photometry and spectroscopy of AT 2019qiz were analysed by Nicholl et al. (2020) and Hung et al. (2021) independently; we reference their results wherever possible in this paper. The TDE light curve and velocity dispersion of the host galaxy suggests that a $\sim 1\ M_\odot$ star was disrupted by a central black hole of mass $\sim 10^6\ M_\odot$. The peak luminosity ($\sim 10^{43}$ erg s^{-1}) and the total integrated emitted energy ($\sim 10^{50}$ erg) are relatively low compared to other TDEs (Nicholl et al. 2020), which may be due to partial disruption of the star. The X-ray luminosity from this TDE was found to be 2-3 orders of magnitude lower than in the UV/optical, making it a "normal" optically-selected non-relativistic TDE (Nicholl et al. 2020). The host of AT 2019qiz is a face-on barred spiral galaxy (Hubble type SBb). A redshift of $z = 0.01513$ taken from the NASA Extragalactic Database was adopted in this study. The calculated luminosity distance of 65.6 Mpc (assuming a flat ΛCDM cosmological model with $H_0 = 70\,{\rm km\,s^{-1}\,Mpc^{-1}}$ and $\Omega_\Lambda = 0.7$) makes AT 2019qiz the nearest TDE discovered to date.

The Kast spectropolarimeter on the Shane 3 m telescope at Lick Observatory (Miller

[2] In this paper the word "polarization" refers to linear polarization only. We expect that photons emerging from the electron-scattering photosphere have no circular polarization. This is because thermal photons have random phases before they are scattered by electrons, and the scattering process itself does not generate circular polarization.

et al. 1988) has a magnitude limit of approximately 16.5 mag. Most TDEs, therefore, are not bright enough for a meaningful spectropolarimetric measurement by this instrument. Fortuitously, AT 2019qiz was close enough and luminous enough to reach a peak apparent brightness of $\sim$ 16 mag in the Zwicky Transient Facility (ZTF) *r* band (Nicholl et al. 2020), offering a ripe opportunity for the first spectropolarimetric follow-up observations of a TDE with the Kast spectropolarimeter. In this work, we present two epochs of spectropolarimetry of AT 2019qiz separated by a month. We describe our observations in Section 4.3 and present our results in Section 4.4. Interpretation of the data is discussed in Section 4.5 followed by a concluding summary in Section 6.7.

4.3 Observations

Observations and data reduction were carried out following the procedure laid out by Patra et al. (2022b). Below we highlight the important details.

Two epochs of spectropolarimetry of AT 2019qiz were obtained on 2019-Oct-08 and 2019-Nov-06 using the polarimetry mode of the Kast Double Spectrograph. On each night, exposures of 1050 s each were carried out at retarder-plate angles of $0^\circ, 45^\circ, 22.5^\circ$, and 67.5° to calculate the Stokes q and u parameters. All observations were carried out at low airmass ($\lesssim 1.5$), which allowed us to align the slit to a position angle of 180° (north-south direction) on both nights. (Kast lacks an atmospheric dispersion compensator, so it is important to observe at low airmass or align the slit along the parallactic angle; see Filippenko 1982.) We obtained three sets of polarimetry exposures of AT 2019qiz on each night. This allowed us to achieve a higher signal-to-noise ratio (S/N) by median combining the repeated measurements, and to compare the measured Stokes parameters from different exposure sets against each other to check for consistency.

We observed the unpolarized standard star HD 12021 on both nights. The average Stokes q and u were measured to be < 0.05 per cent for HD 12021, thus confirming low instrumental polarization. The same low-polarization standard star was used in the polarizance test, where we determined the polarimetric response of the Kast spectropolarimeter to be > 99.5 per cent over the wavelength range 4600–9000 Å. Additionally, we observed two high-polarization standard stars (HD 25443 and HD 245310) to examine the instrument's accuracy, finding the measured degree of polarization and its position angle consistent with references within 0.1 per cent and 3°, respectively (Schmidt et al. 1992; Wolff et al. 1996).

4.4 The measured polarization

The intensity-normalized Stokes parameters ($q = Q/I$ and $u = U/I$, where where Q and U are the differences in flux with electric field oscillating in two perpendicular directions and I is the total flux) were used to calculate the degree of polarization as

$$p_{\rm obs} = \sqrt{q^2 + u^2}, \tag{4.1}$$

and the polarization position angle (PA) as

$$PA_{\rm obs} = \frac{1}{2} \arctan\left(\frac{u}{q}\right). \tag{4.2}$$

The polarization position angles in this work conform to the International Astronomical Union (IAU) definition in which North = 0° and East = 90°. The quantity $p_{\rm obs}$ is positive definite and thus biased toward higher polarization, especially in the low-S/N regime. Following Wang et al. (1997), we calculated the debiased polarization as

$$p = \left(p_{\rm obs} - \frac{\sigma_p^2}{p_{\rm obs}}\right) \times h(p_{\rm obs} - \sigma_p) \text{ and } PA = PA_{\rm obs}, \tag{4.3}$$

where σ_p denotes the 1σ uncertainty in p and h is the Heaviside step function. We note that this debiasing procedure may overcorrect polarization in certain bins (Montier et al. 2015), however, we determined that using a more robust debiasing technique does not improve the result significantly. See Patra et al. (2022b) for more details behind the calculation of polarization. In Figure 4.1 we show the flux and the polarization spectra measured on days +0 and +29.

One potential complication in the analysis of the polarization of AT 2019qiz is interstellar polarization (ISP). Nonspherical paramagnetic dust grains that are comparable in size to the wavelength of the light will preferentially extinguish photons whose polarization aligns with the long axis of the dust grains. When a large number of such dust grains — along the sight line of the TDE — are aligned similarly under interstellar magnetic fields, they can bias the observed polarization by inducing additional polarization. While it is generally difficult to estimate how much of the measured polarization is due to the interstellar medium, we have reasons to believe that the ISP along the direction of AT 2019qiz is low.

Firstly, Galactic ISP can be estimated to $9 \times E(B-V)$ per cent (Serkowski et al. 1975). Considering the Milky Way colour excess $E(B-V)_{\rm MW} = 0.09$ mag along the line of sight of AT 2019qiz, we get $\rm ISP_{MW} \sim 0.8$ per cent (Schlafly & Finkbeiner 2011). To obtain a better constraint on the Galactic ISP, we measured the polarization of an ISP "probe star"[3], which

[3]Gaia DR2 3184737873690839296

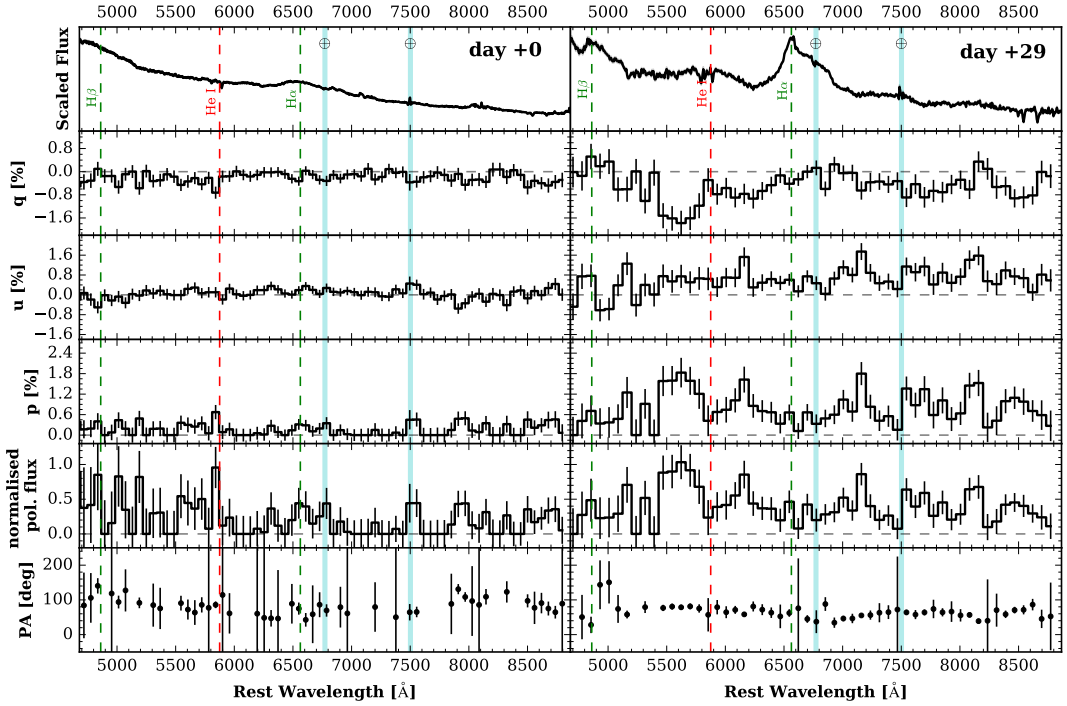

Figure 4.1: Spectropolarimetry of AT 2019qiz on days +0 and +29 relative to the peak brightness on MJD 58764 (Nicholl et al. 2020). Cyan vertical bands mark the spectral regions corrected for major telluric lines. The error bars indicate 1σ uncertainty. With the exception of the flux spectrum, we use 60 Å binning on day +0 and 80 Å binning on day +29 for clarity of presentation. *PA* is undefined when p is 0; we do not show those points in the *PA* panel.

is an intrinsically unpolarized star [4] within 1° of the line of sight of AT 2019qiz, and distant enough to probe at least 150 pc of the ∼ 300 pc scale height of the Galactic interstellar medium. (Beyond ∼ 150 pc, the density drops so rapidly that obtaining spectropolarimetry of a more-distant star does not improve the result much.) The measured Stokes q and u for the probe star were determined to be ∼ 0.1 per cent, thus confirming low contribution from Galactic reddening. Unfortunately, the probe star does not provide any information about reddening from the host galaxy. Instead, from the host-galaxy spectral energy distribution modeling, Nicholl et al. (2020) determined a small additional extinction of $E(B-V)_{\rm host} \approx 0.05$ mag from the host. In combination with the Galactic ISP from the probe star, we constrain the total possible ISP to < 0.5 per cent along the sight line of AT 2019qiz. This upper limit is consistent with the depolarization down to ∼ 0.3 per cent of the Hα and He I emission features. The argument here is that if these emission lines are intrinsically unpolarized, any measured polarization at those wavelengths must be due to ISP. Finally, we see no wavelength-dependent polarization on day +0, indicating that any dust-related polarization is small. Since galactic (Milky Way and host) ISP should remain constant over the lifetime of a TDE, any subsequent increase in polarization at a later time must be intrinsic to the TDE. Thus, all things considered, we deemed the ISP along the line of sight of AT 2019qiz to be low. Justifiably, in the absence of a stronger constraint on the ISP, we did no further ISP correction.

The continuum polarization of AT 2019qiz at the two epochs was estimated based on the Stokes parameters over the wavelength range 7100–8200 Å. Admittedly, the choice of this wavelength range is arbitrary. Nonetheless, our choice was based on the fact that this region (i) is devoid of strong absorption or emission features, (ii) is sufficiently large to average over random statistical fluctuations in q and u, and (iii) avoids the extreme ends of the spectra where the S/N is lower. Stokes q and u were averaged over the aforementioned wavelength range and weighted by the inverse-squared 1σ uncertainties. The degree of the continuum polarization and the associated position angle were then calculated based on the weighted mean Stokes parameters.

At its maximum brightness, the continuum polarization of AT 2019qiz was $p_{\rm d+0} = 0.16 \pm 0.05$ (stat) ± 0.10 (sys) per cent. The systematic uncertainty is an estimation of the limitation of the instrument, which was determined from the polarimetry of bright polarization standard stars. Low polarization on day +0 indicates that the sky-projected electron-scattering surface is almost circularly symmetric. The polarization position angle was $PA = 85° \pm 23$. We note that since PA displays mostly random values in the low-polarization regime, this PA measurement is not particularly meaningful. A month later, on day +29, the continuum polarization increased to $p_{\rm d+29} = 0.93 \pm 0.09$ (stat) ± 0.10 (sys) per cent. A more secure measurement of position angle was made with $PA = 59° \pm 7$. Note that the polarization below 5500 Å is less reliable owing to comparatively poorer S/N than

[4] Spectral type A5-F5

in the rest of the spectrum. On day+29, the peak of the Hα emission line shows depolarization (compared to the continuum) down to $p_{\mathrm{H}\alpha} = 0.3 \pm 0.1$ per cent in the 200 Å around the 6563 Å line.

4.5 Interpretation

In scenarios where optical emission of a TDE is powered by a naked eccentric disc lacking significant mass outflow, a high level of polarization can be expected owing to imperfect cancellation of electric vectors across the sky-projected surface. However, the low continuum polarization observed on day +0 implies that the sky-projected electron-scattering photosphere was close to being circularly symmetric. In three dimensions, it is reasonable to assume that the circular symmetry arises from the projection of a spherical electron-scattering photosphere. The continuum polarization on day +29 is no more than ~ 1 per cent, which translates to only a moderate amount of asphericity (aspect ratio ~ 0.8 for a Thomson scattering optical depth $\tau = 1$ and a radial density profile approximated by a steady mass-loss wind; Höflich 1991). These results are incompatible with models that require a highly eccentric disc as the dominant source of optical emission. Additionally, if a disc with high initial eccentricity circularises over time, it should display high polarization at early phases followed by a gradual decrease later. The observed polarization, however, follows the opposite trend.

One might argue that a circular accretion disc is also consistent with the observed spectropolarimetry. However, such a disc requires the less-likely special condition in which it is almost face-on to the observer at maximum brightness. Weak X-ray emission observed from AT 2019qiz (compared to UV/optical) is in tension with the face-on disc (Nicholl et al. 2020). This is because the emission of X-ray flux is viewing-angle dependent, with low X-ray emission expected from edge-on accretion discs and vice versa (Dai et al. 2018). Furthermore, the increase of polarization on day +29 precludes the face-on-disc scenario, unless the inclination of the disc changes dramatically over a month. The data thus disfavor a naked accretion disc — either eccentric or circular. Instead, a quasispherical reprocessing layer originating from mass outflow is consistent with the observations, and we can place interesting constraints on the said layer.

4.5.1 The size of the reprocessing layer

The radius of the electron-scattering photosphere can be estimated from the mass outflowing rate given by $\dot{M} = 4\pi r^2 \rho v$, where ρ is the density and v is the outflow velocity. The size of the electron-scattering photosphere (r_{s}) is determined by the scattering optical depth $\tau_{\mathrm{s}} = \rho \kappa_{\mathrm{s}} r_{\mathrm{s}} = 1$, where $\kappa_{\mathrm{s}} \approx 0.34\,\mathrm{cm^2\,g^{-1}}$ is the Thomson opacity for solar metallicity. Thus,

we obtain

$$r_{\rm s} = \frac{\dot{M}\kappa_{\rm s}}{4\pi v} \approx 1.7\times10^{15}\,{\rm cm}\,\frac{\dot{M}}{{\rm M}_\odot\,{\rm yr}^{-1}}\,\frac{10^9\,{\rm cm\,s}^{-1}}{v}. \tag{4.4}$$

Although the detailed physical processes driving the outflow are still uncertain, we can infer the outflow velocity $v \approx 10^9\,{\rm cm\,s}^{-1}$ from the observed emission-line widths (e.g., Hung et al. 2020), and we expect the mass-outflow rate to be comparable to the mass-fallback rate. This is because (i) the fallback gas is only marginally bound (compared to the binding energy near the tidal radius), and (ii) the heating rate owing to shocks and viscous accretion is super-Eddington. The peak fallback rate can be estimated as $\dot{M}_{\rm fb,max} \approx M_*/3P_{\rm min} \approx 3\,{\rm M}_\odot\,{\rm yr}^{-1}\,(M_{\rm h}/10^6\,M_\odot)^{-1/2}(M_*/M_\odot)^{1/2}$, where $M_{\rm h}$ is the black hole mass, $P_{\rm min} \approx 41\ {\rm d}\,(M_{\rm h}/10^6\,M_\odot)^{1/2}(M_*/M_\odot)^{1/2}$ is the minimum orbital period of the fallback material, and we have taken the stellar radius to be $R_* \approx R_\odot(M_*/M_\odot)$ for a main-sequence star of mass M_*. The mass of the central black hole of the host galaxy of AT 2019qiz was estimated to be of the order $10^6{\rm M}_\odot$ (Nicholl et al. 2020; Hung et al. 2021). Based on these arguments, we conclude that the scattering photospheric radius of the outflow is of order 100 au near peak brightness (at time $t \approx P_{\rm min}$ since the disruption). At later time $t \gtrsim P_{\rm min}$, the fallback rate drops as $\dot{M}_{\rm fb} \propto t^{-5/3}$, which causes $r_{\rm s}$ to shrink.

Let us now also determine the thermalisation radius ($r_{\rm th}$), where the optical continuum is formed. The last absorption surface is located where the effective optical depth $\sqrt{\tau_{\rm a}\tau_{\rm s}} \approx 1$ (Rybicki & Lightman 1986), where $\tau_{\rm a}$ and $\tau_{\rm s}$ are the absorption and scattering optical depths, respectively.

Assuming a constant-velocity mass outflow with $\rho \propto r^{-2}$, we can write the thermalisation radius as

$$r_{\rm th} \approx \sqrt{\kappa_{\rm a}/\kappa_{\rm s}}\,r_{\rm s}. \tag{4.5}$$

The problem here is that the absorption opacity, $\kappa_{\rm a}$, is generally difficult to estimate from first principles (non-local thermodynamic equilibrium radiative transfer). To make progress, we can use the fact that above $r_{\rm th}$, instead of streaming freely, photons will diffusively advance outward owing to electron scattering. Using the diffusive flux, $F_{\rm diff} \approx U_{\rm rad}c/\tau_{\rm s}(r_{\rm th})$, where $U_{\rm rad}$ is the radiation energy density and $\tau_{\rm s}(r_{\rm th}) = r_{\rm s}/r_{\rm th}$ is the scattering optical depth at $r_{\rm th}$, we can write the bolometric luminosity as $L = 4\pi r_{\rm th}^2 F_{\rm diff}$. Rearranging for the thermalisation radius, and using $U_{\rm rad} = aT^4$, we find

$$r_{\rm th} = \left(\frac{r_{\rm s}L}{4\pi caT^4}\right)^{1/3}, \tag{4.6}$$

where a is the radiation constant and T is the observed color temperature. At the peak brightness of AT 2019qiz, L and T were found to be about $10^{43.7}\,{\rm erg\,s}^{-1}$ and $2\times10^4\,{\rm K}$, respectively (Nicholl et al. 2020; Hung et al. 2021), giving $r_{\rm th} \approx 5.7\times10^{14}\,{\rm cm}\,(\dot{M}_{+0}/{\rm M}_\odot\,{\rm yr}^{-1})^{1/3}(v/10^9\,{\rm cm\,s}^{-1})^{-1/3}$, where $\dot{M}_{+0}$ is the outflow rate on day +0. This shows that the optical continuum forms well below the electron-scattering surface. From

here, using Equation 4.5, we can also estimate the absorption opacity $\kappa_a \approx 0.1\kappa_s$ for our fiducial parameters.

On day +29, the mass-outflow rate has dropped by a factor of a few (depending on P_{min}) from the peak value, and hence the scattering photosphere would shrink significantly by the same factor. At this time, $L \approx 10^{43}\,\mathrm{erg\,s^{-1}}$ and $T \approx 1.5 \times 10^4\,\mathrm{K}$, giving us $r_{th} \approx 3.9 \times 10^{14}\,\mathrm{cm}\,(\dot{M}_{+29}/0.5\,\mathrm{M_\odot\,yr^{-1}})^{1/3}(v/10^9\,\mathrm{cm\,s^{-1}})^{-1/3}$, which is only slightly smaller than the r_{th} at maximum brightness. Thus, over time, the electron-scattering photosphere gets closer to the thermalisation radius, exposing more of the internal asymmetries that manifest as a higher-polarization signal. The recession of the photosphere also harmonises with the independent observation that X-ray emission from TDE 2019qiz, although low initially, rose slowly and reached a peak ~ 25 days after maximum brightness (Nicholl et al. 2020).

The observed rise in the level of polarization to ~ 1 per cent on day +29 can be explained by the presence of an asymmetric interior scattering photosphere, the projection in the sky of which has an aspect ratio $e \approx 0.8$ (Höflich 1991) and is pointed $\sim 120°$ counterclockwise from the north–south axis in the sky. This is a simplified but illustrative interpretation of the polarization signal; the electron-scattering photosphere may have more irregularities compared to an ellipsoid. The inner asphericity could arise from an asymmetric outflow in the inner regions. The implication here is that when the scattering photosphere is much larger than the thermalisation radius (as is the case at maximum brightness), the scattering surface will appear quite spherical even with an asymmetric outflow velocity field underneath. This explains why low polarization is measured near maximum brightness, but as the scattering photosphere recedes, the asymmetry of the inner regions becomes more prominent, consequently increasing the polarization. One notable caveat to this interpretation is that the TDE spectra have some contamination from the stellar light. On day +29, as the TDE becomes fainter, the stellar light comprises a larger fraction of the observed light. Thus, if the stellar light was *somehow* polarized, that could explain the observed rise in polarization on day +29. However, a simple argument rules out this possibility: let us consider an upper limit of 10 per cent contamination from stellar light (the actual contamination level is probably closer to 1 per cent). If the ~ 1 per cent observed polarization were to come from stellar light alone, it requires the stellar light to be polarized at 10 per cent level, which is unlikely. Any smaller amount of contamination requires the stellar light to be polarized at even higher level. Thus it is reasonable to conclude that the rise in polarization on day +29 was not due to contamination by polarized stellar light.

We emphasise that we remain agnostic about the exact mechanism by which the outflow originates, ultimately creating the reprocessing layer. With the data at hand, we can only conclude that any model with strong mass outflow is consistent with the observations. Detailed theoretical modeling and more polarimetric TDE studies will be required to discriminate between the existing models.

4.5.2 Substructures in the electron-scattering photosphere

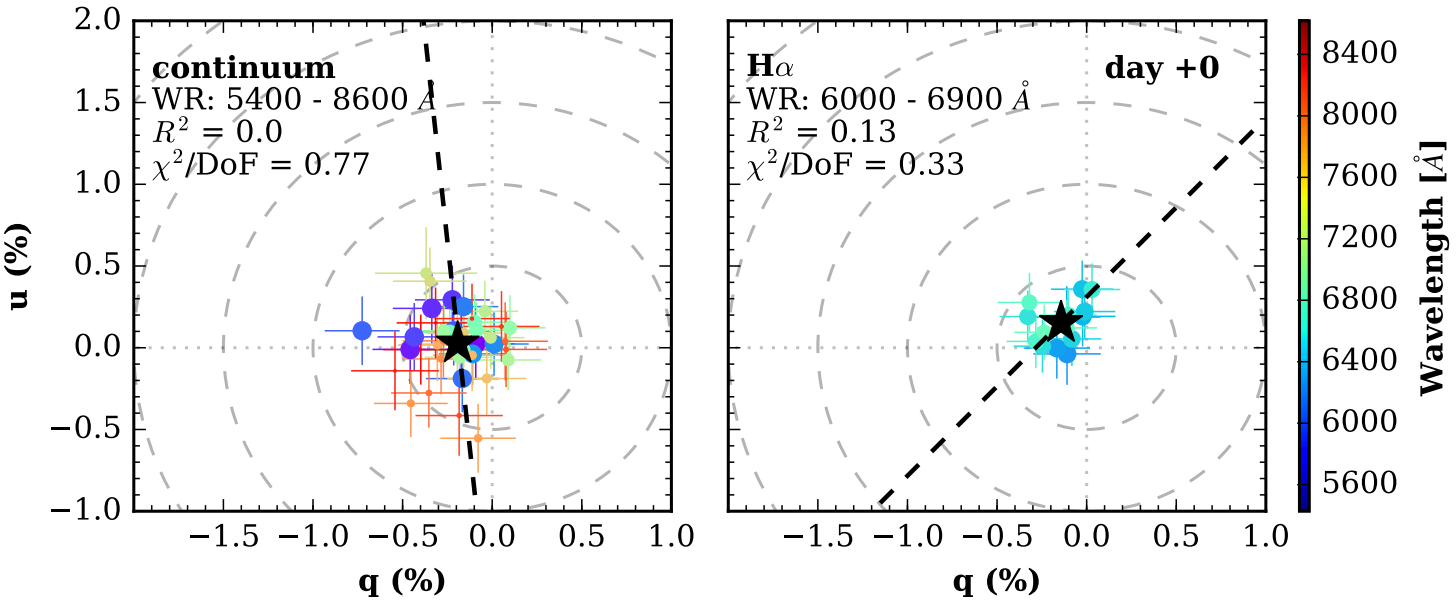

Figure 4.2: Polarization of AT 2019qiz in the $q - u$ plane on day +0. The left-side panel shows the polarization in the wavelength range 5400–8600 Å, coloured by wavelength. Additionally, the size of the data points also reflects their relative wavelengths in a decreasing order (i.e., larger points are bluer). The right-side panel only shows the polarization of the Hα line in the wavelength range 6000–6900 Å. The black dashed lines are the best-fitting dominant axes. Constant-polarization contours in 0.5 per cent increments are shown as dashed circles. The black star in each panel represents the error-weighted mean Stokes q and u. The coefficient of determination (R^2) and the χ^2/DoF are also provided.

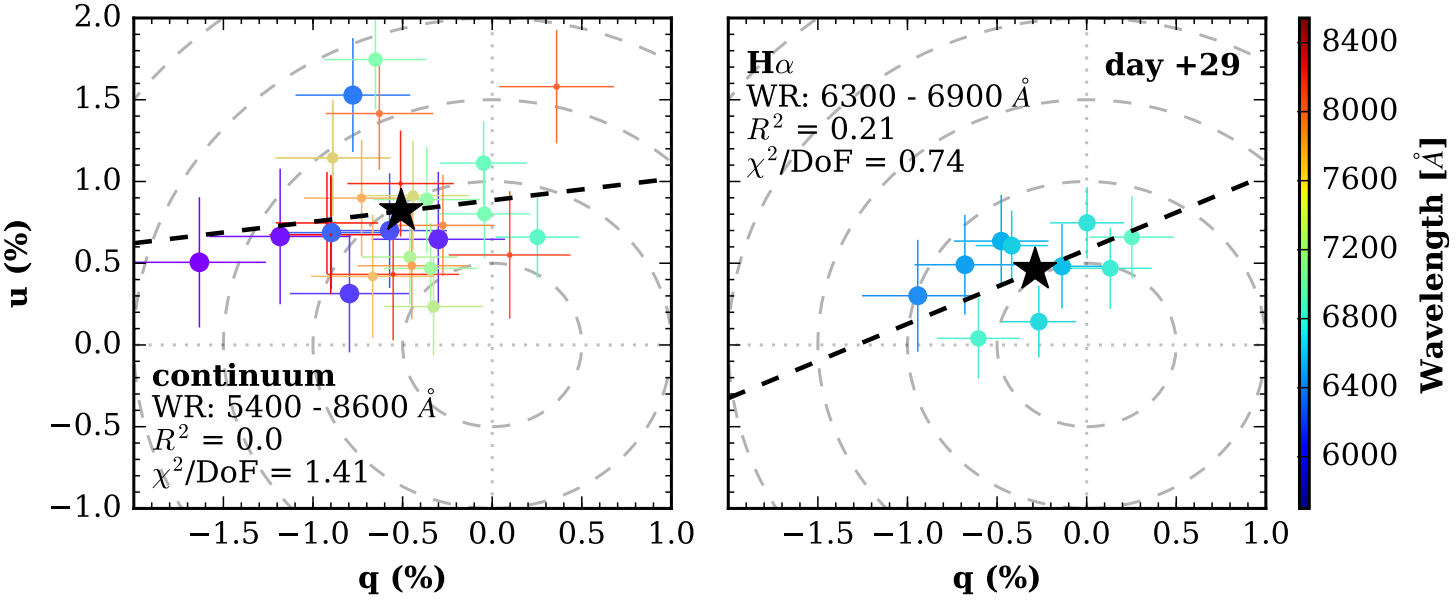

Figure 4.3: Same as Figure 4.2 but for day +29. The Hα wavelength range is 6300–6900 Å. The abscissa and the ordinate are on the same scale as Figure 4.2 for ease of comparison.

Substructures in the photosphere can be probed by plotting the polarization in the Stokes $q - u$ plane. If the photosphere is axially symmetric, the data will lie along a straight line called the "dominant axis" (Wang et al. 2003; Maund et al. 2010). In the $q - u$ plane, distance from the origin represents deviation from circular symmetry, whereas scatter around the dominant axis shows departure from axisymmetry (for e.g., clumps of material). Figures 4.2 and 4.3 show the polarization in the $q - u$ plane on days +0 and +29, respectively. The left panel displays polarization over the wavelength range 5400–8600 Å. Note that we ignore wavelengths below 5400 Å because the S/N on the blue end is poorer compared to the rest of the spectrum. The right-side panel also shows polarization but only for the Hα feature. The dominant axes fitted to the data in each panel are indicated by the dashed black lines. The black star represents the error-weighted mean Stokes q and u. At maximum light the data are distributed around the origin, indicating that the photosphere is highly spherical. On day +29, the data are farther from the origin, showing that an aspherical interior has begun emerging at this epoch. Additionally, as indicated by the increased value of chi-squared per degree of freedom (χ^2/DoF), the scatter of the data relative to the dominant axis is also elevated on day +29 compared to day +0. The implication is that the aspherical photosphere is clumpier on day +29 than at maximum brightness. In the context of a TDE photosphere, the clumpiness of the material may refer to smaller-scale density variations that contribute different amounts of polarized flux. We sketch the implied geometry of the electron-scattering photospheres on days +0 and +29 in Figure 4.4 based on the observed Stokes parameters, PA, and the relation between polarization and asphericity of scattering-dominated atmospheres (Höflich 1991).

4.5.3 Hα line polarization

The Hα emission line is depolarized compared to the continuum on day +29. This observation implies that the Hα line-forming region is close to the electron-scattering surface, $r_{\mathrm{th},\alpha} \approx r_{\mathrm{s}}$. Our reasoning is as follows. If Hα formed near the continuum thermalisation surface, the Hα photons would be similarly polarized to the rest of the continuum as they diffuse through the electron-scattering-dominated region. Instead, if the Hα-forming region is closer to the electron-scattering surface, then the probability that Hα photons will scatter is smaller owing to lower scattering optical depth, thus suppressing the polarization (see Figure 1 of Höflich 1991). Such depolarization is also seen for the He I emission line at 5875 Å. It follows from this argument that the red shoulder of the Hα profile should show a gradual increase in polarization — the redder photons originate closer to the continuum thermalisation radius (as a result of lower line absorption opacity) — until the polarization matches the continuum level at the end of the red shoulder. Hints of this are visible in the Hα polarization profile of AT 2019qiz on day +29, although the S/N is not sufficiently high to make a definitive claim. If this polarization feature is more securely realised in

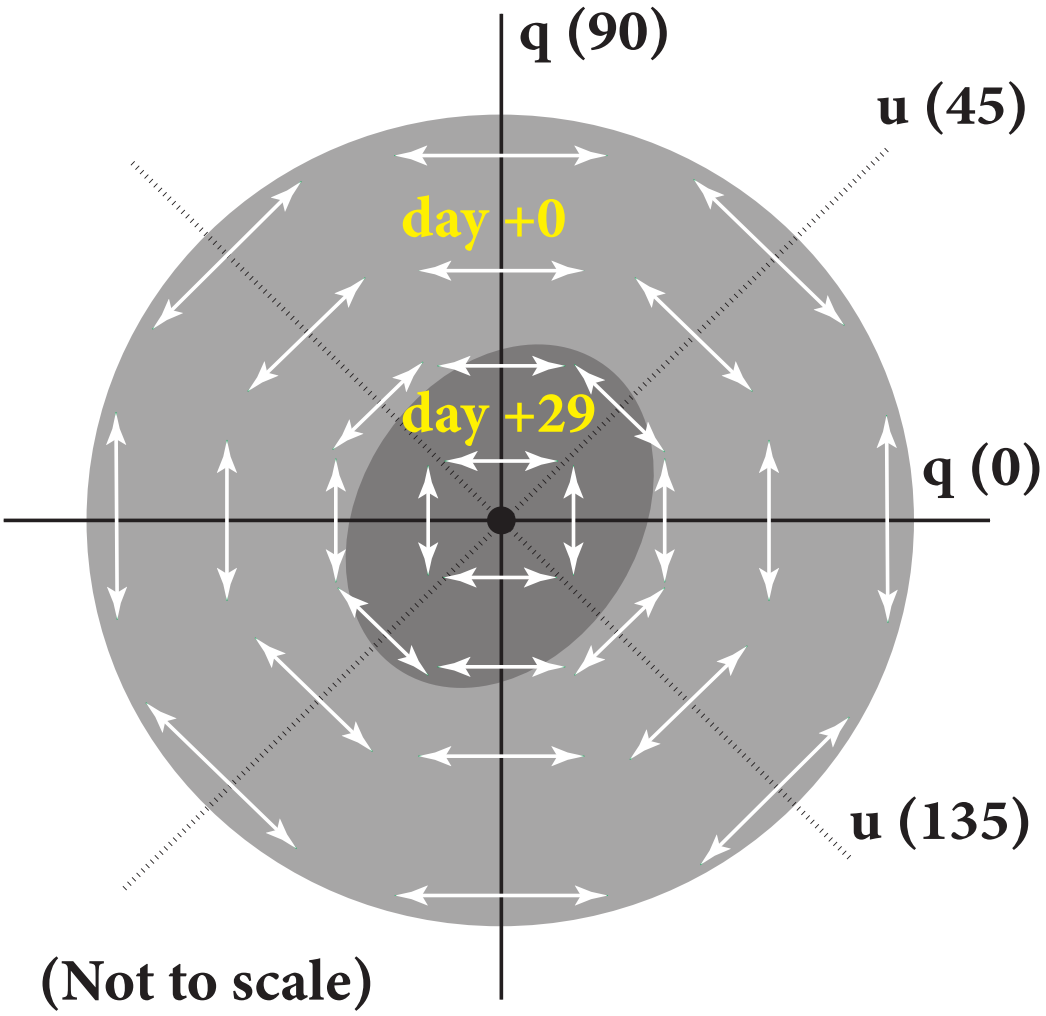

Figure 4.4: Schematic diagram illustrating the geometrical configuration of a sky-projected electron-scattering photosphere that is compatible with the observed polarimetry. The white arrows represent the relative size and direction of the local polarization. The outer circle shows the scattering photosphere on day +0, and the inner ellipse displays the photosphere a month later on day +29. The inner ellipse has an aspect ratio of $e \approx 0.8$, which produces $\sim$ 1 per cent continuum polarization in a scattering-dominated photosphere.

subsequent spectropolarimetric studies of TDEs, it would provide supporting evidence to the claim made by Roth & Kasen (2018) that electron scattering plays a significant role in spectral-line formation in TDEs.

Alternatively, if the Hα line actually forms outside the electron-scattering radius, spectropolarimetry can once again provide evidence. In that case, the Hα emission line would be completely depolarized because flux from emission is intrinsically unpolarized.

4.5.4 Comparison with other polarimetric studies of TDEs

Owing to the low rate of TDEs ($\sim 10^{-6}$–10^{-4} yr^{-1}; Holoien et al. 2016b) per galaxy, only a handful of polarimetric studies of TDEs currently exist. Nonetheless, these studies show a diverse range of TDE polarization. Here we summarise what is currently known about TDEs from polarimetric studies.

The first reported spectropolarimetric measurement of a TDE was carried out by Holoien et al. (2020) for ASASSN-18pg, who found $\sim$ 1.5 per cent continuum polarization on day -10. However, unlike for AT 2019qiz, most of the polarization measured for ASASSN-18pg was attributable to ISP and not the TDE itself. Thus, our work is the first time intrinsic spectropolarimetric evolution of a TDE has been observed.

Deep-infrared imaging polarimetry of the putative[5] TDE *Swift* J164449.3+573451 showed 7.4 ± 3.5 per cent polarization (Wiersema et al. 2012). However, the authors were unsure about how much of the observed polarization was due to host-galaxy ISP in this highly-reddened event. *Swift* J2058+0516, which is comparatively less afflicted with reddening, exhibited polarization of 8.1 ± 2.5 per cent, with weak evidence for evolution over three epochs (Wiersema et al. 2020). Both *Swift* TDEs had relativistic jets in which high polarization may originate from the tail of nonthermal radiation (e.g., synchrotron) at optical/infrared wavelengths (Lee et al. 2020).

Optical imaging polarimetry of OGLE16aaa — an unjetted thermal TDE — showed polarization at the 1.81 ± 0.42 per cent level, but again the contribution of ISP is unknown (Higgins et al. 2019). Another thermal TDE, AT 2019dsg, displayed high polarization of up to $\sim$ 9 per cent in the optical V band, which decreased to $\sim$ 3 per cent a month later (Lee et al. 2020). The authors attributed this high level of polarization to either an anisotropic accretion disc or contribution from relativistic jet emission. It is unclear how a TDE could achieve high polarization ($\sim$ 8–9 per cent) by a purely electron-scattering process; Höflich (1991) showed that linear polarization maxes out at $\sim$ 4.5 per cent in highly-oblate spheroids ($e < 0.2$; see Figure 4 of Höflich 1991). Thus, there is no clear explanation yet for the diversity of TDE polarization. Evidently, more polarimetric (spectroscopic or photometric) studies of TDEs are necessary to unify these observations.

[5]The initial gamma-ray burst and X-ray properties were in conflict with a TDE interpretation, but late-time properties were more like a TDE (Bloom et al. 2011).

4.6 Conclusion

We have presented 2 epochs of spectropolarimetry of the TDE AT 2019qiz, demonstrating the first observed spectropolarimetric evolution of a TDE. The continuum polarization at maximum brightness was found to be consistent with 0 per cent, but increased to $\sim$ 1 per cent a month later. These observations disfavour a naked accretion disc without significant outflow in AT 2019qiz because high polarization is expected from an eccentric disc. Instead, our data favour the existence of a nearly spherical, optically thick, scattering-dominated gas layer. The apparent sphericity of the scattering photosphere explains the low polarization observed at peak brightness. We estimate the radius of the scattering photosphere to be $\sim$ 100 au at maximum brightness, which is much larger than the size of the complex, aspherical hydrodynamic structures of the bound gas.

As the outflow weakens and the photosphere recedes, the underlying aspherical interior begins to emerge, thus explaining the increased polarization on day +29. By plotting the polarization in the Stokes $q - u$ plane, we showed that on day +29 the electron-scattering layer is clumpy, which indicates the presence of smaller-scale density variations in regions contributing to the polarized flux. The depolarization of the Hα emission line shows that the Hα line-forming region is closer to the electron-scattering radius rather than to the continuum thermalisation radius.

This study demonstrates the immense power and potential of spectropolarimetry in delineating the geometry of a TDE, and thus providing a new perspective on the origin of the optical emission of TDEs. Indeed, well-sampled spectropolarimetric observations could help build a "tomographic" picture of a TDE as it evolves. Primary challenges include the rarity of bright and nearby TDEs that will provide sufficiently high S/N to allow a feasible spectropolarimetric study. Additionally, no theoretical models for polarization of a TDE exist at the moment. Such models may enable stronger constraints on the TDE geometry as opposed to order-of-magnitude estimates. We hope that this work serves as a clarion call for further spectropolarimetric studies of TDEs.

Acknowledgements

K.C.P. thanks Nina Pak for her help in creating Figure 4.4, and Andrea Antoni for helpful discussions. We thank Ryan Foley for recommending that we collect spectropolarimetric observations of AT 2019qiz. A.V.F.'s group acknowledges generous support from the Christopher R. Redlich Fund, the U.C. Berkeley Miller Institute for Basic Research in Science, Sunil Nagaraj, Landon Noll, Sandy Otellini, and many additional donors. W.L. was supported by the Lyman Spitzer, Jr. Fellowship at Princeton University. A major upgrade of the Kast spectrograph on the Shane 3 m telescope at Lick Observatory, led by Brad Holden, was made possible through generous gifts from the Heising-Simons Founda-

tion, William and Marina Kast, and the University of California Observatories. Research at Lick Observatory is partially supported by a generous gift from Google. We appreciate the excellent assistance of the staff at Lick Observatory. NASA/IPAC Extragalactic Database (NED) is operated by the Jet Propulsion Laboratory, California Institute of Technology, under contract with NASA.

Chapter 5

Imaging Polarimetry of Tidal Disruption Events

5.1 Introduction

In the preceding chapter of this thesis, we ventured into the relatively new domain of spectropolarimetry applied to tidal disruption events (TDEs), an area where data remain scarce. The study of the TDE AT 2019qiz, in particular, served as a pioneering effort, shedding light on the polarimetric characteristics of these extraordinary events. However, the rarity of bright TDEs poses a significant hurdle to their spectropolarimetric analysis. Our fortunate encounter with AT 2019qiz, a TDE that was both luminous and close enough for the Kast spectropolarimeter on the 3 m Shane telescope at Lick Observatory to detect its polarization, underscored the scarcity of such ideal candidates for spectropolarimetry. The majority of TDEs, being much fainter, elude observations with instruments like the Kast polarimeter, prompting us to turn to larger telescopes.

This chapter introduces an ambitious undertaking: the extension of TDE spectropolarimetry to a larger sample of events using the Low Resolution Imaging Spectrometer polarimeter (LRISp; Oke et al. 1995; Goodrich et al. 1995) mounted on the Keck-I 10 m telescope. The primary motivation behind employing LRISp for a TDE polarimetry program hinges on its potential to enable polarimetric measurements of TDEs at late times ($\gtrsim$ 100 days) and, by extension, to extract insights into the polarization contribution of their host galaxies. One of the known challenges in the polarimetric analysis of TDEs is the contamination from the starlight of their host galaxies (Patra et al. 2022a; Leloudas et al. 2022; Liodakis et al. 2023). Some researchers (e.g., Leloudas et al. 2022; Liodakis et al. 2023) have operated under the assumption that the starlight in these host galaxies exhibits zero polarization, a simplification that might not hold true in all cases. The importance of testing this assumption cannot be overstated, as it directly impacts the accuracy of our

measurements and our understanding of the intrinsic polarization of TDEs.

To address this problem, the work presented here includes polarization measurements of TDE host galaxies at a point when the TDE itself has faded below the flux of the background starlight at optical wavelengths, which typically happens a few hundred days after peak brightness. This method allows us to isolate and examine the polarization contribution from the host galaxy, thereby refining our understanding of the host's influence on the observed polarization of TDEs. Additionally, late-time polarization measurements allow us to constrain the level of interstellar polarization in the host galaxy. By leveraging the larger 10 m mirror of the Keck telescope, we aim to target TDEs as faint as $V = 20$ mag, a feat unattainable with smaller instruments like the Shane telescope's Kast polarimeter. In essence, this chapter aims to pivot from the singular case study of AT 2019qiz to a more expansive examination of TDE spectropolarimetry.

While spectropolarimetry of TDEs would be ideal because it offers spectral information, including emission and absorption lines, our focus here is on imaging polarimetry. This choice is driven by the fact that imaging enables us to reach deeper, approximately $V = 20$ mag, whereas spectropolarimetry with LRISp is limited to $V \approx 18$ mag, a depth at which there is still an insufficient number of TDEs for a comprehensive study.

5.2 Observations and Data Reduction

Imaging polarimetry data were acquired using the polarimetry module of the LRIS instrument on the Keck-I telescope on UT June 13, 2023, and UT December 13, 2023. LRIS is equipped with two channels: the blue side and the red side, both optimized for different parts of the optical spectrum. The blue side of LRIS utilizes a Marconi Astronomical Research Camera with a detector size of 2048×4096 pixels, each pixel measuring $15\,\mu$m. This side of the instrument is specifically optimized for shorter, blue wavelengths and records images using the B and V filters at a scale of $0.135''$ per pixel. Conversely, the red side is equipped with a 4096×4096 pixel detector manufactured by the Lawrence Berkeley National Laboratory (LBNL), also featuring a pixel size of $15\,\mu$m, but it is optimized for capturing red and near-infrared wavelengths with R and I filters. The imaging polarimetry mode in LRIS has a significantly reduced field of view (FoV), approximately $30' \times 30'$. This limitation stems from the need to capture both ordinary and extraordinary images on the detector in the polarimetry mode.

Reduction of the science images followed the standard process: each image underwent bias subtraction, overscan correction, cosmic ray removal, and flat fielding to correct for detector imperfections. Flux calibration of images was *not* performed, as it is not essential for calculating the Stokes parameters. Aperture photometry was carried out with the Photutils module of Astropy Astropy Collaboration et al. (2022). The flux centroid of each source was computed to establish a precise location for the aperture setting. Apertures were

then centered on these centroids and set to 1.5 times the full width at half-maximum intensity (FWHM) of the point-spread function (PSF). This aperture sizing was strategically chosen to maximize the capture of light from the source while minimizing the inclusion of background noise. Owing to the TDE targets being located at the centers of galaxies, sky-background annuli were positioned very close to the edge of the target aperture, typically within 3–5 pixels. This close setting is helpful (although not perfect) for effective subtraction of starlight from the host galaxy. An example of an image acquired by LRISp is shown in Figure 5.1.

To calculate polarization, we begin by defining the parameter G, which describes the sensitivity difference between the ordinary (top) and extraordinary (bottom) images captured by LRISp. Notably, LRISp exhibits a large sensitivity difference between these images compared to the Kast spectropolarimeter. The parameter G is calculated as

$$G = \sqrt{\frac{f_{b,0}\, f_{b,45}}{f_{t,0}\, f_{t,45}}}\,. \tag{5.1}$$

Here, f represents the measured flux and the subscripts show whether the flux came from the top or the bottom image, along with the waveplate position angles. Next, we calculate the Stokes parameter q at waveplate positions of 0° and 45°. The calculations for q at these positions are given by

$$q_0 = \frac{f_{b,0} - G\, f_{t,0}}{f_{b,0} + G\, f_{t,0}} \tag{5.2}$$

and

$$q_{45} = \frac{G\, f_{t,45} - f_{b,45}}{G\, f_{t,45} + f_{b,45}}\,, \tag{5.3}$$

respectively.
The final Stokes parameter q is then determined by averaging q_0 and q_{45}:

$$q = 0.5(q_0 + q_{45})\,. \tag{5.4}$$

Similarly, the Stokes parameter u is calculated using the exposures at waveplate positions of 22.5° and 67.5°. The subsequent calculations for the polarization magnitude (p) and the position angle (PA) follow the calculations described in Chapter 2.

5.3 Calibrating LRISp

During our planning for observations using LRISp on the Keck 10 m telescope, we identified a need for fainter polarization standard stars. Typically, spectropolarimetric standard stars have a brightness of about $V \approx 10$ mag, which causes saturation in exposures as

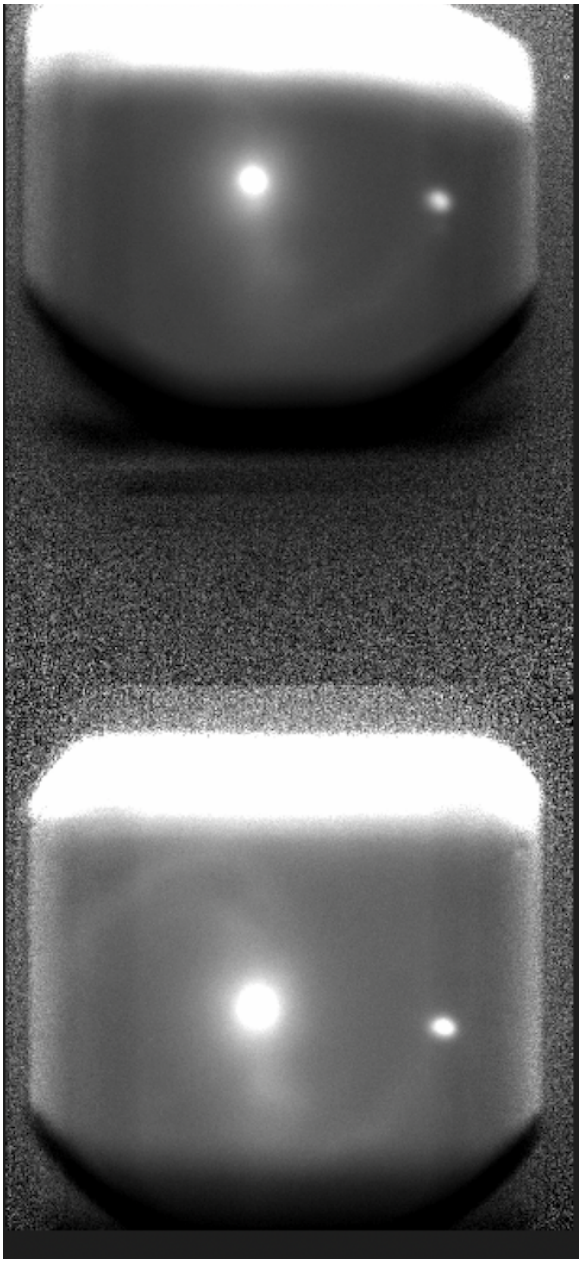

Figure 5.1: An image of AT 2019qiz in the *B* filter with LRISp showing both the ordinary (top) and extraordinary (bottom) images.

short as 1 s at Keck. Additionally, we aimed to avoid very short exposure times because the shutter movement of the Keck telescope, which takes about 50–60 ms, comprises $\sim 5\%$ of a 1 s exposure. Such brief exposures can lead to systematic polarization variations around 5%. Consequently, we sought new, fainter polarization standards suitable for the imaging mode of LRISp.

We selected two high-polarization and two null-polarization standards from the *Gaia* dataset (Gaia Collaboration et al. 2018). Our selection criteria were (i) a brightness of $13 < G < 16$ mag, (ii) proximity within $10'$ of known spectropolarimetric standard stars on the sky, and (iii) a parallax such that the high-polarization standard is at least 1 kpc away and the null-polarization standard is less than 1 kpc away. The latter two conditions ensure that the polarization of the fainter standards is comparable to that of the known standards owing to effectively the same dust columns along their lines of sight. These candidates were first verified with the Kast spectropolarimeter to establish baseline polarization and position angles across different wavelengths.

Subsequent observations of these standards LRISp were conducted on nights dedicated to the polarimetry of TDEs. The polarization measurements of the standard stars are documented in Table 5.1, and their comparison with the baseline values obtained from Shane/Kast are illustrated in Figures 5.2 through 5.5.

This comparison between LRISp and Kast measurements was crucial, as it highlighted significant issues with LRISp. We discovered that the Stokes q and u parameters in LRISp are reversed, likely due to mislabeled waveplate positions within the instrument. Additionally, we observed internal reflections ("ghosts") very close to the target's PSF, complicating accurate flux extraction. Based on these observations, we estimate the systematic uncertainty in polarization measurements with LRISp to be $\sim 0.25\%$.

5.4 Preliminary Results

Having calibrated LRISp and established its reliability for extracting reasonably accurate polarization measurements, we present the results of polarization observations for five TDEs at various stages of their evolution, from 20 days to over 1500 days post-peak brightness in optical wavelengths. The polarization data for these TDEs are summarized in Table 5.2 and depicted in Figure 5.6. Generally, the polarization levels of these TDEs are low and largely consistent with 0% polarization, except for AT 2023xen, which exhibits about 1% polarization observed 21 days after peak brightness. Note that, as discussed in Chapter 4, AT 2019qiz also showed 1% polarization approximately 25 days post-peak. This may be an early hint for similar evolution of the tidal debris in these two TDEs.

Except for AT 2023xen, the observed polarization likely originates from the starlight of the host galaxy, as the TDEs typically fade into the stellar background several hundred days after reaching peak brightness. The host galaxy of AT 2020mot shows polarization

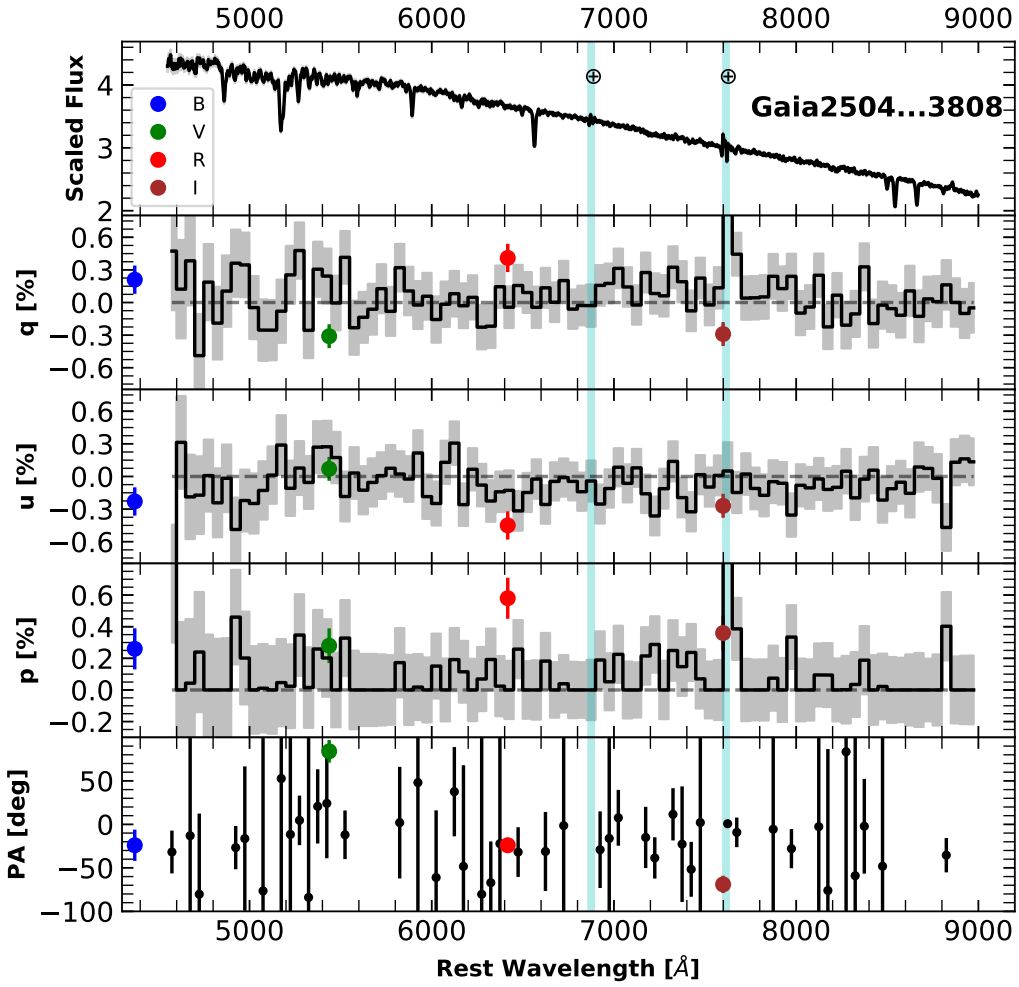

Figure 5.2: Comparison between LRISp and Kast for the null-standard star Gaia2504724807045303808. Kast data are shown in black whereas LRISp data are with colors denoting the different filters.

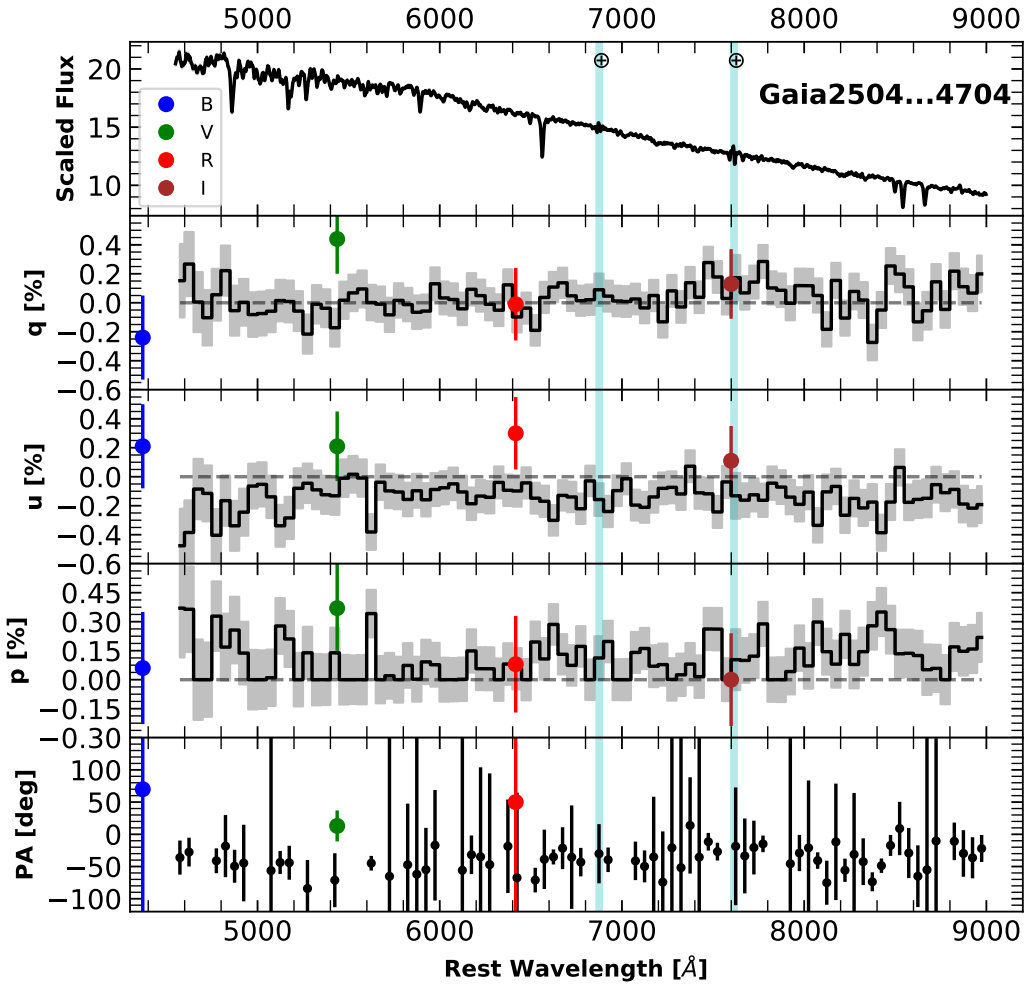

Figure 5.3: Similar to Figure 5.2 but showing comparison between LRISp and Kast for the null-standard star Gaia2504739959689944704.

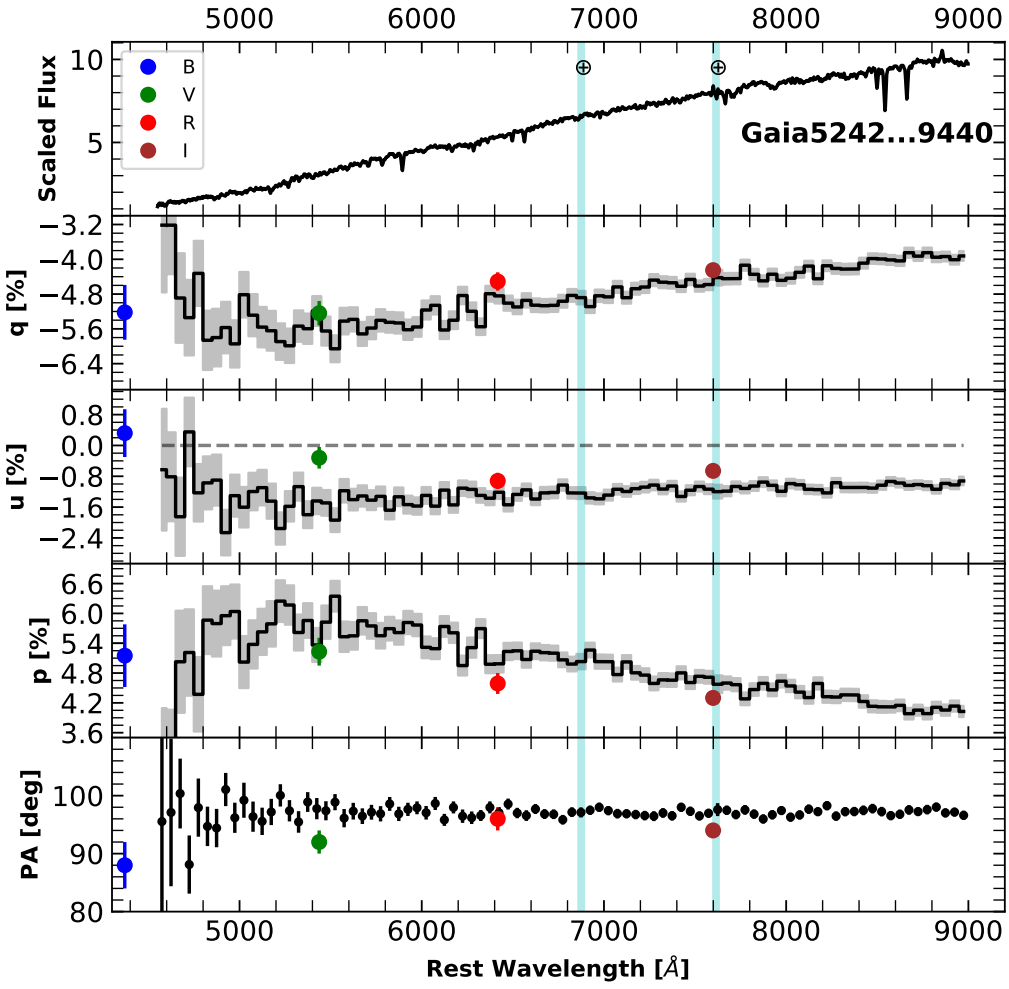

Figure 5.4: Similar to Figure 5.2 but showing comparison between LRISp and Kast for the high-polarization standard star Gaia524279927616349440.

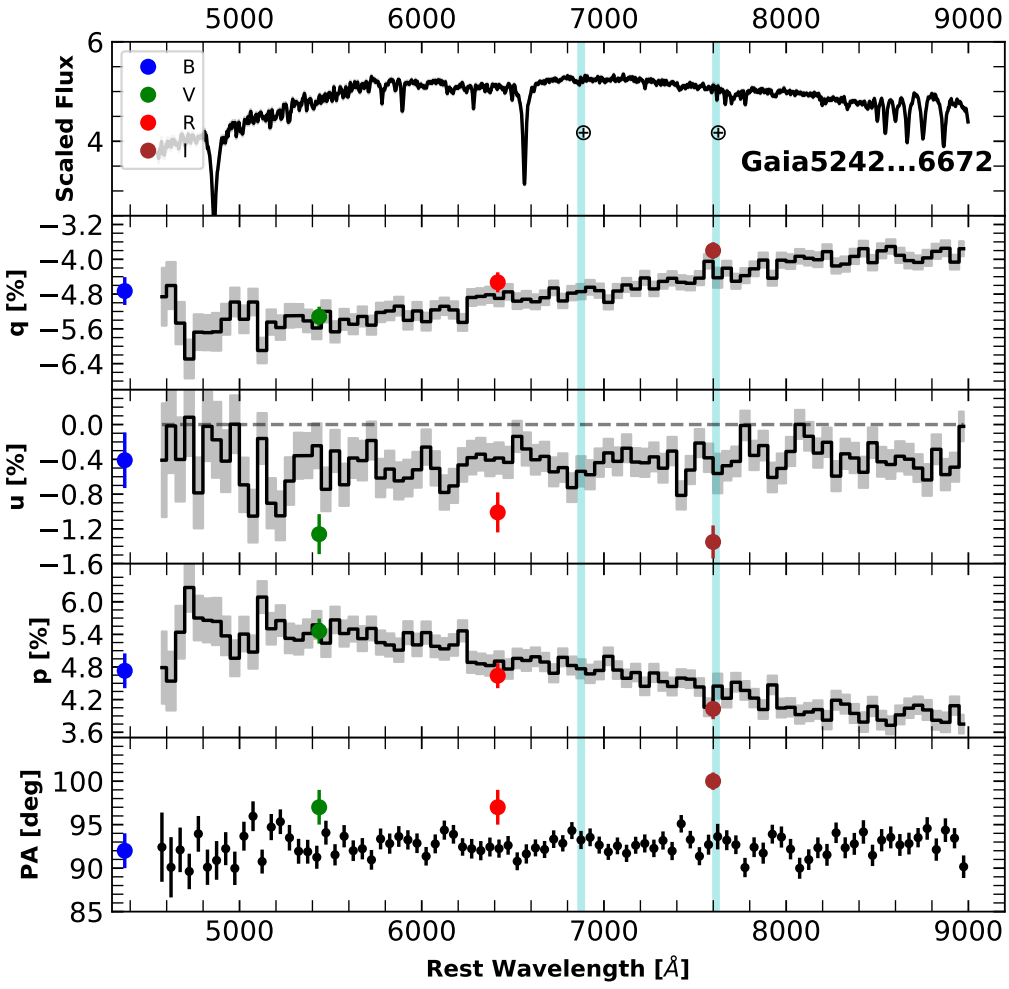

Figure 5.5: Similar to Figure 5.2 but showing comparison between LRISp and Kast for the high-polarization standard star Gaia5242809941503667 2.

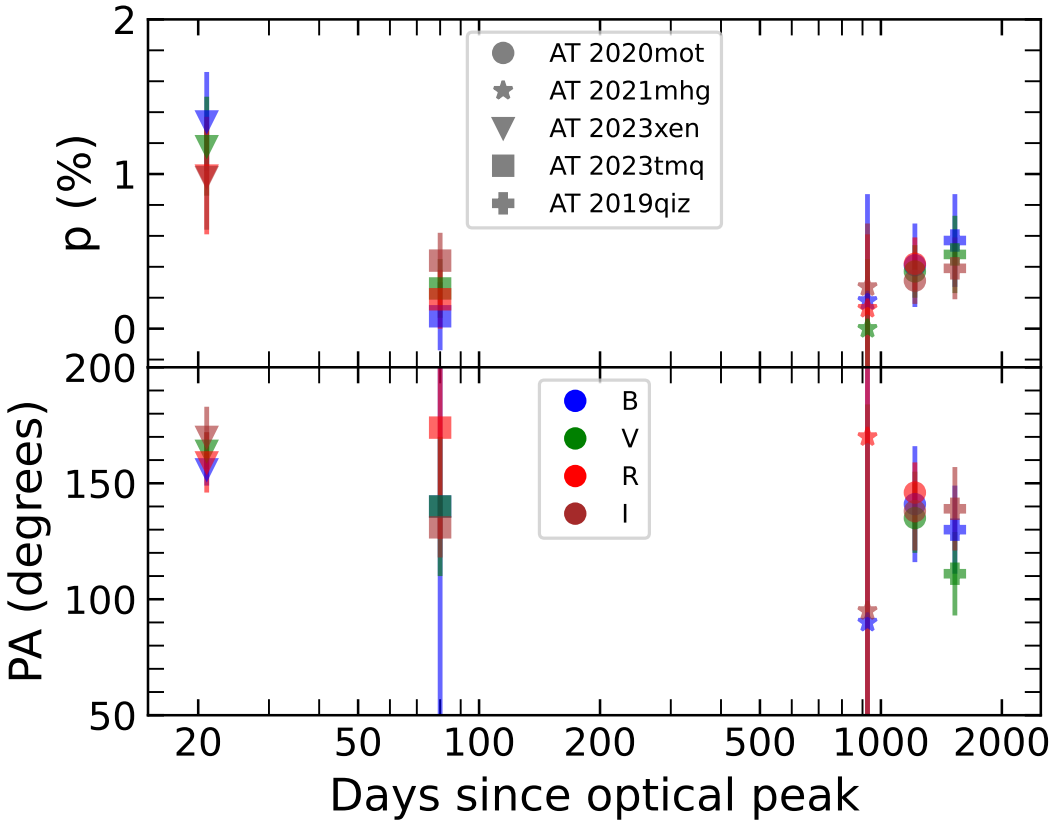

Figure 5.6: Polarization and position angle of TDEs. The colors denote the different filters whereas the shapes represent different TDEs.

Standard Star	Pol. Type	Filter	q(%)	u(%)	p(%)	PA (°)
Gaia2504724807045303808	Low	B	0.21(13)	−0.23(13)	0.26(13)	156(18)
		V	−0.31(11)	0.07(11)	0.28(11)	84(13)
		R	0.41(13)	−0.45(13)	0.58(13)	156(6)
		I	−0.29(11)	−0.27(11)	0.36(11)	111(10)
Gaia2504739959689944704	Low	B	−0.24(29)	0.21(29)	0.06(29)	70(650)
		V	0.44(24)	0.21(24)	0.37(24)	13(24)
		R	−0.01(25)	0.30(25)	0.08(25)	50(330)
		I	0.13(24)	0.11(24)	0.00(24)	–
Gaia524279927616349440	High	B	−5.22(63)	0.32(62)	5.15(63)	88(4)
		V	−5.24(28)	−0.32(28)	5.23(28)	92(2)
		R	−4.51(21)	−0.92(21)	4.59(21)	96(2)
		I	−4.25(15)	−0.66(15)	4.30(15)	94(1)
Gaia524280099415036672	High	B	−4.73(32)	−0.41(32)	4.73(32)	92(2)
		V	−5.32(23)	−1.26(23)	5.46(23)	97(2)
		R	−4.53(23)	−1.01(23)	4.64(23)	97(2)
		I	−3.80(19)	−1.35(19)	4.03(19)	100(1)

Table 5.1: Imaging polarimetry of standard stars observed with Keck LRISp on UT Dec 13, 2023. Statistical uncertainty in the last few significant figures is provided in parentheses next to each measurement. For e.g., 0.07 ± 0.11 is written as 0.07(11) and 32 ± 24 is written as 32(24).

at the 0.3–0.4% level, and AT 2019qiz at 0.5%, whereas the host of AT 2021mhg has 0% polarization. This was indeed one of the objectives driving this project — to investigate whether the starlight in the host galaxy exhibits any polarization.

The availability of data across multiple filters also proves extremely beneficial as it allows for consistency checks. Since the primary source of polarization in TDE photospheres is wavelength-independent electron scattering, the polarization measurements across all four filters should be similar to first order. However, differences may arise due to polarization effects within specific spectral lines. Notably, the Hα line is known to be depolarized in TDEs, which could lead to lower observed polarization in the R band (Patra et al. 2022a; Leloudas et al. 2022).

The generally low polarization observed in many TDEs has significant implications. As discussed in Chapter 4, this suggests that TDEs likely possess highly spherical photospheres, potentially due to strong outflows. This observation supports reprocessing models for the source of optical emission rather than shocks occurring within highly asymmetrical tidal streams.

TDE	Obs. Date (UT)	Phase (days)	Filter	q(%)	u(%)	p(%)	PA (°)
AT 2020mot	Dec-13-2023	1215	B	0.12(27)	−0.53(27)	0.41(27)	141(25)
			V	−0.01(17)	−0.44(17)	0.37(17)	135(15)
			R	0.19(17)	−0.43(17)	0.42(17)	146(13)
			I	0.03(15)	−0.37(15)	0.31(15)	138(17)
AT 2021mhg	Dec-13-2023	926	B	−0.79(69)	−0.07(68)	0.18(69)	100(500)
			V	−0.23(45)	0.03(42)	0.00(45)	–
			R	0.54(48)	−0.10(48)	0.13(48)	170(430)
			I	−0.56(41)	−0.10(40)	0.27(41)	95(89)
AT 2023xen	Dec-13-2023	21	B	0.93(31)	−1.05(32)	1.34(32)	156(7)
			V	1.07(32)	−0.67(33)	1.18(32)	164(8)
			R	0.83(39)	−0.74(38)	0.99(38)	159(13)
			I	1.06(34)	−0.40(36)	0.98(34)	170(13)
AT 2023tmq	Dec-13-2023	80	B	0.06(22)	−0.26(22)	0.08(22)	140(270)
			V	0.10(19)	−0.34(19)	0.26(19)	140(30)
			R	0.30(19)	−0.07(19)	0.19(19)	174(48)
			I	−0.07(17)	−0.50(18)	0.44(18)	131(13)
AT 2019qiz	Dec-13-2023	1528	B	−0.11(30)	−0.69(30)	0.57(30)	130(19)
			V	−0.43(25)	−0.39(24)	0.48(25)	111(18)
			I	0.08(20)	−0.47(20)	0.39(20)	139(18)

Table 5.2: Imaging polarimetry of TDEs observed with Keck LRISp. Statistical uncertainty in the last few significant figures is provided in parentheses next to each measurement. For example, 0.07 ± 0.11 is written as 0.07(11) and 32 ± 24 is written as 32(24). Note that the *R*-band image of AT 2019qiz was severely affected by cosmic rays, and consequently was omitted from the analysis.

5.5 Future Work

The results presented here are part of an ongoing project aimed at increasing the sample of TDEs with polarimetric measurements. Crucially, this project seeks to construct a time series of polarization at different phases of a TDE's evolution. Doing so has the potential to delineate the phases at which shocks within tidal streams play a significant role versus when outflows predominate. Moreover, acquiring additional polarization measurements could help constrain the currently uncertain circularization timescale of the accretion disk that forms post-disruption.

Equipped with the late-time polarization measurements detailed in this study, there is a need to revisit earlier polarization observations of these TDEs and adjust them for host light contamination to determine the true level of polarization. For example, the reported polarization of AT 2020mot is around 25%, which has been cited as evidence for shocks within tidal streams (Liodakis et al. 2023). However, this analysis assumes that the host-galaxy light is unpolarized. Contrary to this assumption, our findings indicate that the host galaxy's polarization is actually about 0.4%. Therefore, future work will involve correcting the polarization data of TDEs to reflect these interpretations accurately. Additionally, we plan to continue collecting more TDE polarimetry data with LRISp to further this work.

Chapter 6

Constraints on the Narrow-Line Region of the X-ray Quasi-periodic Eruption Source GSN 069

An earlier version of this chapter was accepted by the Monthly Notices of the Royal Astronomical Society (MNRAS) for publication as Patra, Kishore C.; Lu, Wenbin; Ma, Yilun; Quataert, Eliot; Miniutti, Giovanni; Chiaberge, Marco; Filippenko, Alexei V.; Beatriz Agís González, MNRAS, in press.

6.1 Chapter Abstract

The origins of quasi-periodic eruptions (QPEs) are poorly understood, although most theoretical explanations invoke an accretion disk around a supermassive black hole. The gas and stellar environments in the galactic nuclei of these sources are also poorly constrained. In this paper, we present an analysis of archival *Hubble Space Telescope (HST)* images to study the narrow-line [O III] emission in the QPE source GSN 069. We find strong evidence for a compact nuclear [O III] emission region of size $\lesssim 35$ pc, overlaid on top of extended [O III] emission up to 2 kpc away from the nucleus. The age of the accretion system is estimated to be between 10 and 100 yr. The [O III] luminosity of the compact region was measured to be $(2.1 \pm 0.3) \times 10^{40}$ erg s^{-1}. Based on CLOUDY simulations, we constrain that the [O III] emitting gas has a hydrogen number density in the range $2 \times 10^3 < n_{\rm H} \lesssim 10^8$ cm^{-3} and volume filling factor $f_{\rm V} < 4 \times 10^{-3}$. We suggest that the dense gas in the nuclear region of GSN 069 originates from molecular clouds (with total mass $\gtrsim 3 \times 10^3\ M_\odot$), which are freshly ionised by the soft X-ray photons from the accretion disk. We predict possible evolution of the compact narrow-line region on emission-line diagnostic diagrams, and hence future *HST* or integral-field unit observations can be used

to further pin down the age of this puzzling system.

6.2 Introduction

Quasi-periodic eruptions (QPEs) are a new class of X-ray sources identified by wide-field X-ray surveys. These enigmatic objects exhibit distinctive characteristics, featuring bursts of bright X-ray emission superimposed on top of quiescent emission consistent with steady-state accretion around a supermassive black hole (SMBH). The quasi-periodic recurrence times range from a few hours up to a day in the currently known sample. In the X-ray band, the spectra of QPEs are thermal-like, with higher temperatures ($k_{\rm B}T \approx 100\,{\rm eV}$) during the eruption phase and lower temperatures ($k_{\rm B}T \approx 50\,{\rm eV}$) in quiescence. The flare amplitude can reach 100 times that of the quiescent phase at the highest X-ray energies. QPEs are predominantly detected in the nuclei of low-mass galaxies (stellar mass $M_* \approx 10^9\,M_\odot$), implying that these sources are likely associated with relatively low-mass SMBHs. To date, only 9 QPE sources or candidates have been discovered: GSN 069 (Miniutti et al. 2013; Shu et al. 2018; Miniutti et al. 2019), RX J1301.9+2747 (Sun et al. 2013; Shu et al. 2017; Giustini et al. 2020), eRO-QPEs 1-4 (Arcodia et al. 2021, 2022, 2024; Chakraborty et al. 2024), *Swift* J0230+28 (Guolo et al. 2024), XMMSL1 J024916.6-04124 (Chakraborty et al. 2021), and "Tormund" (Quintin et al. 2023), with the latter two considered QPE candidates. Given the small number of known QPEs and sparse temporal/wavelength coverage of them, there is limited knowledge regarding their origin(s), emission processes, lifetime, and periodicity, making them a novel and exciting prospect for understanding the physical processes near these low-mass SMBHs.

Several theoretical frameworks have been proposed to explain the origin of QPEs, spanning concepts such as disk instabilities (Raj & Nixon 2021; Pan et al. 2022, 2023; Kaur et al. 2023), mass transfer from various configurations of orbiting bodies (Chen et al. 2022; King 2020, 2022; Krolik & Linial 2022; Metzger et al. 2022; Wang et al. 2022; Zhao et al. 2022; Linial & Sari 2023), and interactions between a secondary orbiting object and the accretion disk around the primary SMBH (Suková et al. 2021; Xian et al. 2021; Lu & Quataert 2023; Franchini et al. 2023; Linial & Metzger 2023). A connection between QPEs and tidal-disruption events (TDEs) has also been proposed (see, e.g., Xian et al. 2021; Wang et al. 2022; King 2020; Linial & Metzger 2023; Wang 2024). Apparently, three of the currently known QPE sources/candidates might be associated with X-ray-selected TDEs (GSN 069, XMMSL1, and "Tormund"; Miniutti et al. 2023a; Chakraborty et al. 2021; Quintin et al. 2023). A common theme among all the aforementioned models is an accretion disk, whose X-ray emission has been detected (during the quiescence phase) in at least some of the QPE sources. There is some indication that these accretion disks may be compact in size, as inferred from the lack of broad optical emission lines and near-infrared (IR) dust emission typically associated with active galactic nuclei (AGN; Wevers et al. 2022). However, the

disk properties (e.g., accretion rate, mass feeding source, and radial structure) are currently poorly constrained. Much also remains unknown about the gas and stellar environments in these galactic nuclei.

In this paper, we present the analysis of *Hubble Space Telescope (HST)* images to study the narrow-line region in the nucleus of the first-ever QPE source GSN 069 [α(J2000) = $01^{hr}19^{m}08.61^{s}$; δ(J2000) = $-34°11'30.13''$; z = 0.018]. GSN 069 was first discovered in July 2010 during an *XMM-Newton* slew (Saxton et al. 2011), exhibiting a flux over 240 times higher than previous *Roentgen Satellite (ROSAT)* observations from 1994 (Miniutti et al. 2013). Subsequent observations with the *Swift* X-Ray Telescope (XRT) indicated a relatively steady X-ray flux for around a year (Miniutti et al. 2013). *Swift* and *XMM-Newton* further showed a gradual decline in flux over the next decade (Shu et al. 2018). Notably, QPEs — X-ray flares with high amplitude and short duration, repeating approximately every 9 hr — were observed during *XMM-Newton* and *Chandra* observations between December 2018 and February 2019 (Miniutti et al. 2019). Mysteriously, the QPE phenomenon in this source goes on and off together with secular evolution of the quiescent X-ray flux (Miniutti et al. 2023b,a).

This paper is organised as follows. Section 6.3 provides details on the archival *HST* images and the process of creating a continuum-subtracted image for the [O III] line emission. In Section 6.4, we describe our photometry model along with the results. Subsequently, we present our Cloudy modeling along with constraints on the [O III]-emitting gas in Section 6.5. We discuss our findings and conclusions in Sections 6.6 and 6.7, respectively.

6.3 HST Images

Archival *HST* images of GSN 069 were retrieved from the Mikulski Archive for Space Telescopes (MAST). These images were originally obtained in *HST* Cycle 27 (Program ID 16062; PI: G. Miniutti) in August and November 2020 with the goal, among others, to study the spatially-resolved structure of the narrow-line region. Five images were obtained with the Advanced Camera for Surveys (ACS) over two *HST* orbits: two far-ultraviolet (UV) band (F140LP, F165LP) images, one narrow-band optical image to capture the [O III] emission (FR505N), a medium-band image (FR647M) for the continuum near the [O III] line, and a wide-band optical image (F606W) to study the spatially-resolved stellar structure. Table 6.1 provides a summary of the *HST* observations including the filters, observation dates, exposure times, and the central wavelengths $\lambda_{\rm centre}$ and full width at half maximum intensity (FWHM) of the filter throughput functions. The filter functions are shown in Figure 6.1. The middle segment of the ramp filter FR505N with central wavelength 5099 Å was used to capture the [O III] λ4959 and λ5007 lines which were redshifted to 5046 Å and 5097 Å (respectively) by the recession of the host galaxy GSN 069 at redshift z = 0.018. Standard *HST* reductions and calibrations were carried out with *AstroDrizzle*.

Filter	UT Date (yyyy-mm-dd)	λ_{centre} [Å]	FWHM [Å]	T_{exp} [s]
F140LP	2020-11-19	1476	226	1000
F165LP	2020-11-19	1740	200	1000
FR505N	2020-08-16	5099	105	700
FR647M	2020-08-16	5757	499	160
F606W	2020-08-16	5962	2253	800

Table 6.1: Summary of *HST* observations of GSN 069.

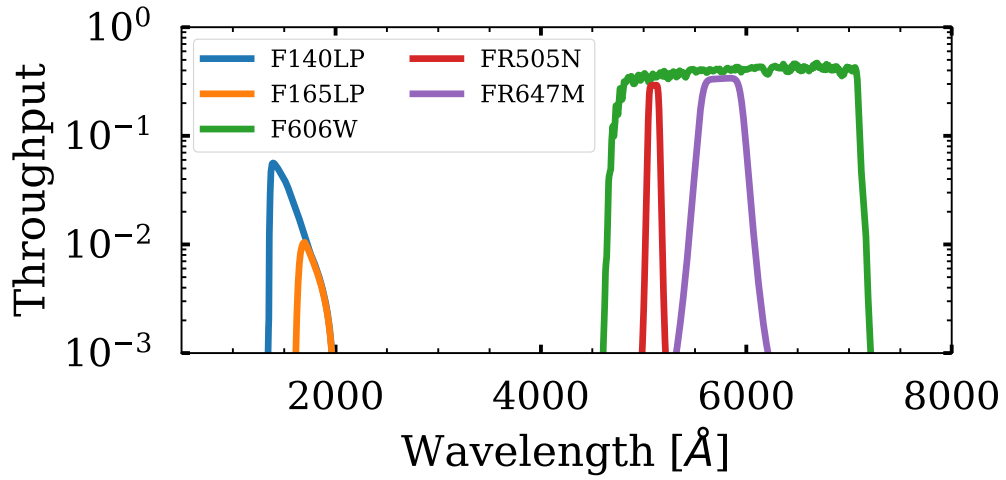

Figure 6.1: The throughput functions of the *HST* filters in which the images of GSN 069 were obtained.

The FR505N image contains both the [O III] line and continuum fluxes, and we first created the continuum-subtracted [O III] image as follows. Since the available images lacked a sufficient number of resolved stars, registering the FR505N (on-band) and FR647M (continuum) images based on stars was not feasible. Instead, we computed the photometric centroids of the galactic nuclei in both the on-band and continuum images. Subsequently, we generated a 100×100 pixel ($\sim 2\,\mathrm{kpc} \times 2\,\mathrm{kpc}$ in physical size) cutout centred around each centroid. Despite the centroid's accuracy being better than an *HST* pixel, subtraction between the two images is no better than one pixel. To address this challenge, we employed a strategy of supersampling — we increased the resolution of both cutout images by a factor of 5 through polynomial interpolation between adjacent pixels. For each image, the pixel counts in units of electron s^{-1} were converted to flux density in units of $\mathrm{erg\,s^{-1}\,cm^{-2}\,\AA^{-1}}$ using the PHOTFLAM keyword in the image headers. Subsequently, we subtracted the supersampled continuum cutout from the supersampled on-band cutout, both expressed in flux-density units.

Figure 6.2 presents the resultant continuum-free image displaying the [O III] emission. It is apparent that the surface brightness profile of [O III] emission has a cusp structure near the nucleus and a number of elongated structures away from the nucleus. Based on the [O III] image alone, it is not clear whether these structures reflect the spatial distribution of dense gas or sources of ionising photons or both. To gauge the systematic uncertainty associated with the [O III] flux due to the process of image subtraction, a deliberate misalignment of the images in random directions, each by a slight amount (1-2 supersampled pixels), was undertaken. This procedure allowed us to determine the average systematic difference in [O III] flux as a function of the distance from the centre. The resultant systematic-error function was then combined with the statistical error to estimate the comprehensive uncertainty linked to the flux measurement.

In Figure 6.3, we show the far-UV (F140LP−F165LP)[1] and broad-band optical (F606W) images for comparison. From the fact that the elongated structures on larger scales $\gtrsim 0.3\,\mathrm{kpc}$ in the [O III] image do not appear to correspond to any features in the far-UV image (young stars) and the broad-band optical image (young and old stars), we infer that the [O III] emission on larger scales is not dominated by the photoionised (H II) regions near young stars. We leave a detailed analysis of the spectral energy distributions of the nucleus and the surrounding stars to a future work, whereas in this paper we focus on the [O III] emission.

[1]The *HST* Solar Blind Camera (SBC) has a known problem of red leak for wavelengths $> 2000\,\mathrm{\AA}$. To remove the contaminating flux from longer wavelengths, and to get the true UV flux between 1400 and 1600 Å, we subtracted the two far-UV images F140LP and F165LP. This works because the throughput function of F165LP is contained entirely within the throughput function of F140LP as can be seen in Figure 6.1.

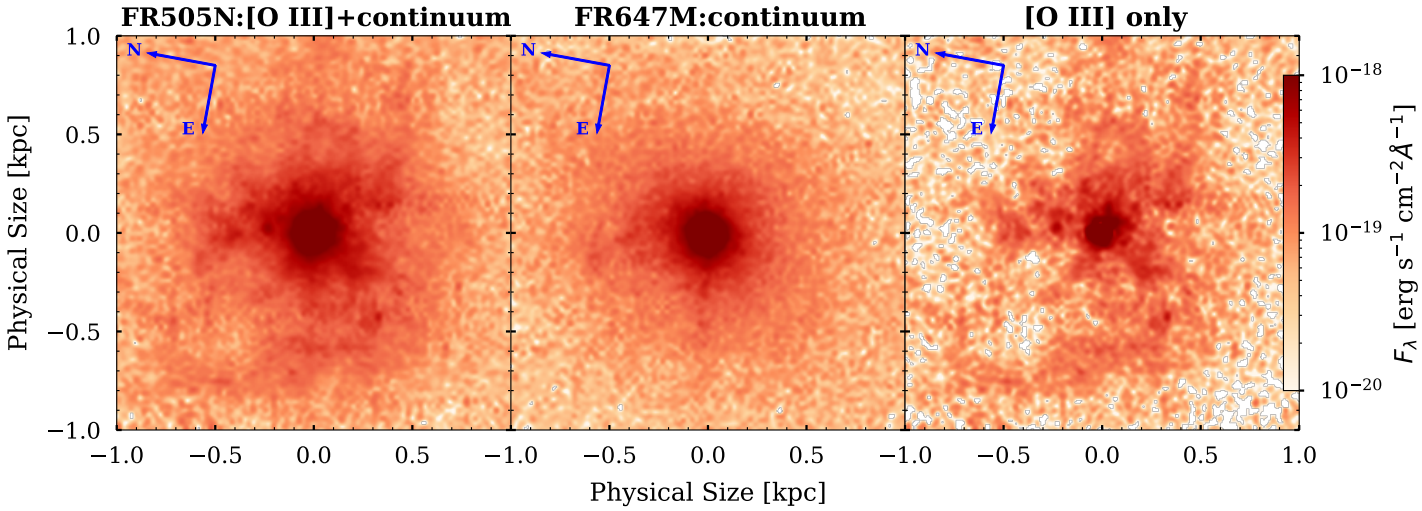

Figure 6.2: The left panel displays the *HST* image in the narrow-band filter FR505N which captures [O III] emission at 4958.9 Å and 5006.9 Å, along with the continuum emission. The middle panel shows the continuum image in filter FR647M, whereas the right panel presents the continuum-subtracted image of GSN 069. All three panels are plotted on the same flux-density scale to enable direct comparison.

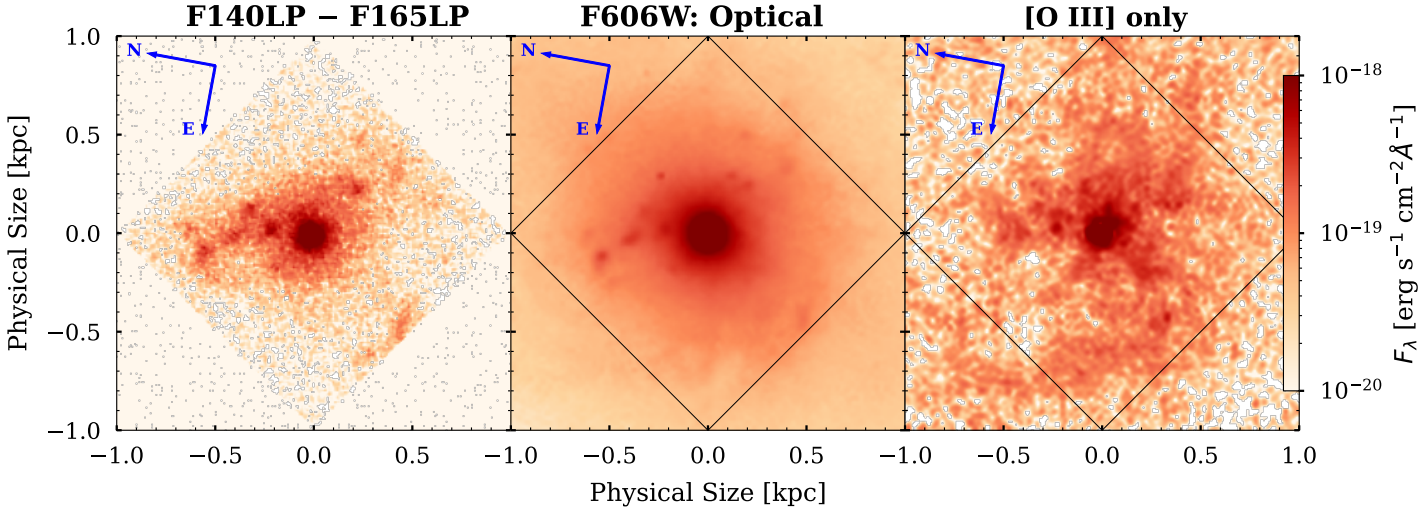

Figure 6.3: The left panel shows the far-UV image created by subtracting F165LP from F140LP. The middle panel displays the broad-band F606W optical image. The continuum-free [O III] emission image is reproduced for comparison in the right panel. All three panels are plotted on the same flux-density scale for comparison.

6.4 Photometry

Aperture photometry was performed using Astropy's Photutils module (Astropy Collaboration et al. 2022). Annular apertures of varying radii were centred on the calculated centroid of the continuum-free [O III] image. The median surface flux density $\mu_{\lambda,\mathrm{o}}(r)$ was calculated in each annular aperture. We modeled the observed [O III] image as a convolution of a source image with a point-spread function (PSF),

$$\mu_{\lambda,\mathrm{o}}(x,y) = \int \mathrm{d}x'\,\mathrm{d}y'\mu_{\lambda,\mathrm{s}}(x',y')K(\Delta r), \tag{6.1}$$

where $\Delta r = \sqrt{(x-x')^2+(y-y')^2}$, $\mu_{\lambda,\mathrm{o}}(x,y)$ is the observed flux density at pixel position (x,y), $\mu_{\lambda,\mathrm{s}}(x',y')$ is the flux density of the source, and $K(\Delta r)$ is the PSF, also known as the kernel function in the context of convolution. We used the PSF of the filter F555W which encapsulates the relevant wavelengths of both FR505N and FR647M. Annular photometry was subsequently carried out on the convolved image to get a model surface flux density as a function of radius $r = \sqrt{x^2+y^2}$.

Two source models were tested, with the first being a power law model given by

$$\mu_{\mathrm{s}}(r) = \mu_0\left(\frac{r}{r_0}\right)^{-b}, \tag{6.2}$$

where μ_0 is the surface flux density at a fixed reference radius $r_0 = 50\,\mathrm{pc}$ (the results do not depend on this choice), and b is the power-law index. To overcome the numerical singularity at $r = 0$, the value of the central pixel was extrapolated using the gradient at immediately adjacent pixels. The second model was a power-law model plus a point source given by

$$\mu_{\mathrm{s}}(r) = \mu_0\left(\frac{r}{r_0}\right)^{-b} + A\delta[r], \tag{6.3}$$

where A is the amplitude (in units of surface flux density) of the discrete unit sample function $\delta[r]$, which is defined as

$$\delta[r] = \begin{cases} 1, & \text{if } r = 0 \\ 0, & \text{otherwise.} \end{cases}$$

Figure 6.4 shows the annular photometry along with the best-fit models, whereas Figure 6.5 shows the posterior distributions of the fitted parameters for the two models. Table 6.2 displays the measured flux density within circular apertures of various sizes for all *HST* images of GSN 069. We acknowledge that the PSF of F555W is merely an approximation of the PSF of the continuum-free image. However, the fitted parameters in Equations 6.2 and 6.3 exhibited relative robustness when different optical band filters' PSFs were utilised.

The power-law model does not provide a good fit to the observed data, as indicated by a reduced chi-squared of $\chi^2_{\rm red} = 3.5$ with 19 degrees of freedom (dof). The Bayesian Information Criterion (BIC), defined as BIC $\equiv \chi^2 + k \ln n$, where k represents the number of free parameters in the model and n is the quantity of data points, yields a BIC value of 72 for this model. In contrast, the power-law + point-source model demonstrates an excellent fit to the data, with $\chi^2_{\rm red} = 1.1$ with 18 degrees of freedom and a BIC of 29. The evidence strongly favours the power law + point-source model over the power-law model. Although we do not exhaust all possible parametrised models with more parameters (e.g., a 4-parameter Gaussian + power-law model, or a 4-parameter broken-power-law model), our preferred power-law + point-source model provides an excellent fit to the data with only three parameters.

We interpret these results as being consistent with the existence of a compact, unresolved source of [O III] emission within the nucleus of GSN 069, superimposed onto an extended power-law distribution of [O III] emission. The best-fit values for the free parameters in the power-law + point-source model are $\log \mu_0 = -18.11 \pm 0.02\,{\rm erg\,s^{-1}\,cm^{-2}\,\AA^{-1}}$, $b = 1.08 \pm 0.06$, and $\log A = -15.25 \pm 0.06\,{\rm erg\,s^{-1}\,cm^{-2}\,\AA^{-1}}$. The measured $\log A$ parameter corresponds to a luminosity of the compact [O III] source of $(2.1 \pm 0.3) \times 10^{40}\,{\rm erg\,s^{-1}}$. We discuss the implications of these results in the next section. On the other hand, the best-fit values for the free parameters in the power-law-only model are $\log \mu_0 = -18.00 \pm 0.01\,{\rm erg\,s^{-1}\,cm^{-2}\,\AA^{-1}}$ and $b = 1.43 \pm 0.03$.

Filter	λ	λF_λ (10^{-12} erg s^{-1} cm^{-2})					Uncertainty (10^{-15} erg s^{-1} cm^{-2})				
	(Å)	0.1″	0.2″	0.3″	0.4″	1.2″	0.1″	0.2″	0.3″	0.4″	1.2″
F140LP	1475	1.196	1.444	1.465	1.433	2.175	8.641	8.548	8.157	7.768	8.320
F165LP	1740	1.333	1.537	1.545	1.508	2.232	2.255	2.211	2.122	2.027	2.164
FR505N	5099	1.623	2.103	2.413	2.646	5.389	6.841	6.947	7.263	7.530	10.206
FR647M	5757	1.559	1.921	2.177	2.362	4.212	6.767	6.620	6.865	7.068	8.974
F606W	5962	1.385	1.858	2.109	2.296	4.137	1.110	1.142	1.184	1.223	1.560

Table 6.2: Flux measurement of all *HST* images. The radii in arcseconds of the circular apertures are shown in the header. The uncertainty presented here is the statistical Poisson noise.

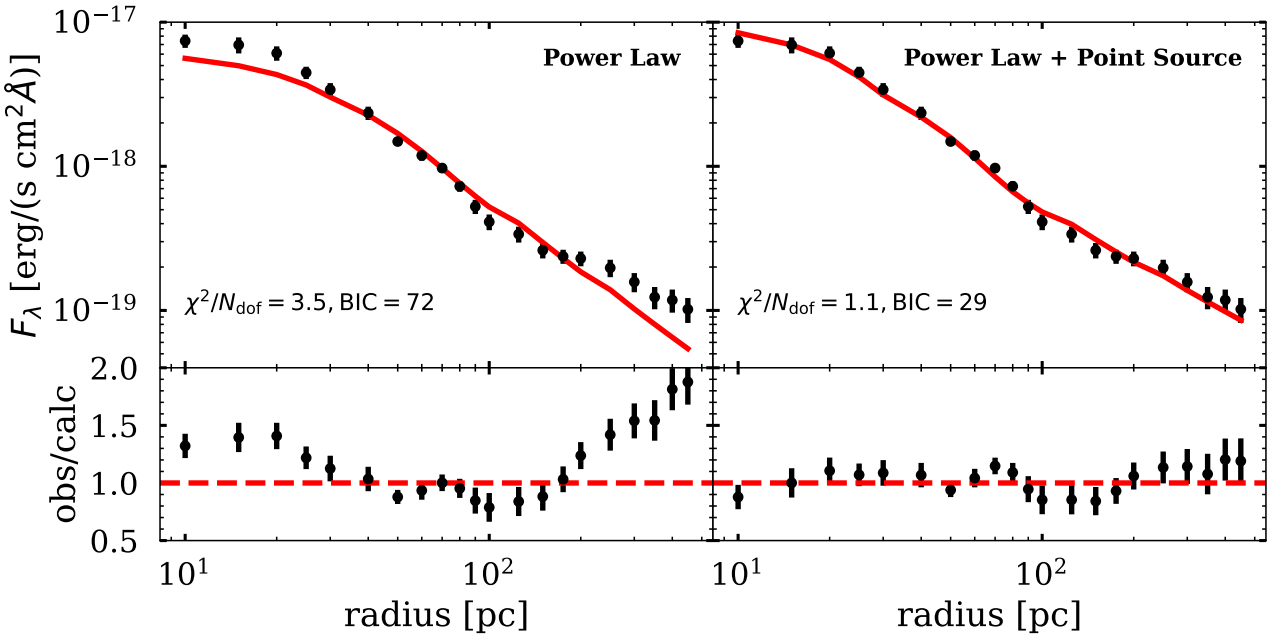

Figure 6.4: Fitting of photometry models to the observed data. Left panel shows the fitting of a power-law-only model, whereas the right panel shows the fitting of a power-law + point-source model. The bottom panels display observed data-to-best-fit model ratios as residuals.

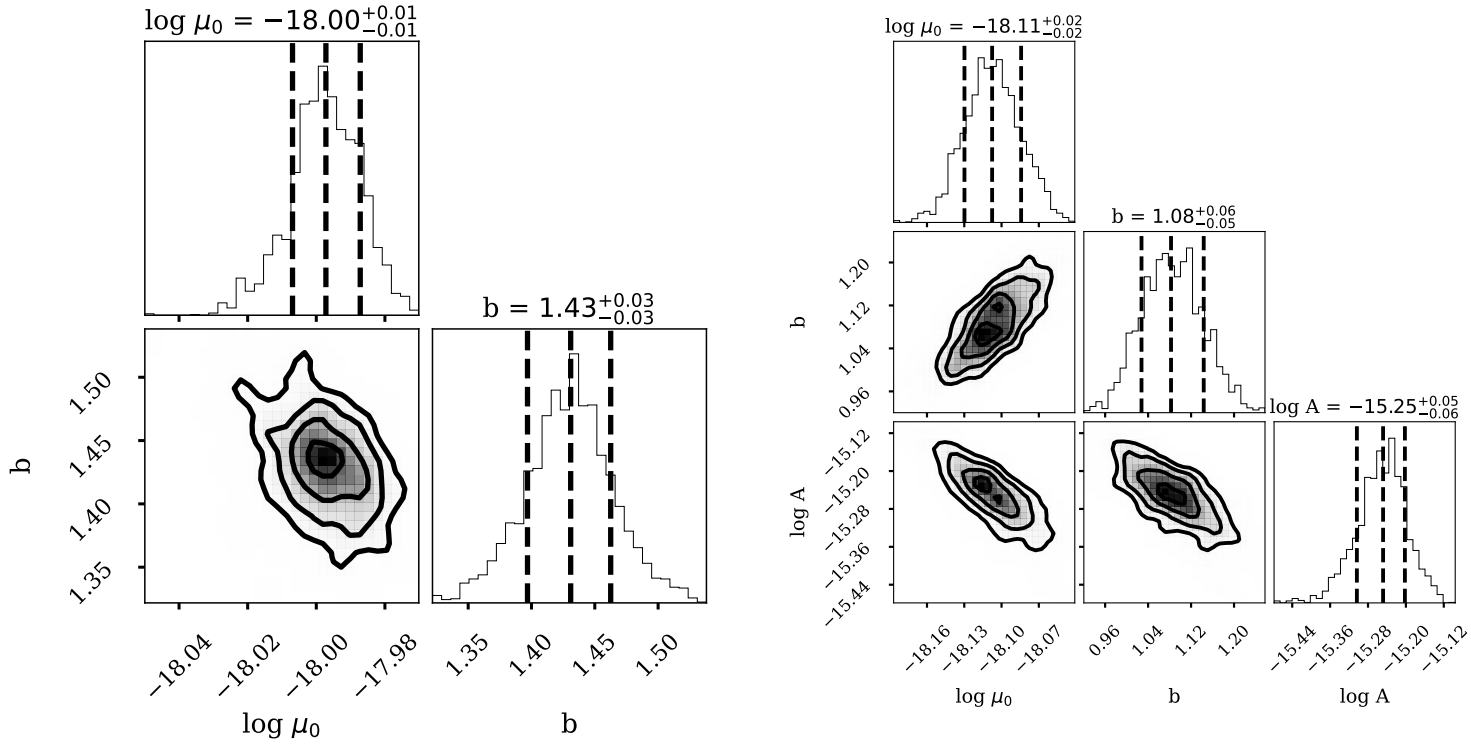

(a) Power law model

(b) Power-law + point-source model

Figure 6.5: Posterior distributions of the parameters that describe the two models fit to the photometry of the continuum-subtracted [O III] image.

6.5 CLOUDY Simulations

We used CLOUDY (Ferland et al. 2017) — a spectral synthesis code designed to simulate the conditions of gas-radiation interactions — to calculate the [O III] line emissivity on a two-dimensional (2D) grid of hydrogen number density and distance from the SMBH, with the goal of constraining the physical properties the [O III] emitting gas. We varied the hydrogen number density $n_{\rm H}$ from $10^3\,{\rm cm^{-3}}$ to $10^{10}\,{\rm cm^{-3}}$, while varying the distance r from 1 pc to 100 pc. Motivated by X-ray observations in the past two decades (see Miniutti et al. 2023a, for a summary), a spectral energy distribution (SED) table was created for a standard multicolour-blackbody accretion-disk model[2] (Shakura & Sunyaev 1973) with two conditions: (i) the X-ray luminosity between 0.2 keV and 2 keV is taken to be $L_{0.2\text{-}2\,{\rm keV}} = 10^{43}\,{\rm erg\,s^{-1}}$ (Miniutti et al. 2023a), and (ii) the temperature at the inner edge of the disk $k_{\rm B}T_{\rm in} = 50\,{\rm eV}$ ($k_{\rm B}$ being the Boltzmann constant; Miniutti et al. 2023a). These numbers reflect the approximate midpoints of the range of $L_{0.2\text{-}2\,{\rm keV}}$ and $k_{\rm B}T_{\rm in}$ observed during the quiescent phase of the QPE system. We chose the noneruptive phase because the system predominantly operates in this state, with the QPE duty cycle in GSN 069 being $\sim 10\%$. Consequently, the time-averaged source luminosity is dominated bolometrically by the quiescent phase. Additionally, emission in the quiescent phase (peaking at $\sim 50\,{\rm eV}$) is more efficient than the eruptive phase ($\gtrsim 100\,{\rm eV}$) at producing O III species within the gas, which is likely to lead to higher ionisation states of oxygen to the detriment of [O III] emission (Draine 2011). The disk SED is assumed to be time-independent, although in reality, the X-ray flux varied by a factor of two above and below the time-averaged value taken in our model. The systematic error introduced by this assumption is minor compared to other sources of uncertainties, as we only aim to provide rough constraints on the [O III]-emitting gas properties using a simple one-zone model. The above SED table was fed into the CLOUDY simulations. The chemical abundance within the gas was chosen to be solar abundance.

Note that there is uncertainty about the exact nature of the X-ray absorbing medium at the redshift of GSN 069, with two possibilities. (1) If the absorbing gas is highly ionised, the intrinsic soft-X-ray luminosity in the quiescent phase is $L_{0.2\text{-}2\,{\rm keV}} \approx 2\times10^{43}\,{\rm erg\,s^{-1}}$ and the hydrogen column density along the line of sight is $N_{\rm H} \approx 7\times10^{21}\,{\rm cm^{-2}}$ (Miniutti

[2]The standard multicolour-blackbody disk SED has the asymptotic behaviour of $\nu L_\nu \propto \nu^{4/3}$ at low frequencies $h\nu \ll k_{\rm B}T_{\rm in}$ (Shakura & Sunyaev 1973). This is only possible if the disk extends to infinity with a constant mass accretion rate at all radii. Lu & Quataert (2023) pointed out that fresh gas may join the disk at a finite radius r_*, which is on the order of the pericentre radius of the stellar orbit if the disk is fed by a star (or the tidal disruption of a star). In this case, the outer regions of the disk at $r > r_*$ do not have a constant mass-accretion rate, and the disk SED steepens to $\nu L_\nu \propto \nu^{12/7}$. The disk also has an outer edge at radius $r_{\rm out}$ due to the finite lifetime in which the disk can viscously spread, and hence the emission at the lowest frequencies has a Rayleigh-Jeans spectrum $\nu L_\nu \propto \nu^3$. For our purpose here, since most ionising photons always come from near the inner edge of the disk, the systematic errors introduced by the uncertainty in the disk SED at low frequencies are minor, so we assume the standard disk SED in our model.

et al. 2023a). (2) If the absorbing medium is neutral, then $L_{0.2\text{-}2\,\mathrm{keV}} \approx 4 \times 10^{42}$ erg s^{-1} and $N_\mathrm{H} \approx 5 \times 10^{20}$ cm^{-2} (Miniutti et al. 2023b; this reflects that neutral gas, having higher opacity, requires a smaller column density to produce a similar X-ray spectral shape). Given the prevailing uncertainty in the X-ray luminosity, we opted for a middle ground approach, setting $L_{0.2-2,\mathrm{keV}} = 10^{43}$erg s^{-1} and $N_\mathrm{H} = 2 \times 10^{21}$ cm^{-2} for our standard Cloudy simulations. As a consistency check, we conducted additional Cloudy simulations using the X-ray luminosities and N_H inferred for both aforementioned possibilities. We observed only minor differences in the constraints derived, with variations about a factor of two compared to the standard case. For the sake of brevity, only the results from the representative standard case are discussed hereafter.

Figure 6.6 displays the volume emissivity of [O III], $j_{[\mathrm{O\,III}]}$ (erg s^{-1} cm^{-3}), on a 2D grid of hydrogen number density (n_H) and distance r from the SMBH. The [O III] line luminosity is given by

$$L_{[\mathrm{O\,III}]}(n_\mathrm{H}, r, f_\mathrm{V}) = (4/3)\pi r^3 f_\mathrm{V} j_{[\mathrm{O\,III}]}, \tag{6.4}$$

where f_V is the volume filling factor of the [O III]-emitting gas. Here, in our simple one-zone model, n_H and r should be understood as the density and distance to the SMBH for the gas that dominates the observed [O III] emission. In reality, the [O III] luminosity is contributed by different emitting regions with different gas densities, and these variations can be captured by an effective volume filling factor. The cyan lines represent the combinations of n_H and r that yield the observed point-source [O III] luminosity of 2.1×10^{40} erg s^{-1}, for three distinct values of f_V. The black vertical lines restrict the physical size of the unresolved nuclear [O III] source. The disk X-ray emission has been active for at least 13 yr (Saxton et al. 2011). During this time, the ionising photons from the accretion disk would have traveled $r_\mathrm{min} = 4$ pc, thus setting the lower limit to the size of the nuclear [O III] emitting region. On the other hand, the unresolved point-source region can be no larger than the FWHM of the *HST* PSF. Consequently, the upper limit for the nuclear [O III] region's size is $r_\mathrm{max} = 35$ pc.

Additional constraints can be derived from the requirement that the gas in the nucleus of GSN 069 is optically thin to optical and soft X-ray emission, otherwise the [O III] line or the QPE flares will not be detected. Taking a conservative limit for the V-band dust extinction $A_\mathrm{V} < 1$ mag, we get a total hydrogen column density $N_\mathrm{H} < 2 \times 10^{21}$ cm^{-2} (see chapter 21.2 of Draine 2011). This allows us to set iso-extinction contours in the n_H–r space as

$$n_\mathrm{H}\, r < 2 \times 10^{21} / f_\mathrm{V}\ \mathrm{cm}^{-2}. \tag{6.5}$$

These contours are shown by the dash-dotted lines. A critical volume filling factor $f_\mathrm{V,crit} = 4 \times 10^{-3}$ was determined such that the corresponding extinction contour and the $L_{[\mathrm{O\,III}]}$ solution intersect the r_max vertical black line. Any solution above the critical iso-extinction contour for $f_\mathrm{V,crit}$ is not viable because the [O III]-emitting gas would be optically thick, which is inconsistent with observations. Thus, $f_\mathrm{V} > 4 \times 10^{-3}$ is ruled out. The unshaded

regions in the $n_{\rm H}$–r space represent the viable combinations of number density and distance to the SMBH for the [O III]-emitting gas.

The total mass of the [O III]-emitting gas is

$$M_{\rm gas} = (4/3)\pi r^3 f_{\rm V} n_{\rm H} m_{\rm H}, \tag{6.6}$$

where $m_{\rm H}$ is the mass of a hydrogen atom. It follows that the minimum mass of the [O III]-emitting region must correspond to the lower-left corner of the allowed region in $n_{\rm H}$–r space — that is, where the $L_{\rm [O\,III]}$ contour for $f_{\rm V,crit}$ intersects the $r_{\rm min}$ bound. We found that the total gas mass within the compact nuclear region is at least $3 \times 10^3\ M_\odot$, a conservative limit since we have excluded diffuse gas that does not contribute significantly to the [O III] luminosity.

We also explored the feasibility of establishing an upper limit for $n_{\rm H}$ by comparing the observed Hα luminosity with the luminosity produced by the Cloudy simulations. Wevers et al. (2022) provide the equivalent width (EW) of the Hα line but not the actual measurement of the Hα flux in a spectrum of GSN 069 acquired with a 0.7″-wide slit. To estimate the Hα flux, we performed photometry on the HST continuum image (FR647M) with a 0.7″ aperture and multiplied it with the EW determined by Wevers et al. (2022). Consequently, we were able to derive Hα luminosity as $L_{\rm H\alpha} \approx 6 \times 10^{40}\,{\rm erg\,s^{-1}}$. Note that 0.7″ corresponds to ~ 300 pc in physical size; thus, the $L_{\rm H\alpha}$ value calculated above should be treated as an upper limit on allowed $L_{\rm H\alpha}$ in Cloudy simulations. Unfortunately, the Hα luminosity imposes comparable constraints on the $n_{\rm H}$–r space as $L_{\rm [O\,III]}$, yielding no new insights. Consequently, we refrain from discussing constraints from Hα emission and X-ray measurements any further. Nevertheless, it is important to note that $n_{\rm H}$ cannot be arbitrarily high. Based on Cloudy calculations, we see that for $n_{\rm H} \gtrsim 10^8\,{\rm cm^{-3}}$, the emissivity of [O III] per unit mass rapidly declines to a constant value owing to collisional deexcitation.

Therefore, the hydrogen number density of the gas in the nucleus is constrained to $2 \times 10^3 < n_{\rm H} \lesssim 10^8\ {\rm cm^{-3}}$, with a volume filling factor $f_{\rm V} < 4 \times 10^{-3}$. These values of $f_{\rm V}$ and $n_{\rm H}$ are characteristic of dense molecular gas, which are gravitationally bound clouds that are often the sites of star formation before the SMBH becomes active (see Table 1.3 of Draine 2011). The onset of accretion onto the SMBH then rapidly ionised the surrounding dense gas. Subsequently, the dense gas will have to contend with two opposing pressure forces: the thermal pressure is $P_{\rm gas} = nkT_{\rm gas}$, whereas the pressure from the accretion disk's radiation field is $P_{\rm rad} = L/4\pi r^2 c$. For the region near $r_{\rm min}$, $P_{\rm gas} \approx 4 \times 10^{-7}\,{\rm g\,cm^{-1}\,s^{-2}}$ (for a typical value of $T_{\rm gas} \approx 10^4$ K) and $P_{\rm rad} \approx 2 \times 10^{-7}\,{\rm g\,cm^{-1}\,s^{-2}}$. Since $P_{\rm gas} \approx P_{\rm rad}$, the dense gas may achieve pressure equilibrium, preventing it from dispersing away (we note that the system is unlikely to be in hydrostatic equilibrium and that the 3D radiation-gas dynamics are much more complicated). Furthermore, even if the gas cloud could expand, it would do so at the speed of sound, $c_{\rm s} = \sqrt{kT_{\rm gas}/m_{\rm p}} \approx 10\,{\rm km\,s^{-1}}$. For a 100 yr-old system (as an example), the gas will only expand by up to 10^{15} cm, which is much smaller than $r_{\rm min}$. We

conclude that the [O III]-emitting gas may originate from dense molecular clouds in the vicinity of the SMBH at distances $\mathcal{O}(10)$ pc.

Note that our Cloudy simulations are conducted under the assumption of steady-state ionisation conditions. The time it takes for recombination of O III → O II and H II → H I are roughly given by

$$t_{\mathrm{rec,O\,III}} \approx 1\,\mathrm{yr}\frac{10^4\,\mathrm{cm}^{-3}}{n_{\mathrm{H}}},\quad t_{\mathrm{rec,H\,II}} \approx 10\,\mathrm{yr}\frac{10^4\,\mathrm{cm}^{-3}}{n_{\mathrm{H}}}, \tag{6.7}$$

respectively (Draine 2011). For permissible values of $n_{\mathrm{H}} > 10^3\,\mathrm{cm}^{-3}$, the recombination timescale for O III is shorter than the estimated duration for which the SMBH has been active (10–100 yr). For all allowed values of n_{H}, the recombination timescale of H II, which controls the availability of free electrons, is also shorter than or comparable to the estimated duration of the SMBH activity. Thus, the steady-state assumption approximately holds.

In order to put another constraint on the line luminosities and to visualise the timescale on which the narrow-line region (NLR) emission in GSN 069 evolves, we conducted another set of Cloudy simulations for $\log n_{\mathrm{H}}/\mathrm{cm}^{-3} = \{2, 3, 4, 5, 6\}$, assuming a fiducial volume filling factor of $f_{\mathrm{V}} = 10^{-4}$. We set the inner radius of the gas to be $r_{\mathrm{in}} = 0.010$ pc and varied the outer radius between $r_{\mathrm{out}} = 5{\times}10^{16}$ cm ≈ 0.016 pc and $r_{\mathrm{out}} = 3{\times}10^{20}$ cm ≈ 100 pc since we are concerned about the integrated light from the entire NLR. The value of r_{in} corresponds to a light-crossing time of 10 days, which is much shorter than the age of the compact nuclear [OIII] source in GSN069. Since most of the narrow-line emission comes from much larger radii $r \gg r_{\mathrm{in}}$, our results are insensitive to the choice of r_{in}. An example of the Cloudy settings is provided in the Appendix. We present the results of these simulations in Figure 6.7. For the NLR evolution on the Baldwin-Phillips-Terlevich (BPT) diagnostic diagram (Baldwin et al. 1981), the starting point is a typical H II-dominated galaxy, which we assume has $L_{\mathrm{H}\alpha} = 3 \times 10^{40}\,\mathrm{erg\,s}^{-1}$, $L_{\mathrm{H}\beta} = 10^{40}\,\mathrm{erg\,s}^{-1}$, $L_{[\mathrm{O\,III}]5007} = 5 \times 10^{39}\,\mathrm{erg\,s}^{-1}$, and $L_{[\mathrm{N\,II}]6583} = 10^{40}\,\mathrm{erg\,s}^{-1}$. All of the line ratios are computed by summing luminosities from both the assumed H II background and the simulated NLR. For the allowed gas densities and volume filling factor, the Strömgren sphere will expand approximately as $r = ct$ — the standard isothermal Strömgren sphere expansion calculation would yield an unphysical superluminal expansion rate. Therefore, different outer radii used in the simulation can be converted into time since the turn-on of the central ionising source. We see that initially the NLR is in the purely star-forming H II region in the BPT diagram, but as the Strömgren sphere expands over time, the NLR moves first to the upper-left corner and then transitions to moving rightward at nearly constant $\log([\mathrm{O\,III}]/\mathrm{H}_\beta)$. Eventually, the NLR settles in the AGN region of the BPT diagram after $\sim$ 30–300 yr depending on the gas density. The evolution is the fastest for higher n_{H}.

In our simulation, we found that the [O III] and [N II] line luminosities increase rapidly with the size of the Strömgren sphere, approximately scaling as $L \propto r^{10}$. Such rapid rise of

[O III] luminosity can also be inferred from Figure 6.6, since [O III] emissivity increases as $j_{[\mathrm{O\,III}]} \propto r^7$ for a constant n_H and it follows from Equation 6.4 that $L_{[\mathrm{O\,III}]} \propto r^{10}$. On the other hand, the luminosities of the Balmer lines H_α and H_β only scale as $\propto r^{3.5}$. The line luminosities remain relatively constant once the Strömgren sphere has expanded to a certain radius determined by the gas number density. This occurs because the emissivity of the lines diminishes significantly beyond this distance from the accretion system, making only a minor contribution to the overall integrated line luminosity. The point at which the line luminosities stabilise marks the transition of the NLR toward the AGN region in the BPT diagram. The implications are discussed in the following section.

Continued Caption for Figure 6.6: The colour bar represents the [O III] emissivity calculated by Cloudy. The cyan-coloured bands represent the contours that satisfy the observed [O III] luminosity of the unresolved point source for various values of the volume filling factors f_V. The solid vertical black lines show constraints on the size of the emitting region. The black dash-dotted lines show iso-extinction contours for various values of f_V. The dash-dotted lines follow this scheme: 2 dots between dashes for $f_\mathrm{V} = 10^{-2}$, 4 dots between dashes for $f_\mathrm{V} = 10^{-4}$, and so on. The iso-extinction contour and the [O III] luminosity solution corresponding to $f_{\mathrm{V,crit}}$ are shown with dashed lines. The disallowed region is hatched with grey lines. The smaller panel on the top extends $\log n_\mathrm{H}$ up to 10 cm^{-3} to demonstrate the decline in [O III] emissivity due to collisional de-excitation at high density.

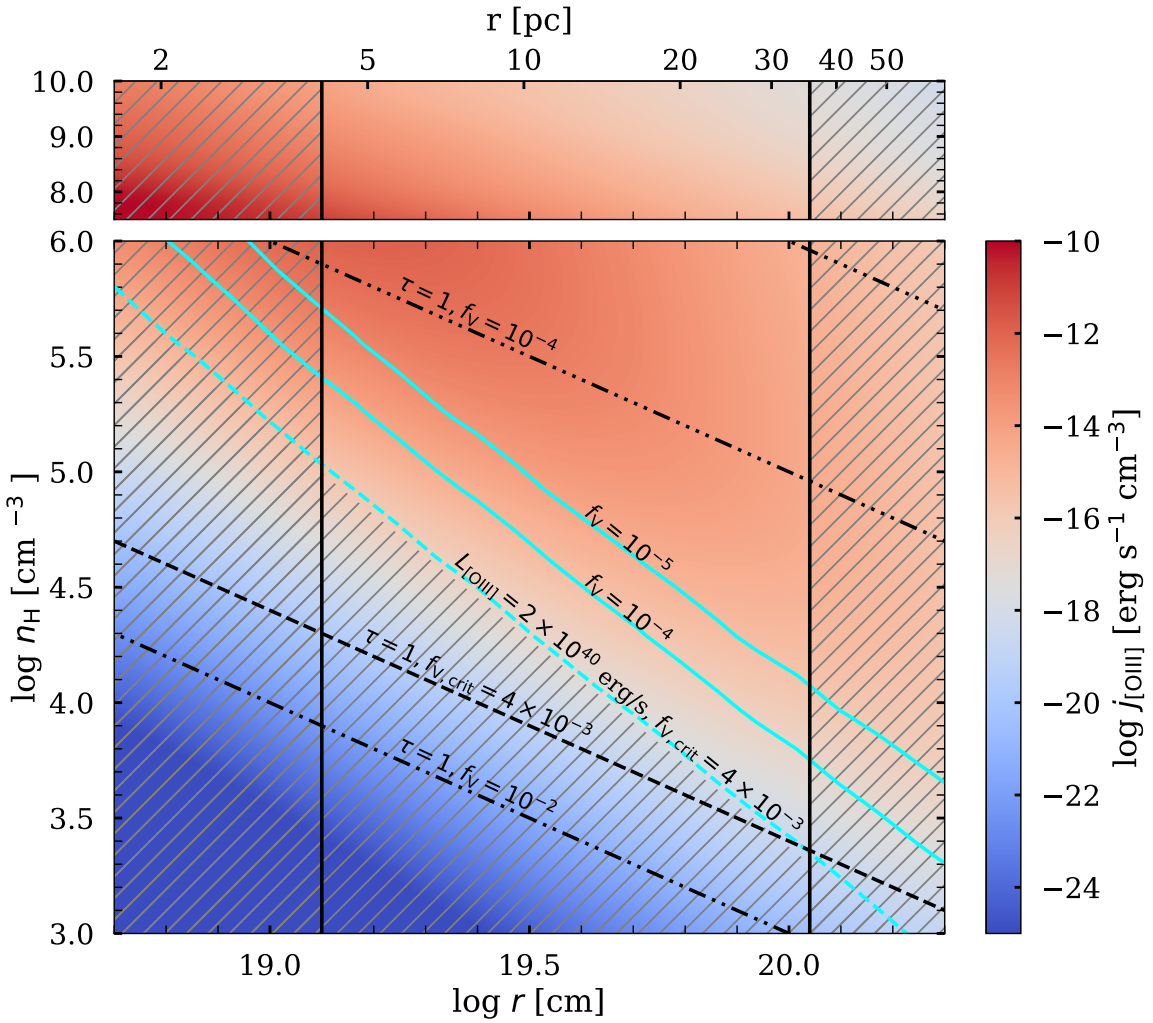

Figure 6.6: Constraints on the hydrogen number density (n_H) and the distance from SMBH of the [O III]-emitting gas in the nucleus of GSN 069. See the continued caption after this figure.

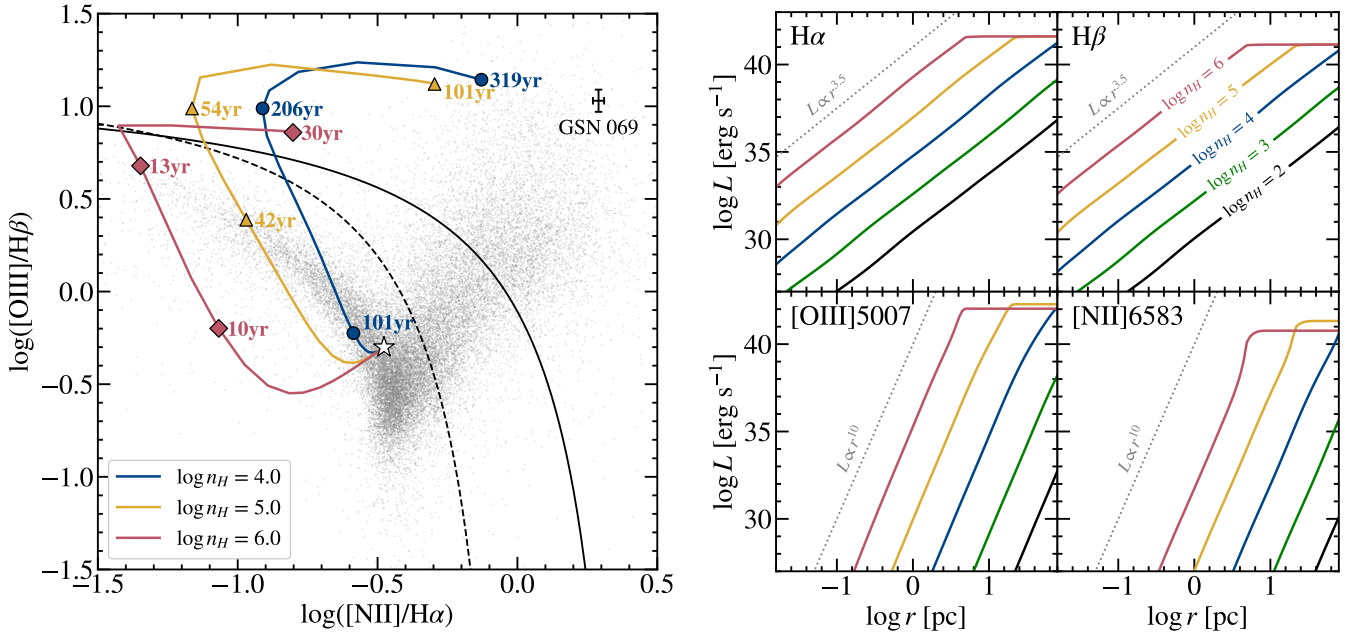

Figure 6.7: Examples of possible NLR evolution via CLOUDY simulations at different gas densities. **Left:** The temporal evolution of the source in a BPT diagram for $n_{\rm H} = 10^4\,{\rm cm}^{-3}$, $n_{\rm H} = 10^5\,{\rm cm}^{-3}$, $n_{\rm H} = 10^6\,{\rm cm}^{-3}$. The white star marks the initial background line ratios from the assumed star-forming galaxy. We do not include the lower-density tracks because the total line luminosities are still dominated by the star-forming H II regions at $\sim 100\,{\rm pc}$. The grey points are galaxies from the MPA-JHU DR7 catalogue (see Data Availability statement). The position of GSN 069 as determined by Wevers et al. (2022) based on line fluxes from the entire galaxy (dominated by the non-nuclear regions) is also shown. **Right:** The line luminosity of selected optical lines as a function of the outer radius set in CLOUDY. As discussed in the text, the radius is equivalent to time since the accretion system turned on ($t = r/c$).

6.6 Discussion and Prediction for Future Observations

One potential concern with extracting an unresolved nuclear point source of [O III] emission is the shape of the spectral continuum. We evaluated the robustness of our point-source detection using an optical spectrum[3] (1″-wide slit; Agís González et al. in prep.) of GSN 069 to estimate the spectral continuum shape. The correction required a modest upscaling of the continuum band by $\sim 7\%$. This scaling is commensurate with the rough upper limit that can be estimated from the fluxes measured in FR647M and F606W provided in Table 6.2. With the flux in the smallest aperture (0.1″), we find that the scaling factor must be $< 12\%$. Scaling the continuum band by $\sim 10\%$ only marginally weakened the statistical significance of the point-source extraction, and the calculated [O III] luminosity of the point source remained within the current uncertainty margins. The limitation of using a wide-slit spectrum for continuum-shape correction is that it predominantly captures light from areas outside the unresolved nucleus, potentially leading to an unrepresentative correction for the innermost nuclear region, especially if the continuum shape changes with distance from the centre. Future spectra obtained with integral field units (IFUs) will be able to determine the continuum-shape correction more accurately. Given the current uncertainties in determining the spectral continuum shape, we do not scale the continuum band in the analysis presented here, and demonstrate that small scaling of the continuum band does not materially impact our findings.

Past X-ray observations show that the SMBH in GSN 069 has been active for at least 13 yr. An upper limit to the age of the accretion disk may be obtained from the following two arguments. First, the upper limit on the nuclear [O III] emission size is 35 pc, which corresponds to a light-travel time of 115 yr. A potential loophole in accepting this value as the upper limit to the age is that the size of the nuclear [O III] emitting region might simply be due to a high concentration of dense gas within 35 pc. Second, in most QPE models (referred to in § I), the system is powered by a stellar-mass object orbiting an SMBH. Taking a radiative efficiency of $\eta \approx 0.1$, a mass budget of $M \approx 1\,M_\odot$, and an average bolometric luminosity of $L \approx 2 \times 10^{43}\,\mathrm{erg\,s^{-1}}$, we infer the lifetime of the system to be

$$t_{\rm life} \approx \frac{\eta M c^2}{L} \approx 200\,\mathrm{yr}\,\frac{(\eta/0.1)\,(M/M_\odot)}{L/2\times10^{43}\,\mathrm{erg\,s^{-1}}}. \tag{6.8}$$

From these two arguments, we infer that the current age of the system is likely less than $O(10^2)$ yr. It is worth noting that *ROSAT* nondetection of bright X-ray emission in 1994 could mean that the SMBH is active for no more than ~ 30 yr.

We also consider the possibility that a star-forming region within the nucleus could dominate as the source of the ionising radiation over the accretion disk. This argument can be refuted for the following reason. Let us consider an optimistic case of a young nuclear

[3]The spectrum is shown in the Appendix.

star cluster of mass $10^6\,M_\odot$ (a higher stellar mass will overproduce the far-UV fluxes in the nuclear region; see Table 6.2). Employing the Salpeter initial mass function (Salpeter 1955) results in an estimation of $\sim 10^4$ high-mass stars ($M \gtrsim 15\,M_\odot$). Each high-mass star emits $O(10^{48})$ ionising photons ($h\nu > 13.6\,\mathrm{eV}$) per second (see Table 15.1 of Draine 2011), resulting in emission of $O(10^{52})$ ionising photons per second from the nuclear star cluster. In fact, the optimistic case of a young massive cluster we are considering here is too blue to be consistent with the observed far-UV to optical colour, which has a nearly flat SED with $\lambda F_\lambda \propto \lambda^{\approx 0}$ indicating an older stellar population with far fewer ionising photons. Comparatively, the accretion-disk SED model that is consistent with the X-ray observations (Miniutti et al. 2023a) produces roughly $O(10^{53})$ ionising photons every second. Thus, the budget of ionising photons is dominated by the accretion disk and not the nuclear stellar cluster. This rules out the scenario wherein the nuclear [O III] emission is powered by a nuclear star cluster.

6.6.1 Extended [O III] emission region

In Figure 6.2, we see an extended [O III] emission region, stretching up to 1 kpc away from the nucleus. This large-scale [O III] emission's origin could be linked to a previous phase of (or currently weak) AGN activity. Then, sometime within the last 10–100 yr GSN 069 began emitting bright X-ray emission associated with the initial X-ray-selected TDE and subsequent QPEs. Indeed, Wevers et al. (2022) have shown that, based on line fluxes from the entire galaxy, the ionising source in GSN 069 is consistent with an AGN. Although the position of GSN 069 is marked in Figure 6.7, we note that line fluxes measured from long-slit spectra — dominated by flux from non-nuclear regions — might not accurately reflect the nuclear region's line fluxes.

The presence of a relic or currently weak AGN in GSN 069 is further supported by similar narrow-band imaging of persistent AGNs that has shown extended [O III] emission reaching several tens of kpc from the nucleus (e.g., Sun et al. 2018). To our knowledge, while no compact nuclear [O III] emission regions have been reported in AGNs, this could merely be due to the lack of targeted searches. The [O III] surface brightness in these AGN hosts declines following a power law (Liu et al. 2013), similar to what is observed in GSN 069. Additionally, the [O III]-emitting gas in these AGNs is characterised as clumpy (Greene et al. 2011) with a low volume filling factor ($f_V \approx 10^{-6}$; Nesvadba et al. 2006), also consistent with our findings. A discovered correlation between the size of the [O III]-emitting area and the AGN's luminosity suggests that more-luminous AGNs can ionise gas further into their host galaxy (Sun et al. 2018). The relatively small size of the [O III]-emitting region in GSN 069, compared to persistent AGNs, thus implies a very low-luminosity historical AGN in GSN 069 ($\lesssim 10^{42}$ erg s^{-1}, if the size-luminosity relationship is naively extrapolated to 1 kpc; Sun et al. 2018).

Moreover, extended [O III] emission-line filaments have been observed in galaxies hosting TDEs (e.g., ASASSN-14li; Prieto et al. 2016), suggesting that these galaxies might have experienced recent mergers. Such events could leave behind relatively dense gas over large scales. In GSN 069, the [O III] filamentary extensions point toward a recent merger possibly triggering a significant starburst, leading to AGN activity and an enhanced rate of TDEs (Arcavi et al. 2014; French et al. 2016). The filamentary structures observed in both ASASSN-14li and GSN 069 contribute to the accumulating evidence of a link between QPEs and TDEs.

6.6.2 Testable predictions for future observations

Our model of an SMBH accretion disk that was recently activated by a sudden onset of gas supply in the past 10–100 yr is consistent with all observations. To further test this picture, we consider the possible future evolution of the system. For simplicity, let us assume that the disk luminosity and SED stays more-or-less steady in the next few years. Based on the relatively modest Hα luminosity from the compact nuclear region ($\ll 6 \times 10^{40}\,\mathrm{erg\,s^{-1}}$) and also the fact that soft X-rays are escaping from the system, we know that only a small fraction of the ionising, soft-X-ray photons from the accretion disk is used to power the compact nuclear [O III] region. Therefore, we expect that Strömgren sphere surrounding the SMBH to expand at the speed of light, $\mathrm{d}r/\mathrm{d}t = c$. From Figure 6.7, it is clear that two distinct regimes exist for the evolution of [O III] luminosity. If the QPE is sufficiently young (i.e., before the luminosity flattens out), then we expect the [O III] luminosity to increase rapidly as $L \propto r^{10}$, with a fractional change given, to an order of magnitude, by

$$\frac{\mathrm{d}L_{[\mathrm{O\,III}]}}{L_{[\mathrm{O\,III}]}} \approx \frac{10\,\mathrm{d}r}{r} \approx \frac{10\,\mathrm{d}t}{t}. \tag{6.9}$$

For a fixed time interval $\mathrm{d}t$, we see that the [O III] luminosity will be less variable if the source is older. For instance, for $t \approx 30$ yr and $\mathrm{d}t = 6$ yr (for an observation taken in the near future), we expect a 200% increase in the [O III] luminosity from the compact nuclear region. Such a large increase in the nuclear [O III] luminosity will be easily detectable by *HST*, and may also be observable with ground-based spectroscopic observations at low spatial resolutions, with the caveat that the measured line flux may be dominated by the extended [O III] region. Our power-law + point-source model shows that surface flux density declines with a rather shallow power law, $\mu(r) \propto r^{-1}$. It follows that the flux density enclosed within some radius r scales as $F_\lambda(< r) \approx r^2\mu(r) \propto r$. This means that the unresolved [O III] region contributes only a small fraction of the total [O III] luminosity measured by ground-based observatories employing wider slits. For a 0.7″-wide slit, the compact nuclear region only contributes $\sim$ 10% of the [O III] luminosity. Thus, a 200% increase in the [O III] luminosity from the NLR will translate to only a 25% increase in total integrated

flux, which may still be detectable by low-spatial-resolution spectroscopy.

The other regime is where the Strömgren sphere has expanded beyond the point where the [O III] line luminosity levels off. In this situation, we will not observe any significant changes in the [O III] line's brightness. If this happens, we should also notice that the NLR has settled within the AGN region on the BPT diagram. In this case, the age of the QPE is degenerate with the gas number density ($n_{\rm H}$), but we can place even stronger constraints on both of these quantities. These arguments strongly support the idea of conducting similar *HST* observations, like the ones presented in this study, in the coming years to refine our understanding of the age of the SMBH accretion system in GSN 069. Integral-field-unit spectra of GSN 069 and its nucleus would be even more valuable in this context.

6.7 Conclusion

This paper presents an analysis of archival *HST* images, targeting the narrow-line [O III] emission within the QPE discovery source, GSN 069. With aperture photometry on the continuum-subtracted [O III] image, we find strong evidence for the presence of a compact, unresolved nuclear [O III] emission region, which is overlaid on top of a spatially extended [O III] emission region reaching as far as 1 kpc away from the nucleus. The extended [O III] emission is not associated with star-forming H II regions, making it likely that the extended emission is due to past or currently weak AGN activity instead of ionisation by hot stars. Similar extended [O III] filaments seen in TDE-hosts strengthen the connection between QPEs and TDEs.

We measured the [O III] luminosity of the compact region, yielding a value of $(2.1 \pm 0.3) \times 10^{40}\,{\rm erg\,s^{-1}}$. Using Cloudy simulations, we constrain the physical properties of the [O III]-emitting gas in the compact region, and our findings are summarised as follows:

1. size of emitting region $4\,{\rm pc} < r < 35\,{\rm pc}$,
2. age of the SMBH accretion system $10 \lesssim t \lesssim 100\,{\rm yr}$,
3. gas number density $2 \times 10^3 < n_{\rm H} \lesssim 10^8\,{\rm cm^{-3}}$,
4. volume filling factor $f_{\rm V} < 4 \times 10^{-3}$, and
5. mass of the emitting gas $M_{\rm gas} > 3 \times 10^3\,M_\odot$.

These constraints lead us to conclude that the [O III] emission in the compact region comes from dense gas that likely originates from dense molecular clouds within the nuclear region. Such molecular clouds also exist at the Galactic Centre of our Milky Way Galaxy. Compared to other known AGNs whose long-lasting radiation pressure has largely modified its gaseous environment, the nucleus of GSN 069 is a unique, young (most likely 10

to 100 yr-old) ionising source that allows us to probe the pristine gas environment near the otherwise inactive SMBH. This likely applies to other QPE sources as well. Finally, based on our current understanding, we predict that the [O III] luminosity from the compact region will likely undergo a $\sim$ 200% change in a time interval of a few years if the QPE is young. If the line luminosity increases, we should also see that the NLR lies in the H II region of the BPT diagram. On the other hand, if the QPE is older (or the gas in the NLR is denser), we will not see any change in [O III] line luminosity. In this case, the NLR will be found in the AGN region of the BPT diagram.This strongly motivates another epoch of *HST* observations similar to the ones presented here in the near future, which will further pin down the age of the SMBH accreting system.

Acknowledgements

Research by K.C.P. is funded in part by generous support from Sunil Nagaraj, Landon Noll, and Sandy Otellini. We acknowledge the support from the Rose Hills Innovator Program. G.M. was supported by grant PID2020-115325GB-C31 funded by MICIN/AEI/10.13039/501100011033. A.V.F. is grateful for support from the Christopher R. Redlich Fund and numerous other donors. This research benefited from interactions at workshops funded by the Gordon and Betty Moore Foundation through grant GBMF5076.

Data Availability

The *HST* images used in this work are publicly available on STScI's MAST. The MPA-JHU DR7 catalogue used to create Figure 6.7 can be found at https://wwwmpa.mpa-garching.mpg.de/SDSS/.

Appendix

An example of the CLOUDY input settings used to create Figure 6.6 is shown below for reference.

```
luminosity total 43.3
table SED "disk.sed"
radius 18.70
hden 2.48
abundances "default.abn" no grains
iterate to converge
print last iteration
```

```
stop thickness 11.00
save lines, emissivity, "R18.7nH2.48.lem" last
blnd 5007.00A
h 1 6562.80A
h 1 4861.33A
end of lines
```

Below we provide an example of the CLOUDY settings used to create Figure 6.7:

```
luminosity total 43.3
table SED "shortdisksed.sed"
filling factor 0.0001
radius 16.50 19.75
hden 3.00
abundances "default.abn" no grains
iterate to converge
print last iteration
save lines, list"R19.75nH3.0fV1e-4.lines"
     "LineList_NLR.dat"
     units Angstrom
     absolute last
save lines, emissivity"R19.75nH3.0fV1e-4.lem"
     units Angstrom last
o 3 5006.84A
blnd 5007.00A
h 1 6562.80A
h 1 4861.33A
n 2 6583.45A
s 2 6716.44A
s 2 6730.82A
o 1 6300.30A
end of lines
save overview "GSN069_R16.7nH3.0fV1e-4.ovr" last
save continuum "GSN069_R16.7nH3.0fV1e-4.con"
     units Angstrom last
```

The optical spectrum of GSN 069 used to estimate the spectral continuum shape is provided in Figure 6.8 below.

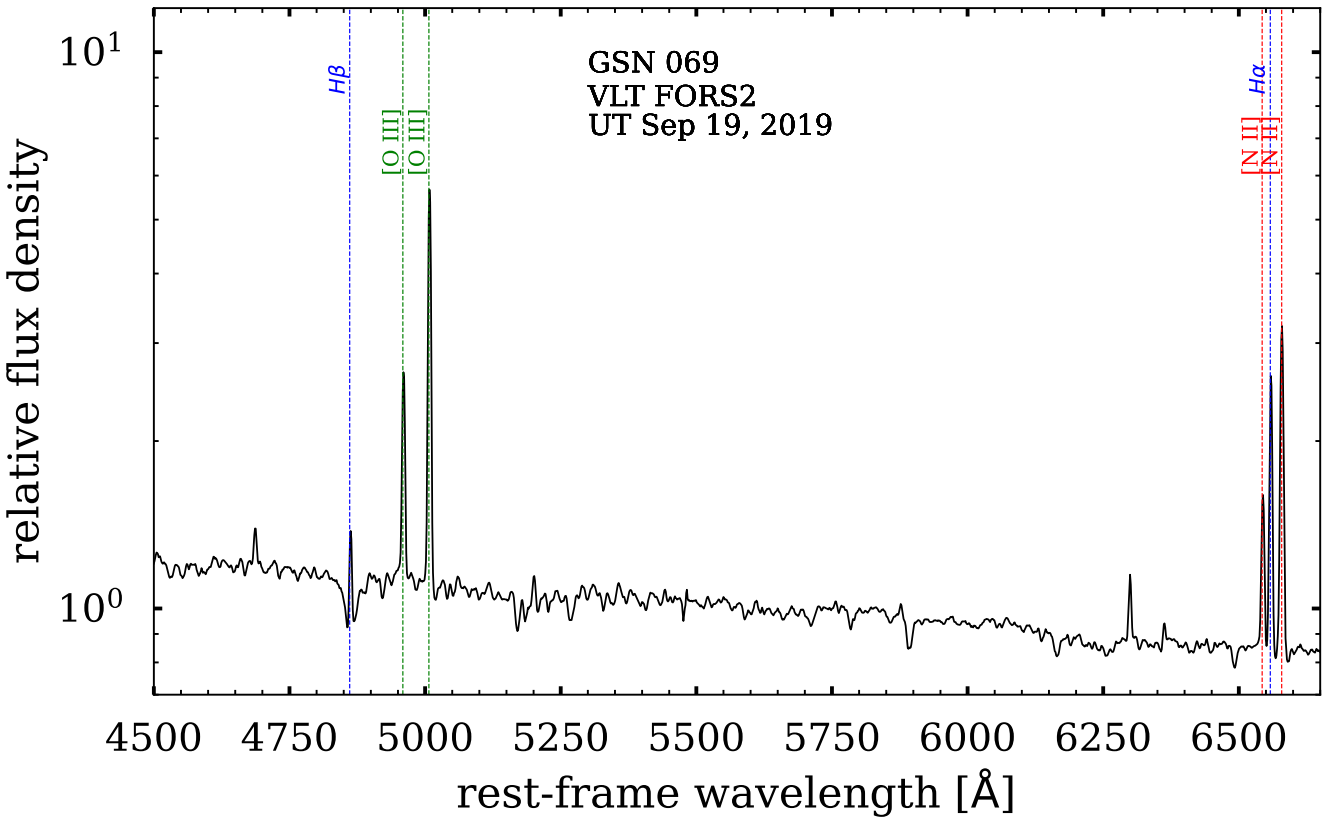

Figure 6.8: The optical spectrum of GSN 069 was obtained on Sep. 19, 2019 UTC, using the FORS2 instrument on the 8.2 m Very Large Telescope. The slit width and the extraction window were 1″ and 1.25″, respectively, which corresponds to $\sim 0.4 \times 0.5$ kpc in physical size.

Bibliography

Arcavi, I., Gal-Yam, A., Sullivan, M., et al. 2014, ApJ, 793, 38
Arcodia, R., Merloni, A., Nandra, K., et al. 2021, Nature, 592, 704
Arcodia, R., Miniutti, G., Ponti, G., et al. 2022, A&A, 662, A49
Arcodia, R., Liu, Z., Merloni, A., et al. 2024, arXiv e-prints, arXiv:2401.17275
Arnett, W. D. 1969, AP&SS, 5, 180
Arnold, D. M., Steele, I. A., Bates, S. D., Mottram, C. J., & Smith, R. J. 2012, in Society of Photo-Optical Instrumentation Engineers (SPIE) Conference Series, Vol. 8446, Ground-based and Airborne Instrumentation for Astronomy IV, ed. I. S. McLean, S. K. Ramsay, & H. Takami, 84462J
Astropy Collaboration, Price-Whelan, A. M., Lim, P. L., et al. 2022, ApJ, 935, 167
Auchettl, K., Ramirez-Ruiz, E., & Guillochon, J. 2018, ApJ, 852, 37
Baldwin, J. A., Phillips, M. M., & Terlevich, R. 1981, PASP, 93, 5
Bellm, E. C., Kulkarni, S. R., Graham, M. J., et al. 2019, PASP, 131, 018002
Benz, W., Bowers, R. L., Cameron, A. G. W., & Press, W. H. . 1990, ApJ, 348, 647
Bildsten, L., Shen, K. J., Weinberg, N. N., & Nelemans, G. 2007, ApJL, 662, L95
Blagorodnova, N., Cenko, S. B., Kulkarni, S. R., et al. 2019, ApJ, 873, 92
Bloom, J. S., Giannios, D., Metzger, B. D., et al. 2011, Science, 333, 203
Bonnerot, C., Lu, W., & Hopkins, P. F. 2021, MNRAS, 504, 4885
Bulla, M., Sim, S. A., & Kromer, M. 2015, MNRAS, 450, 967
Bulla, M., Sim, S. A., Pakmor, R., et al. 2016a, MNRAS, 455, 1060
Bulla, M., Sim, S. A., Kromer, M., et al. 2016b, MNRAS, 462, 1039
Chakraborty, J., Kara, E., Masterson, M., et al. 2021, ApJ, 921, L40
Chakraborty, J., Arcodia, R., Kara, E., et al. 2024, arXiv e-prints, arXiv:2402.08722
Chen, X., Qiu, Y., Li, S., & Liu, F. K. 2022, ApJ, 930, 122
Cikota, A., Patat, F., Wang, L., et al. 2019, MNRAS, 490, 578
Ciotti, L., D'Ercole, A., Pellegrini, S., & Renzini, A. 1991, ApJ, 376, 380
Coughlin, E. R., & Begelman, M. C. 2014, ApJ, 781, 82
Dai, L., McKinney, J. C., Roth, N., Ramirez-Ruiz, E., & Miller, M. C. 2018, ApJ, 859, L20
Draine, B. T. 2011, Physics of the Interstellar and Intergalactic Medium
Esquej, P., Saxton, R. D., Komossa, S., et al. 2008, A&A, 489, 543

Ferland, G. J., Chatzikos, M., Guzmán, F., et al. 2017, Rev. Mexicana Astron. Astrofis., 53, 385
Fesen, R. A., Höflich, P. A., Hamilton, A. J. S., et al. 2007, ApJ, 658, 396
Filippenko, A. V. 1982, PASP, 94, 715
—. 1997, ARAA, 35, 309
Filippenko, A. V., Li, W. D., Treffers, R. R., & Modjaz, M. 2001, in Astronomical Society of the Pacific Conference Series, Vol. 246, IAU Colloq. 183: Small Telescope Astronomy on Global Scales, ed. B. Paczynski, W.-P. Chen, & C. Lemme, 121
Fink, M., Röpke, F. K., Hillebrandt, W., et al. 2010, A&A, 514, A53
Forster, F. 2019, Transient Name Server Discovery Report, 2019-1857, 1
Franchini, A., Bonetti, M., Lupi, A., et al. 2023, A&A, 675, A100
French, K. D., Arcavi, I., & Zabludoff, A. 2016, ApJ, 818, L21
Gaia Collaboration, Brown, A. G. A., Vallenari, A., et al. 2018, A&A, 616, A1
Gal-Yam, A. 2017, Observational and Physical Classification of Supernovae, ed. A. W. Alsabti & P. Murdin, 195
Gal-Yam, A., Arcavi, I., Ofek, E. O., et al. 2014, Nature, 509, 471
Gamezo, V. N., Khokhlov, A. M., & Oran, E. S. 2004, Physical Review Letters, 92, 211102
García-Berro, E., Badenes, C., Aznar-Siguán, G., & Lorén-Aguilar, P. 2017, MNRAS, 468, 4815
García-Berro, E., & Lorén-Aguilar, P. 2017, Dynamical Mergers, ed. A. W. Alsabti & P. Murdin, 1237
Gezari, S., Basa, S., Martin, D. C., et al. 2008, ApJ, 676, 944
Gezari, S., Chornock, R., Rest, A., et al. 2012, Nature, 485, 217
Giustini, M., Miniutti, G., & Saxton, R. D. 2020, A&A, 636, L2
Goodrich, R. W., Cohen, M. H., & Putney, A. 1995, PASP, 107, 179
Greene, J. E., Zakamska, N. L., Ho, L. C., & Barth, A. J. 2011, ApJ, 732, 9
Guillochon, J., Manukian, H., & Ramirez-Ruiz, E. 2014, ApJ, 783, 23
Guolo, M., Pasham, D. R., Zajaček, M., et al. 2024, Nature Astronomy, arXiv:2309.03011 [astro-ph.HE]
Hayden, B. T., Garnavich, P. M., Kasen, D., et al. 2010, ApJ, 722, 1691
Higgins, A. B., Wiersema, K., Covino, S., et al. 2019, MNRAS, 482, 5023
Hillebrandt, W., Kromer, M., Röpke, F. K., & Ruiter, A. J. 2013, Frontiers of Physics, 8, 116
Hills, J. G. 1975, Nature, 254, 295
Hinkle, J. T., Holoien, T. W. S., Auchettl, K., et al. 2021, MNRAS, 500, 1673
Höflich, P. 1991, A&A, 246, 481
—. 1995, ApJ, 443, 89
—. 2017, Explosion Physics of Thermonuclear Supernovae and Their Signatures, ed. A. W. Alsabti & P. Murdin, 1151

Höflich, P., Gerardy, C. L., Marion, H., & Quimby, R. 2006, New Astronomy Review, 50, 470
Höflich, P., & Khokhlov, A. 1996, ApJ, 457, 500
Höflich, P., Mueller, E., & Khokhlov, A. 1993, A&A, 268, 570
Höflich, P., Wheeler, J. C., Hines, D. C., & Trammell, S. R. 1996, ApJ, 459, 307
Höflich, P., Wheeler, J. C., & Thielemann, F. K. 1998, ApJ, 495, 617
Höflich, P., Hsiao, E. Y., Ashall, C., et al. 2017, ApJ, 846, 58
Holoien, T. W. S., Kochanek, C. S., Prieto, J. L., et al. 2016a, MNRAS, 455, 2918
—. 2016b, MNRAS, 455, 2918
Holoien, T. W. S., Auchettl, K., Tucker, M. A., et al. 2020, ApJ, 898, 161
Horne, K. 1986, PASP, 98, 609
Howell, D. A. 2011, Nature Communications, 2, 350
Howell, D. A., Höflich, P., Wang, L., & Wheeler, J. C. 2001, ApJ, 556, 302
Hoyle, F., & Fowler, W. A. 1960, ApJ, 132, 565
Hung, T., Foley, R. J., Ramirez-Ruiz, E., et al. 2020, ApJ, 903, 31
Hung, T., Foley, R. J., Veilleux, S., et al. 2021, ApJ, 917, 9
Iben, Jr., I., & Tutukov, A. V. 1984, ApJs, 54, 335
Jermak, H. 2017, PhD thesis, Astrophysics Research Institute, Liverpool John Moores University
Jiang, Y.-F., Guillochon, J., & Loeb, A. 2016, ApJ, 830, 125
Kasen, D., & Plewa, T. 2007, ApJ, 662, 459
Kasen, D., Röpke, F. K., & Woosley, S. E. 2009, Nature, 460, 869
Kasen, D., Thomas, R. C., & Nugent, P. 2006, ApJ, 651, 366
Katz, M. P., Zingale, M., Calder, A. C., et al. 2016, ApJ, 819, 94
Kaur, K., Stone, N. C., & Gilbaum, S. 2023, MNRAS, 524, 1269
Kawabata, M., Maeda, K., Yamanaka, M., et al. 2020, ApJ, 893, 143
Khokhlov, A. M. 1991, A&A, 245, 114
King, A. 2020, MNRAS, 493, L120
—. 2022, MNRAS, 515, 4344
Komossa, S., & Bade, N. 1999, A&A, 343, 775
Krolik, J. H., & Linial, I. 2022, ApJ, 941, 24
Kromer, M., Sim, S. A., Fink, M., et al. 2010, ApJ, 719, 1067
Kushnir, D., Katz, B., Dong, S., Livne, E., & Fernández, R. 2013, ApJL, 778, L37
Lee, C.-H., Hung, T., Matheson, T., et al. 2020, ApJ, 892, L1
Leloudas, G., Dai, L., Arcavi, I., et al. 2019, ApJ, 887, 218
Leloudas, G., Bulla, M., Cikota, A., et al. 2022, Nature Astronomy, 6, 1193
Leonard, D. C., Filippenko, A. V., Chornock, R., & Li, W. 2002, AJ, 124, 2506
Leonard, D. C., Li, W., Filippenko, A. V., Foley, R. J., & Chornock, R. 2005, ApJ, 632, 450

Linial, I., & Metzger, B. D. 2023, arXiv e-prints, arXiv:2303.16231
Linial, I., & Sari, R. 2023, ApJ, 945, 86
Liodakis, I., Koljonen, K. I. I., Blinov, D., et al. 2023, Science, 380, 656
Liu, G., Zakamska, N. L., Greene, J. E., Nesvadba, N. P. H., & Liu, X. 2013, MNRAS, 430, 2327
Liu, Z.-W., Röpke, F. K., & Han, Z. 2023, Research in Astronomy and Astrophysics, 23, 082001
Livne, E. 1990, ApJL, 354, L53
—. 1999, ApJL, 527, L97
Lodato, G., & Rossi, E. M. 2011, MNRAS, 410, 359
Loeb, A., & Ulmer, A. 1997, ApJ, 489, 573
Lu, W., & Bonnerot, C. 2020, MNRAS, 492, 686
Lu, W., & Quataert, E. 2023, MNRAS, 524, 6247
Luminet, J. P., & Pichon, B. 1989, A&A, 209, 103
Ma, B., Wei, P., Shang, Z., Wang, L., & Wang, X. 2014, The Astronomer's Telegram, 5794
Maoz, D., Mannucci, F., & Nelemans, G. 2014, ARAA, 52, 107
Maund, J. R., Höflich, P., Patat, F., et al. 2010, ApJL, 725, L167
Maund, J. R., Spyromilio, J., Höflich, P. A., et al. 2013, MNRaS, 433, L20
Maund, J. R., Yang, Y., Steele, I. A., et al. 2021, MNRAS, 503, 312
Metzger, B. D., & Stone, N. C. 2016, MNRAS, 461, 948
Metzger, B. D., Stone, N. C., & Gilbaum, S. 2022, ApJ, 926, 101
Miller, J. S., Robinson, L. B., & Goodrich, R. W. 1988, in Instrumentation for Ground-Based Optical Astronomy, 157
Miller, M. C. 2015, ApJ, 805, 83
Miniutti, G., Giustini, M., Arcodia, R., et al. 2023a, A&A, 674, L1
—. 2023b, A&A, 670, A93
Miniutti, G., Saxton, R. D., Rodríguez-Pascual, P. M., et al. 2013, MNRAS, 433, 1764
Miniutti, G., Saxton, R. D., Giustini, M., et al. 2019, Nature, 573, 381
Moll, R., Raskin, C., Kasen, D., & Woosley, S. E. 2014, ApJ, 785, 105
Montier, L., Plaszczynski, S., Levrier, F., et al. 2015, A&A, 574, A135
Nesvadba, N. P. H., Lehnert, M. D., Eisenhauer, F., et al. 2006, ApJ, 650, 693
Nicholl, M., Wevers, T., Oates, S. R., et al. 2020, MNRAS, 499, 482
Niemeyer, J. C., Hillebrandt, W., & Woosley, S. E. 1996, ApJ, 471, 903
Nomoto, K. 1982a, ApJ, 257, 780
—. 1982b, ApJ, 253, 798
Nomoto, K., Sugimoto, D., & Neo, S. 1976, APSS, 39, L37
Nomoto, K., Thielemann, F.-K., & Yokoi, K. 1984, ApJ, 286, 644
Nugent, P., Baron, E., Branch, D., Fisher, A., & Hauschildt, P. H. 1997, ApJ, 485, 812
Nugent, P. E., Sullivan, M., Cenko, S. B., et al. 2011, Nature, 480, 344

Oke, J. B., Cohen, J. G., Carr, M., et al. 1995, PASP, 107, 375
Pakmor, R., Hachinger, S., Röpke, F. K., & Hillebrandt, W. 2011, A&A, 528, A117
Pakmor, R., Kromer, M., Röpke, F. K., et al. 2010, Nature, 463, 61
Pakmor, R., Kromer, M., Taubenberger, S., et al. 2012, ApJL, 747, L10
Pan, X., Li, S.-L., & Cao, X. 2023, ApJ, 952, 32
Pan, X., Li, S.-L., Cao, X., Miniutti, G., & Gu, M. 2022, ApJ, 928, L18
Patat, F., Baade, D., Höflich, P., et al. 2009, A&A, 508, 229
Patra, K. C., Lu, W., Brink, T. G., et al. 2022a, MNRAS, 515, 138
Patra, K. C., Winn, J. N., Holman, M. J., et al. 2020, AJ, 159, 150
Patra, K. C., Yang, Y., Brink, T. G., et al. 2022b, MNRAS, 509, 4058
Pellegrino, C., Howell, D. A., Sarbadhicary, S. K., et al. 2020, ApJ, 897, 159
Perlmutter, S., Aldering, G., Goldhaber, G., et al. 1999, ApJ, 517, 565
Phillips, M. M. 1993, ApJL, 413, L105
Piran, T., Svirski, G., Krolik, J., Cheng, R. M., & Shiokawa, H. 2015, ApJ, 806, 164
Plewa, T., Calder, A. C., & Lamb, D. Q. 2004, ApJL, 612, L37
Prieto, J. L., Krühler, T., Anderson, J. P., et al. 2016, ApJ, 830, L32
Quintin, E., Webb, N. A., Guillot, S., et al. 2023, A&A, 675, A152
Raj, A., & Nixon, C. J. 2021, ApJ, 909, 82
Raskin, C., Kasen, D., Moll, R., Schwab, J., & Woosley, S. 2014, ApJ, 788, 75
Rees, M. J. 1988, Nature, 333, 523
Reinecke, M., Hillebrandt, W., & Niemeyer, J. C. 2002, A&A, 391, 1167
Renzini, A. 1999, in Chemical Evolution from Zero to High Redshift, ed. J. R. Walsh & M. R. Rosa, 185
Riess, A. G. 2020, Nature Reviews Physics, 2, 10
Riess, A. G., Filippenko, A. V., Challis, P., et al. 1998, AJ, 116, 1009
Röpke, F. K. 2007, ApJ, 668, 1103
Rosswog, S., Ramirez-Ruiz, E., & Hix, W. R. 2009, ApJ, 695, 404
Roth, N., & Kasen, D. 2018, ApJ, 855, 54
Roth, N., Kasen, D., Guillochon, J., & Ramirez-Ruiz, E. 2016, ApJ, 827, 3
Rybicki, G. B., & Lightman, A. P. 1986, Radiative Processes in Astrophysics
Salpeter, E. E. 1955, ApJ, 121, 161
Sato, Y., Nakasato, N., Tanikawa, A., et al. 2016, ApJ, 821, 67
Saxton, R., Read, A., Esquej, P., Miniutti, G., & Alvarez, E. 2011, in Narrow-Line Seyfert 1 Galaxies and their Place in the Universe, ed. L. Foschini, M. Colpi, L. Gallo, D. Grupe, S. Komossa, K. Leighly, & S. Mathur, 8
Sazonov, S., Gilfanov, M., Medvedev, P., et al. 2021, MNRAS, 508, 3820
Schlafly, E. F., & Finkbeiner, D. P. 2011, ApJ, 737, 103
Schmidt, G. D., Elston, R., & Lupie, O. L. 1992, AJ, 104, 1563
Seitenzahl, I. R., Ciaraldi-Schoolmann, F., Röpke, F. K., et al. 2013, MNRAS, 429, 1156

Serkowski, K., Mathewson, D. S., & Ford, V. L. 1975, ApJ, 196, 261
Shakura, N. I., & Sunyaev, R. A. 1973, A&A, 24, 337
Shen, K. J., & Bildsten, L. 2009, ApJ, 699, 1365
Shen, K. J., Kasen, D., Miles, B. J., & Townsley, D. M. 2018, ApJ, 854, 52
Shen, K. J., Kasen, D., Weinberg, N. N., Bildsten, L., & Scannapieco, E. 2010, ApJ, 715, 767
Shiokawa, H., Krolik, J. H., Cheng, R. M., Piran, T., & Noble, S. C. 2015, ApJ, 804, 85
Short, P., Nicholl, M., Lawrence, A., et al. 2020, MNRAS, 498, 4119
Shu, X. W., Wang, S. S., Dou, L. M., et al. 2018, ApJ, 857, L16
Shu, X. W., Wang, T. G., Jiang, N., et al. 2017, ApJ, 837, 3
Siebert, M. R., Strasburger, E., Rojas-Bravo, C., & Foley, R. J. 2019, The Astronomer's Telegram, 13131, 1
Soker, N. 2019, New A Rev., 87, 101535
Stevance, H. F., Maund, J. R., Baade, D., et al. 2019, MNRAS, 485, 102
Strubbe, L. E., & Quataert, E. 2009, MNRAS, 400, 2070
Suková, P., Zajaček, M., Witzany, V., & Karas, V. 2021, ApJ, 917, 43
Sun, A.-L., Greene, J. E., Zakamska, N. L., et al. 2018, MNRAS, 480, 2302
Sun, L., Shu, X., & Wang, T. 2013, ApJ, 768, 167
Taam, R. E. 1980, ApJ, 242, 749
Tinyanont, S., Millar-Blanchaer, M., Kasliwal, M. M., et al. 2021, Nature Astronomy, 5, 544
Tonry, J., Denneau, L., Heinze, A., et al. 2019, Transient Name Server Discovery Report, 2019-3, 1
van Dokkum, P. G. 2001, PASP, 113, 1420
vanVanvan Velzen, S., Gezari, S., Hammerstein, E., et al. 2021, ApJ, 908, 4
Wang, D. 2024, A&A, 682, L14
Wang, L., Baade, D., Höflich, P., et al. 2006, ApJ, 653, 490
Wang, L., Baade, D., & Patat, F. 2007, Science, 315, 212
Wang, L., Howell, D. A., Höflich, P., & Wheeler, J. C. 2001, ApJ, 550, 1030
Wang, L., & Wheeler, J. C. 2008, ARAA, 46, 433
Wang, L., Wheeler, J. C., & Höflich, P. 1997, ApJL, 476, L27
Wang, L., Baade, D., Höflich, P., et al. 2003, ApJ, 591, 1110
Wang, M., Yin, J., Ma, Y., & Wu, Q. 2022, ApJ, 933, 225
Wang, X., Li, W., Filippenko, A. V., et al. 2008, ApJ, 677, 1060
Webbink, R. F. 1984, ApJ, 277, 355
Wevers, T., Pasham, D. R., Jalan, P., Rakshit, S., & Arcodia, R. 2022, A&A, 659, L2
Whelan, J., & Iben, Jr., I. 1973, ApJ, 186, 1007
Wiersema, K., van der Horst, A. J., Levan, A. J., et al. 2012, MNRAS, 421, 1942
Wiersema, K., Higgins, A. B., Levan, A. J., et al. 2020, MNRAS, 491, 1771

Wolff, M. J., Nordsieck, K. H., & Nook, M. A. 1996, AJ, 111, 856
Woosley, S. E., & Weaver, T. A. 1994, ApJ, 423, 371
Woosley, S. E., Weaver, T. A., & Taam, R. E. 1980, in Texas Workshop on Type I Supernovae, ed. J. C. Wheeler, 96
Xian, J., Zhang, F., Dou, L., He, J., & Shu, X. 2021, ApJ, 921, L32
Yang, Y., Hoeflich, P. A., Baade, D., et al. 2019, arXiv e-prints, arXiv:1903.10820
Yang, Y., Hoeflich, P., Baade, D., et al. 2020, ApJ, 902, 46
Yang, Y., Yan, H., Wang, L., et al. 2022, ApJ, 939, 18
Zhao, Z. Y., Wang, Y. Y., Zou, Y. C., Wang, F. Y., & Dai, Z. G. 2022, A&A, 661, A55
Zheng, W., Filippenko, A. V., Mauerhan, J., et al. 2017, ApJ, 841, 64